

**Spectral signatures in shortwave radiation measurements to  
derive cloud and aerosol properties**

by

**Samuel Elie LeBlanc**

B.Sc., University of Ottawa, 2008

M.Sc., University of Colorado at Boulder, 2011

A thesis submitted to the

Faculty of the Graduate School of the

University of Colorado in partial fulfillment

of the requirements for the degree of

Doctor of Philosophy

Department of Atmospheric and Oceanic Sciences

2014

UMI Number: 3624806

All rights reserved

INFORMATION TO ALL USERS

The quality of this reproduction is dependent upon the quality of the copy submitted.

In the unlikely event that the author did not send a complete manuscript and there are missing pages, these will be noted. Also, if material had to be removed, a note will indicate the deletion.



UMI 3624806

Published by ProQuest LLC (2014). Copyright in the Dissertation held by the Author.

Microform Edition © ProQuest LLC.

All rights reserved. This work is protected against unauthorized copying under Title 17, United States Code



ProQuest LLC.  
789 East Eisenhower Parkway  
P.O. Box 1346  
Ann Arbor, MI 48106 - 1346

This thesis entitled:  
Spectral signatures in shortwave radiation measurements to derive cloud and aerosol properties  
written by Samuel Elie LeBlanc  
has been approved for the Department of Atmospheric and Oceanic Sciences

---

Peter Pilewskie

---

Sebastian Schmidt

Date \_\_\_\_\_

The final copy of this thesis has been examined by the signatories, and we find that both the content and the form meet acceptable presentation standards of scholarly work in the above mentioned discipline.

LeBlanc, Samuel Elie (Ph.D., Atmospheric Sciences)

Spectral signatures in shortwave radiation measurements to derive cloud and aerosol properties

Thesis directed by Prof. Peter Pilewski

The amplitude and spectral shape of shortwave radiation are used to retrieve aerosol and cloud properties from airborne and ground based measurements. By interacting with clouds and aerosols in the Earth's atmosphere, the wavelength-dependent radiation emitted by the sun is modified. This thesis presents the change in radiation due to absorption and scattering by clouds and aerosols, which result in distinct spectral signatures in shortwave radiation spectra.

The spectral signature in shortwave radiation due to aerosols is quantified by airborne measurements of irradiance above and below aerosol layers. This radiative effect is quantified by the relative forcing efficiency, which is used to compare the impact of aerosols from different air masses, locations, and time of day. The relative forcing efficiency is the net irradiance change due to the presence of aerosols normalized by aerosol optical thickness and incident irradiance. It is shown to vary by less than 20% per unit of midvisible aerosol optical thickness for aerosols sampled during 4 different experiments, except for highly absorbing aerosols near Mexico City. The similarity in relative forcing efficiency for these experiments, not expected a priori, suggests that this quantity is constrained for various types of aerosols with differing scattering and absorption characteristics even when surface albedo differs. To estimate the radiative effect of aerosols sampled in the Los Angeles basin during one of the experiments, where no concurrent measurements of optical thickness with spectral irradiance were available, a new iterative technique was devised to use aerosol optical thickness measurements from another airborne platform.

Cloud-transmitted zenith radiance spectra were measured from the ground in Boulder, Colorado. In these measurements, spectral signatures of cloud optical and microphysical properties were uncovered. The spectral signatures are the result of radiation that is transmitted through clouds, where ice or liquid water cloud particles modulate the radiation by absorbing and scatter-

ing incident light in a wavelength-dependent manner. Typically, the magnitudes of radiance at 2 wavelengths have been used to retrieve cloud properties, but by using wavelength-dependent features more sensitivity to cloud microphysical properties is obtained. This thesis presents a method to analyze wavelength-dependent signal, where spectral features such as slopes, curvatures, and shifts in locations of maxima and minima are parameterized. These spectral features found in normalized radiance are quantified by introducing 15 parameters. These 15 parameters form the basis of a new generalized retrieval obtaining cloud optical thickness ( $\tau$ ), effective radius ( $r_e$ ), and thermodynamic phase ( $\phi$ ). When applied to a liquid water cloud case, this retrieval matched a measured transmittance spectrum with a smaller root mean square difference over the entire spectrum (3.1%) than two other methods (up to 6.4%). To quantify the retrieval over all possible combinations of  $\tau$ ,  $r_e$ , and  $\phi$ , simulated measurements were used in conjunction with realistic measurement and model error characteristics. By combining these error characteristics within the GEneralized Nonlinear Retrieval Analysis (GENRA) a solution probability distributions can be built. The information of cloud properties contained within cloud-transmitted radiance is greater on average for liquid water clouds than for ice clouds. For all possible combinations of cloud properties, radiance transmitted through clouds with  $\tau < 20$  contain the most information on cloud properties, indicating that the 15 parameters have greatest sensitivity to cloud properties of optically thin clouds ( $\tau < 20$ ). Of the 15 parameters, only 10 are required to retrieve accurately  $\tau$ ,  $r_e$ , and  $\phi$  for any cloud except for ice clouds with  $\tau > 25$  and  $r_e > 30 \mu\text{m}$ . Using this retrieval, the correct thermodynamic phase is determined from transmittance with a probability greater than 99.4% for horizontally homogeneous clouds that contain either ice or liquid water cloud particles.

## Dedication

To Jeanne, my wife-to-be.

## Acknowledgements

I am thankful to all the people who have helped me throughout my graduate school career. I express my deepest gratitude to my thesis advisor, Peter Pilewskie, for his mentorship, help, and crucial support; Sebastian Schmidt for his generosity in ideas and time; Odele Coddington for her patience and countless hours of devotion; Scott Kittelman for his presence, assistance, and insights particularly on instrumentation; present and past members of the Atmospheric Radiation Group at CU: Bruce Kindel, Patrick McBride, Yolanda Roberts, Michael King, Shi Song, and Andrew Kren. Your help, support, questions, conversations, and constructive criticism have been instrumental in my development as a scientist.

I have been fortunate to take part in many field missions, where I have witnessed great scientists work under strenuous schedules. I extend my appreciation to these individuals who, during these times, have directly or indirectly helped me gain a deeper understanding of atmospheric science. My appreciation also extends to all those at NASA, NOAA, NCAR, and NSF who have made these field missions possible.

I also wish to acknowledge the faculty of the Department of Atmospheric and Oceanic Sciences for their dedication to teaching.

Finally, I wish to thank my wife-to-be, housemates, colleagues, friends, and family for their continued support and friendship.

## Contents

Chapter	
<b>1</b>	Introduction <span style="float: right;">1</span>
1.1	Motivation <span style="float: right;">2</span>
1.2	Remote sensing <span style="float: right;">3</span>
1.3	Measurement and Instrumentation <span style="float: right;">5</span>
1.4	Overview <span style="float: right;">7</span>
<b>2</b>	Spectral aerosol direct radiative forcing from airborne radiative measurements during Cal- Nex and ARCTAS <span style="float: right;">9</span>
2.1	Introduction <span style="float: right;">10</span>
2.1.1	Radiative Forcing <span style="float: right;">11</span>
2.1.2	Relative Forcing Efficiency <span style="float: right;">12</span>
2.1.3	This Study <span style="float: right;">13</span>
2.2	Instrumentation and Radiative Transfer Model <span style="float: right;">13</span>
2.2.1	Solar Spectral Flux Radiometer <span style="float: right;">14</span>
2.2.2	Ancillary Instruments <span style="float: right;">15</span>
2.2.3	Radiative Transfer Model <span style="float: right;">16</span>
2.3	Research at the Nexus of Air Quality and Climate Change <span style="float: right;">16</span>
2.4	Results and Discussion from CalNex: 19 May 2010 <span style="float: right;">18</span>
2.4.1	Spectra of Retrieved Aerosol Properties <span style="float: right;">19</span>

2.4.2	Retrieved Along-Path Aerosol Properties . . . . .	22
2.4.3	Retrieved Relative Forcing Efficiency . . . . .	22
2.4.4	Corresponding Diurnal Average of Forcing Efficiency . . . . .	25
2.5	Summary and Discussion . . . . .	26
2.6	Appendix A: Acronyms . . . . .	28
2.7	Appendix B: Radiative Properties . . . . .	28
2.7.1	Spectral Irradiance . . . . .	29
2.7.2	Aerosol Optical Thickness . . . . .	29
2.7.3	Single Scattering Albedo . . . . .	29
2.7.4	Asymmetry Parameter . . . . .	30
2.7.5	Ångström Exponent . . . . .	30
2.8	Appendix C: Aerosol Retrieval . . . . .	31
2.8.1	Retrieval Description . . . . .	32
2.8.2	Retrieval Uncertainty . . . . .	35
2.8.3	Retrieval Testing . . . . .	39
2.8.4	Retrieval Sensitivity and Uniqueness . . . . .	39
2.8.5	Retrieval Comparisons of Secondary Aerosol Optical Properties . . . . .	41
2.9	Acknowledgements . . . . .	43
<b>3</b>	<b>A generalized method for discriminating thermodynamic phase and retrieving cloud optical thickness and effective radius using transmitted shortwave radiance spectra</b>	<b>44</b>
3.1	Introduction . . . . .	45
3.2	Instrumentation and Measurements . . . . .	47
3.2.1	Solar Spectral Flux Radiometer . . . . .	47
3.2.2	Skywatch Observatory . . . . .	48
3.2.3	Satellite measurements . . . . .	49
3.3	Case studies . . . . .	49

3.4	Radiative Transfer Simulations and Description of Retrieval Parameters . . . . .	51
3.4.1	Radiative transfer model . . . . .	51
3.4.2	Ancillary inputs . . . . .	52
3.4.3	Modeled Look-Up-Tables (LUT) . . . . .	54
3.4.4	Variability in normalized radiance spectra due to $\tau$ , $r_e$ , and $\phi$ physical basis	54
3.4.5	Definition of spectral parameters . . . . .	60
3.4.6	Dependence on thermodynamic phase, optical thickness, and effective radius	67
3.5	Retrieval methodology . . . . .	70
3.5.1	Retrieval uncertainty . . . . .	72
3.5.2	Comparisons to other methods . . . . .	72
3.6	Summary and Conclusions . . . . .	81
3.7	Acknowledgements . . . . .	84
4	Statistical evaluation of parameters used to discriminate cloud thermodynamic phase and retrieve optical thickness and effective radius from transmitted shortwave radiance spectra	85
4.1	Introduction . . . . .	86
4.2	Simulation of zenith radiance spectra . . . . .	89
4.2.1	Radiative transfer model . . . . .	89
4.2.2	Ancillary inputs – base case . . . . .	90
4.2.3	Modeled radiance spectra and parameters . . . . .	90
4.3	Variation in modeled transmitted radiance spectra and parameters due to ancillary inputs . . . . .	92
4.3.1	Variations in cloud base height and extent, surface albedo, and precipitable water . . . . .	93
4.3.2	Variations in vertical profile of $r_e$ . . . . .	95
4.3.3	Variations in retrieval parameters . . . . .	96
4.4	Retrieval evaluation methodology . . . . .	98

4.4.1	Inverse problem theory . . . . .	98
4.4.2	GEneralized Nonlinear Retrieval Analysis (GENRA) . . . . .	99
4.4.3	Building the probability density functions . . . . .	101
4.4.4	Retrieval Diagnostics . . . . .	107
4.5	Results: Simulated Spectral Transmittance . . . . .	109
4.5.1	Sample case studies modeled spectra . . . . .	110
4.5.2	Information content, uncertainty, and biases for ice and liquid water clouds of varying $\tau$ and $r_e$ . . . . .	114
4.5.3	Effect of vertically varying effective radius on retrieval . . . . .	120
4.6	Summary and conclusions . . . . .	122
4.7	Acknowledgements . . . . .	123
<b>5</b>	<b>Summary and Outlook</b>	<b>124</b>
5.1	Outlook . . . . .	128
	<b>Bibliography</b>	<b>130</b>

## Tables

### Table

2.1	Input and output of different methods used to obtain layer-averaged aerosol optical properties as well as relative forcing efficiency ( $f_e$ ) from airborne spectral irradiance ( $F$ ) and aerosol optical thickness ( $\tau$ ) measurements . . . . .	11
2.2	Available spectral radiative measurements on board aircrafts during CalNex and ARCTAS field missions . . . . .	37

- 3.1 Definition, wavelength range used, and expected behavior for the 15 spectral parameters.  $L_\lambda$  indicates the radiance evaluated at a wavelength,  $\lambda$ , in microns. The function  $lin(y; \lambda = a..b)$  describes the linear fit of values evaluated at  $\lambda = a$  and  $\lambda = b$ , where represents any variable that is calculated from the radiance spectrum. The function  $m(y; \lambda = a..b)$  describes the slope of  $y$  evaluated over the range of  $\lambda = a$  to  $\lambda = b$ . The average value of  $y$  over the range of  $\lambda = a$  to  $\lambda = b$  is presented as  $\langle y \rangle|_{\lambda=a}^b$ . In addition to defining each spectral parameter by the symbol  $\boldsymbol{\eta}_1$  through  $\boldsymbol{\eta}_{15}$ , other symbols are used to provide additional insight into the nature of the parameter. For parameters defined by a measure of the curvature of radiance,  $C_\lambda$  is used, where a convex curvature represents a slope that decreases with increasing wavelength, and concave curvature for a slope that increases with increasing wavelength. The spectral derivatives of the normalized radiances are denoted by  $\partial/\partial\lambda_\lambda$ . When this derivative, as a function of wavelength, is fitted to a line, its slope is represented by  $\partial^2/\partial\lambda_\lambda^2$ . The slope of this derivative over a wavelength range is roughly equivalent to the average second derivative over the same wavelength range, but differences may result from the linear fitting process. Slopes, ratios, mean, and normalized radiances are presented as  $sl_\lambda$ ,  $r_\lambda$ ,  $\langle R \rangle_\lambda$ , and  $R_\lambda$  respectively, with  $\lambda$  denoting a representative wavelength in microns where the features are quantified. . . . . 64
- 3.2 Root-mean-square (rms) of the percent difference for the entire wavelength range between modeled spectra based on the 3 different retrievals and the 3 sample measured spectra presented in Fig. 3.13. . . . . 80
- 4.1 Method, shorthand symbolism, and wavelength region for each 15 parameters introduced by *LeBlanc et al.* [2014] . . . . . 92
- 4.2 Parameters with measurement uncertainties for the 3 cloud cases . . . . . 110

## Figures

### Figure

- 1.1 Shortwave irradiance spectra for a solar zenith angle of  $30^\circ$  incident at the top of atmosphere (in black), in the troposphere, but devoid of influences from aerosol or clouds (in green), under an aerosol layer with an optical thickness of 1 (in red), and under liquid clouds only with an optical thickness of 15 and effective radius of  $10 \mu\text{m}$  (in blue). . . . . 4
- 1.2 Radiance in a midvisible wavelength measured by the original and new narrow field-of-view light collector as a function of the angle between the incident light and the normal of the light collector. The radiance is presented as a fraction of the incident light at  $0^\circ$ . . . . . 6
- 2.1 Upwelling and downwelling irradiance spectra from 1.6 km West of Caltech measured at the top flight leg ( $\sim 1000\text{m}$  altitude) and the bottom flight leg ( $\sim 500\text{m}$  altitude) with the Solar Spectral Flux Radiometers (SSFR) during the Research at the Nexus of Air Quality and Climate Change field mission (CalNex). Solar spectral irradiance that is transmitted through part of the atmosphere is labeled downwelling. Upwelling spectral irradiance shows the influence of reflectance from the underlying surface. . . . . 14
- 2.2 Map of the P-3 airborne platform's flight path around the Los Angeles region on 19 May 2010. The start and end of the flight path (center of the plot) is located in Ontario, California. The flight legs of interest in this figure are located near the Caltech ground site (blue square). . . . . 17

- 2.3 Profiles of in situ measured-extinction coefficients from the P-3 flight track (circles) and extinction coefficients derived from the High Spectral Resolution Lidar (HSRL, diamonds) at 532 nm at ambient humidity. (a) Vertical profile of aerosol extinction coefficients (lidar curtain) overlaid with the in situ extinction coefficient (point measurements) along the flight track. (b) In situ extinction coefficient maps at each altitude (2000–3000 m, 1500–2000 m, 800–1400 m, 400–800 m from top to bottom respectively measured at approximately 5 min intervals for approximately 20 min). 19
- 2.4 Flight leg geometry used to characterize aerosol properties within the aerosol layer. The dashed lines represent the aircraft flight altitude above and below the aerosol layer. . . . . 20
- 2.5 Retrieved aerosol single scattering albedo, asymmetry parameter, optical thickness, and surface albedo, and measured absorption for a single point 1.6 km west of Caltech during the CalNex case of 19 May 2010. (a) Retrieved secondary properties where the shading denotes their uncertainty range. (b) Measured and modeled absorption. Modeled values (at the discrete points) are outside of gas absorption bands. Dashed lines are interpolations between window values. . . . . 21
- 2.6 Retrieved aerosol single scattering albedo ( $\varpi$ , in black), asymmetry parameter ( $g$ , in green), optical thickness ( $\tau$ , in red), and the surface albedo ( $\alpha$ , in blue) for two wavelengths, (a) 380 nm and (b) 500 nm, along the flight path over Caltech during CalNex flight on 19 May, 2010. The x-axis represents the distance from Caltech (west to east), and the y-axis represents the magnitude of the retrieved properties. Blank spaces indicate when the retrieval failed to converge. . . . . 23

- 2.7 Aerosol direct radiative forcing for (a) along-flight, at 500 nm, and (b) the spectral averages over the entire flight leg. In (b) results from ARCTAS, MILAGRO [*Schmidt et al.*, 2010], and INTEX-NA [*Redemann et al.*, 2006] are shown for comparison. The shading in (a) represents the relative forcing efficiency uncertainty; in (b) it represents the standard deviation over the flight legs. Dashed lines are above-layer forcing, solid lines, below-layer forcing. . . . . 24
- 2.8 Conceptual map of the aerosol retrieval algorithm. Starting from measured spectral irradiance above and below the aerosol layer (1) and initial estimates for single scattering albedo, asymmetry parameter, surface albedo, and aerosol optical thickness (2). The steps 3, 4, and 5 compare modeled spectral irradiance to the measured values after modifying the single scattering albedo, and two values of the asymmetry parameter, respectively. If the two methods for deriving asymmetry parameter do not agree (step 6), the aerosol optical thickness is adjusted until the two methods return the same asymmetry parameter. Steps 2–6 are repeated until the aerosol optical thickness modification obtained does not vary (7) between each repetition. . . 33
- 2.9 Determination of the aerosol optical thickness and its uncertainty by using: (a) Retrieved asymmetry parameter from the two different methods ( $g$  and  $\hat{g}$ ), (b) Difference between  $g$  and  $\hat{g}$  as a function of aerosol optical thickness. The red line is the range in uncertainty for the retrieved aerosol optical thickness. Here the difference between the two values of the asymmetry parameter is near zero. The error bars for  $g$  and  $\hat{g}$  have been determined from an approximation of the total derivative method (Eq. 2.11), while the dotted line represents the measured aerosol optical thickness. . . 38
- 2.10 Retrieved aerosol optical thickness (y axis) compared with measured aerosol optical thickness (AATS-14; x axis) during the ARCTAS case on 9 July 2008. Wavelength is indicated by the symbol colors. The dotted line denotes a slope of one. The two circled areas represent regions where the ratio of retrieved optical thickness to AATS optical thickness are approximately 1.3 and 0.85, respectively. . . . . 40

2.11	Distributions of retrieved and in situ-measured aerosol properties at 532 nm. (a) The derived asymmetry parameter determined by Mie-scattering calculations. These calculations use inputs of aerosol particle-size distribution from the White-Light Optical Particle Counter (WOPC), Ultrahigh Sensitivity Aerosol Size Spectrometer (UHSAS), and Nucleation Mode Aerosol Size Spectrometer (NMASS). (b) Comparison of single scattering albedo as measured by the Cavity Ring Down (CRDS) and Photoacoustic Absorption Spectrometer (PAS) instruments to its retrieved values. These values are also compared to the values determined by AERONET which were measured $\sim 5$ h later. . . . .	42
3.1	Broadband short- (pyranometer) and long-wave (pyrgeometer) irradiance and cloud base heights (ceilometer) for horizontally heterogeneous (left panel) and homogeneous (right panel) clouds taken on 23 May 2012. The top panel presents one image from the sky web cam for either heterogeneous or homogeneous clouds taken from the Skywatch observatory. . . . .	50
3.2	Atmospheric sounding profiles of temperature (black) and dew point (grey) taken near Denver International Airport for the case study time periods: (A) liquid cloud case on 25 May 2012, (B) mixed-phase cloud case on 6 August 2012, and (C) ice cloud case on 10 January 2013. Cloud bottom and top values determined from ground-based and satellite data (see text). . . . .	52
3.3	Spectral surface albedo used as input for the radiative transfer modeling for spring/summer. To approximate a full spectrum for varying days, the vegetated spectral surface albedo (black line) measured by <i>Michalsky et al.</i> [2003] is scaled using the discrete-band surface albedo product retrieved from Moderate Resolution Imaging Spectroradiometer (MODIS) measurements [ <i>Schaaf et al.</i> , 2002] at the wavelengths denoted by X. This scaling is interpolated between the discrete MODIS bands. . . . .	53

- 3.4 (a) Spectral bulk absorption coefficient and (b) asymmetry parameter for different thermodynamic phases of water. Notice the local maxima offset between ice water, liquid water, and water vapor near 900 nm, 1100 nm, and 1400 nm. The bulk ice absorption coefficient has been determined by *Warren and Brandt* [2008], while the bulk liquid water absorption coefficient has been determined by *Cumming* [2013]. The bulk water vapor absorption has been calculated using the HITRAN model described by *Rothman et al.* [2009] for an optical path length of 10 m with pure water vapor pressure of 15 hPa at 293 K [*Ptashnik et al.*, 2004]. The asymmetry parameter for liquid drops were calculated from Mie scattering calculation following the methodology developed by *Wiscombe* [1980]. Ice asymmetry parameter were obtained from the scattering models for severely roughened general habit mixture described by *Baum et al.* [2011]. . . . . 55
- 3.5 Modeled zenith radiance spectra transmitted through clouds with a few combinations of optical thickness ( $\tau$ ) for ice and liquid water clouds with an effective radius ( $r_e$ ) of 20  $\mu\text{m}$  for the atmospheric state and surface albedo defined for 2012-05-25 and a solar zenith angle of 50°. Top panel (a) shows the radiance spectra in  $\text{Wm}^{-2}\text{nm}^{-1}\text{sr}^{-1}$  units and bottom panel (b) shows the radiance spectra normalized by their maximum value (unitless). The radiance minima centered at 760 nm, 940 nm, 1130 nm, and 1400 nm represent gas absorption bands that are ignored in this work. . . . . 57
- 3.6 Normalized radiance spectra for liquid (left) and ice (right) clouds with an  $r_e$  of 20  $\mu\text{m}$  and  $\tau$  varying from 0.2 to 100 (where darker colors denotes optically thicker clouds). A clear sky normalized radiance (denoted in green) is added for comparison to the optically thinnest clouds. Three wavelength ranges where there are spectral features are indicated by the grey curly brackets. . . . . 58

- 3.7 Normalized radiance spectra transmitted through liquid and ice clouds of  $\tau$  of 30 and  $r_e$  ranging from 2  $\mu\text{m}$  to 30  $\mu\text{m}$  for liquid clouds and 10  $\mu\text{m}$  to 60  $\mu\text{m}$  for ice clouds. Darker orange lines represent radiance spectra transmitted through larger ice particles. Darker blue lines represent the radiance spectra transmitted through larger liquid cloud droplets. 3 wavelength ranges where there are spectral features are indicated by the grey curly brackets. . . . . 60
- 3.8 Radiance spectra normalized by its value at 1000 nm for liquid (left) and ice (right) clouds with  $r_e = 20 \mu\text{m}$  and  $\tau$  varying from 1 to 100 (where darker colors denotes optically thicker clouds). Three spectral features, which vary with changes of  $\tau$ , (see text) are quantified by the first 3 parameters,  $\eta_1$ ,  $\eta_2$ , and  $\eta_3$ . The transmittance that contribute to calculating  $\eta_1$ ,  $\eta_2$ , and  $\eta_3$  are highlighted and indicated by the numbers 1, 2, and 3, respectively. The shaded areas indicated by 1 overlap for different optical thickness. To increase visibility of the smaller shaded areas (denoted by lighter blues and darker oranges), these are plotted in front of the larger shaded areas. . . . . 62
- 3.9 (a) Transmittance of liquid water clouds of varying optical thickness and effective radius of 20  $\mu\text{m}$  and (b) the slope of normalized radiance for the wavelength range in 530 - 610 nm,  $\eta_{11}$ , as a function of  $\tau$  for ice and liquid clouds, evaluated for 3 different effective radii. In (a), the slope in the visible is identified by the highlighted region. The normalized radiance spectra and the  $\eta_{11}$  calculated from them were modeled with ancillary inputs based on 2012-05-25, for a solar zenith angle of  $50^\circ$ . . 63
- 3.10 The value of the parameters,  $\eta_1$  through  $\eta_{15}$ , as a function of optical thickness for 3 effective radii (colors) for liquid (solid) and ice (dashed) clouds. The shading surrounding each line denotes the standard deviation of the variability in the parameters due to measurement uncertainty (see text). . . . . 67

- 3.11 Time series of retrieved cloud properties determined by 3 different transmittance based retrieval methods; case A (left) for liquid cloud, case B (center) for mixed-phase cloud, and case C (right) for ice cloud. The mixed-phase cloud case represents a span in time where both ice and liquid water cloud particles are expected to have been present. Colors represent three different cloud retrieval methods: this work (black), the slope method (blue) and the 2-wavelength method (red). For each case study, the top-most panel presents the retrieved optical thickness,  $\tau$ , the panel directly below shows the effective radius,  $r_e$ , the panel directly below shows the minimum  $\chi^2$  determined by this work (15-parameter method), and the lowest panel shows thermodynamic phase,  $\phi$ , designated by this work. The y-axis scale in  $\tau$  and  $r_e$  differs for each case. . . . . 74
- 3.12 Scatter plot of (a) optical thickness and (b) effective radius for the liquid water cloud (case A) from the slope (blue) and 2-wavelength (red) methods compared to the current works retrieval. Dashed lines represent the best-fit lines. Larger thickness of the symbols indicates higher density of the points at that location. . . . . 77
- 3.13 Sample measured and modeled spectra for the 3 different cloud case studies. Measured radiance spectra (black) are specific to a certain point (see legend) in the time series of Fig. 3.11. Modeled radiance spectra, are based on the retrieved cloud properties from each method (this work = green; slope = blue, and 2-wavelength = red) for the same time instance. The percentage difference in the modeled spectra with respect to the measured spectra is shown in lower panels for wavelength regions outside of water vapor absorption bands. Modeled radiance spectra based on the current works retrieval for an ice cloud (dashed line) and if it were a liquid cloud (solid line) is presented in case B. The slope and 2-wavelength modeled spectra represent a liquid cloud in case B. . . . . 79

- 4.1 Sample modeled (a) radiance ( $Wm^{-2}nm^{-1}sr^{-1}$ ) spectra and (b) normalized radiance (unitless) transmitted through clouds with 3 combinations of  $\tau$ ,  $r_e$ , and  $\phi$  (cases A, B, and C) and a solar zenith angle of  $50^\circ$ . The grey shaded regions represent the spectral bands used in determining the different parameters, introduced by *LeBlanc et al.* [2014],  $\eta_1$ ,  $\eta_5$  to  $\eta_{11}$ , and  $\eta_{15}$ . Grey vertical lines indicate the wavelength for parameters,  $\eta_2$  to  $\eta_4$  and  $\eta_{12}$  to  $\eta_{14}$ , which are evaluated at a single wavelength. . . . . 91
- 4.2 Modeled zenith spectra with variance due to (a) cloud base height above ground, (b) surface albedo evaluated for the 5 periods centered on the dates listed, and (c) precipitable water. Top panels show the radiance spectra for the 3 cloud cases (case A - red, case B - green and case C - blue) evaluated with different cloud base height above ground, surface albedo, and precipitable water identified by different line styles. The bottom panels show the difference in radiance spectra as a percentage of the maximum radiance between radiance spectra evaluated with the changing ancillary inputs presented in the top panels and the base case ancillary inputs. The dotted grey line indicates a 0% difference to the radiance evaluated with base case ancillary inputs. . . . . 94
- 4.3 (a) Vertical profile of  $r_e$  for a cloud with constant  $r_e$  (solid line) and a cloud with  $r_e$  varying proportionally with cloud height ( $z$ , dashed line). Each 'X' symbol denotes the middle point of the cloud layer. (b) The two profiles of  $r_e$  as model input for the radiance spectra calculated with 3 cloud cases. The spectra modeled from vertically varying  $r_e$  are presented as dashed lines. (c) The differences between radiance spectra evaluated with the two  $r_e$  profiles. . . . . 96

- 4.4 Variation in modeled parameters as a percentage of the total range of the parameter evaluated with changes due to (a) cloud base height above ground in the first column, (b) surface albedo evaluated for the 5 periods centered on the dates listed in the second column, and (c) precipitable water in the third column. Each row shows the variation of each parameters,  $\eta_{i=1..15}$ , represented by the colored lines, for the 3 cloud cases (A in the top panel, B in the middle panel, and C in the bottom panel). The shaded part represents variations of less than 2%. . . . . 97
- 4.5 Measurement PDF of  $\eta_2$  for the 3 cloud cases. . . . . 104
- 4.6 Posterior PDF for cloud cases A, B, and C. The colors denote the probability of the selected pair of  $\tau$  and  $r_e$  to describe the measured spectrum. The colors for each case denote different probabilities, indicated directly on the contour. The highest probability is denoted by the red contour, while the smallest non-zero probability is indicated by the blue contour. The black X denotes the maximum likelihood solution. The x- and y-axes are magnified to center on the optical thickness and effective radius regions where the posterior PDF has a non-zero probability. . . . . 111
- 4.7 Marginal PDFs in optical thickness (top panels) and effective radius (bottom panels) for the 3 cloud cases. For each marginal PDF, the shaded region denotes its variance, while the dashed line denotes the maximum likelihood solution in either optical thickness or effective radius. The SIC calculated from the marginal PDF (either  $H_\tau$  or  $H_{r_e}$ ) is reported on each panel. . . . . 112
- 4.8 The Shannon information content (SIC) for each parameter for the 3 cloud cases. SIC for each parameter can be calculated (a) independently or (b) cumulatively (see text). The dashed lines represent the cumulative SIC where only a subset of parameters are used ( $\eta_1, \eta_2, \eta_3, \eta_5, \eta_6, \eta_7, \eta_9, \eta_{11}, \eta_{13}$ , and  $\eta_{15}$ ) and describes similar cumulative SIC obtained by combining all parameter (solid lines). . . . . 113

- 4.9 The uncertainty of optical thickness (a) and effective radius (b) as a function of ingested parameters for the 3 cloud cases. The uncertainties after ingesting a subset of the parameters are indicated by the dashed line. The prior uncertainty in  $\tau$  and  $r_e$  is described as the standard deviation of the marginal PDF of a non-informative prior PDF defined in cloud property space  $\Pi_{liq}$  for case A, and  $\Pi_{ice}$  for case B and C. 115
- 4.10 Shannon information content (distinguished by colored-contour lines) calculated from each final posterior PDF with a subset of parameters determined from simulated measurement with varying optical thickness and effective radius presented for (a) liquid and (b) ice clouds. The grey boxed regions related to 1 – thin clouds, 2 – thick clouds with large particles, and 3 – thick clouds with small particles. . . . . 116
- 4.11 Cumulative SIC after sequential ingestion of each parameter into GENRA for the 3 regions of optical thickness, effective radius, and thermodynamic phase determined in Fig. 4.10. The regions are denoted by the legend in the bottom right side of each panel. The error bars at each parameter show the maximum and minimum value of SIC for that parameter in the specified region. The X denotes the mean cumulative SIC due to the particular parameter for that region. . . . . 117
- 4.12 Uncertainties of  $\tau$  (upper panel) and  $r_e$  (bottom panel) for liquid (left column) and ice (right column) clouds are presented as a function of  $\tau$  and  $r_e$ . The values of each contour lines (denoted by different colors) refer to uncertainties in  $\tau$  or  $r_e$ . The grey boxes denote the same regions of the  $\tau$  and  $r_e$  introduced in Fig. 4.10 . . . . . 119
- 4.13 Probability of retrieving a liquid water cloud after ingesting the parameters sequentially within the GENRA algorithm for the 3 cloud cases. A liquid water cloud probability of 0 also means an ice cloud probability of 1. . . . . 120

- 4.14 Bias in retrieved optical thickness (top panels) and effective radius (bottom panels) of liquid water clouds (left panels) spanning space  $\Pi_{liq}$  and ice clouds (right panel) spanning space  $\Pi_{ice}$  when the input simulated measurements include clouds with vertically varying effective radius. Negative biases (red) represent retrieved values less than the truth and positive biases (blue) represent retrieved values greater than the truth, with the white regions indicating no bias. The true values of  $r_e$  are the mean  $r_e$  of the vertical profiles of cloud particle sizes. . . . . 121

# Chapter 1

## Introduction

This thesis uses measurements of shortwave radiation over a continuous spectral range to retrieve optical and microphysical properties of clouds and aerosols. The shortwave radiation was measured with a spectrometer system onboard multiple airborne and ground-based platforms. The spectrometer system was used to quantify the radiative effects of aerosol layers and clouds. Focused measurements of an aerosol layer were used to extract its bulk aerosol properties by sampling shortwave irradiance spectra above and below the layer. By using direct measurements of irradiance, the effect on shortwave radiation by aerosol layers is quantified. Cloud-transmitted radiance measurements also offer a view of clouds unavailable from commonly used reflectance based measurements. Although transmitted photons have interacted with cloud particles throughout the vertical extent of the cloud, traditional methods of extracting cloud microphysical information retrieve larger uncertainties when used on transmittance rather than reflectance. By using multiple spectral features found in transmittance unique to either ice or liquid water clouds that vary with cloud properties, this challenge was addressed. In addition, these underexplored spectral features themselves have been quantified with 15 parameters, which are used in a new generalized cloud property retrieval. The retrieval solution was also quantified by evaluating its information content when assuming realistic error characteristics. In this thesis, these types of measurements taken during case studies are used to answer the following 3 questions:

- (1) What are the impacts of aerosol on the spectrally-resolved net radiative effects? Is there a recurrent pattern in the radiative effects of aerosol observed in different locations?

- (2) What do spectral features in ground-based zenith radiance measurements reveal about cloud optical and microphysical properties?
- (3) How do naturally occurring variations in environmental conditions affect the accuracy and precision of the retrieval of cloud optical and microphysical properties from transmitted radiance?

Each of these questions represents the focus of the next 3 chapters. To answer these questions new retrieval techniques were devised and quantified. New instrumentation and modifications to existing instruments were also necessary to obtain the measurements used throughout this thesis.

## 1.1 Motivation

Shortwave radiation reaching the Earth's surface is impacted the most by clouds and aerosols in broad wavelength bands and also in a spectrally-dependent manner. Clouds reduce the radiant energy emitted by the sun reaching the Earth's surface by a global average of  $53Wm^{-2}$  [Allan, 2011], for aerosol this decrease is  $11Wm^{-2}$  [Kim and Ramanathan, 2008]. Predicting how these estimates will change is one of the greatest uncertainties when determining future climate [Forster *et al.*, 2007]. When estimating the net effect of clouds and aerosols on the shortwave radiation, satellite and ground-based observations are crucial and are a major driver of the accuracy of these estimates [e.g., Allan, 2011; Yu *et al.*, 2006]. More of the information contained in the observations can be extracted when using radiation measurements at multiple wavelength bands instead of at a single or dual wavelength bands [e.g., L'Ecuyer *et al.*, 2006; Cooper *et al.*, 2006; Coddington *et al.*, 2012].

By scattering and absorbing radiation in a wavelength-dependent manner, clouds and aerosols modulate incident radiation creating unique spectral signatures. Figure 1.1 shows the incident radiation spectrum at top of atmosphere, which peaks near 475 nm. 95% of the energy in the shortwave radiation is distributed over the wavelength range 350 nm – 2150 nm [Kurucz, 1994]. After being transmitted to the troposphere, at 3 km in altitude, much of the incident radiation

remains even after being absorbed by various gases (green line Fig. 1.1). The radiation within the troposphere is further reduced by aerosol and clouds outside gas absorption bands.

When transmitted through aerosols, the radiation within the troposphere is decreased due to scattering and absorption. The radiative effect of aerosols increases as wavelength shortens, with the largest effect at wavelengths shorter than 1000 nm (red line in Fig. 1.1). When radiation is transmitted through clouds, there is a broadband reduction of radiation spanning the entire shortwave radiation spectrum (blue line, Fig. 1.1). In addition to the broad band reduction in radiation, clouds also modify spectral features in the transmitted radiation.

In this thesis, the spectral changes of incident radiation due to aerosols and clouds are quantified. For aerosols, their radiative effect is quantified by the relative forcing efficiency [*Redemann et al.*, 2006], which is this change in net irradiance introduced by an aerosol layer normalized by the incident irradiance and the midvisible aerosol optical thickness, thus reducing sensitivity to solar zenith angles and aerosol optical thickness. The relative forcing efficiency has similar spectral shapes and magnitude for aerosols of different types measured in different locations. For clouds, their spectral signatures consist of features in transmitted radiance at different locations within the spectra. The spectral features are sensitive to liquid and ice cloud particle absorption and scattering properties.

## 1.2 Remote sensing

To evaluate how much clouds and aerosols cool or warm the surface, an accurate quantification of the scattering and absorption properties is needed [e.g., for aerosols, *Bond and Sun*, 2005]. The following variables quantify the scattering and absorption properties for aerosols and clouds: cloud or aerosol optical thickness ( $\tau$ ), aerosol single scattering albedo ( $\varpi$ ), aerosol asymmetry parameter ( $g$ ), cloud particle effective radius ( $r_e$ ), and cloud thermodynamic phase ( $\phi$ ). By reducing the uncertainty of aerosol and cloud properties, the effect of clouds and aerosol on climate can be assessed with more certainty, even at a local level [*Penner et al.*, 1994].

When using wavelength-dependent information to retrieve cloud and aerosol properties, as-

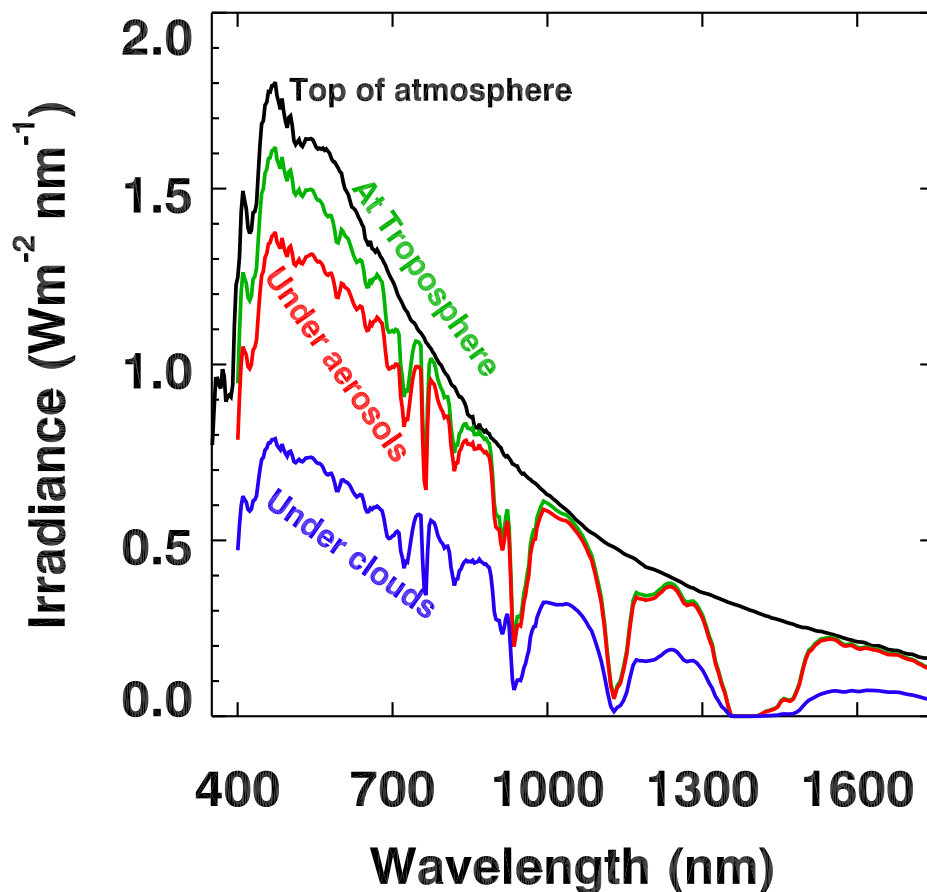


Figure 1.1: Shortwave irradiance spectra for a solar zenith angle of  $30^\circ$  incident at the top of atmosphere (in black), in the troposphere, but devoid of influences from aerosol or clouds (in green), under an aerosol layer with an optical thickness of 1 (in red), and under liquid clouds only with an optical thickness of 15 and effective radius of  $10 \mu\text{m}$  (in blue).

assumptions of spectrally constant properties that are required by retrievals based on broadband radiation measurements are no longer sources of uncertainty. By using spectrally resolved measurements, estimates of aerosol properties can be determined with smaller uncertainty than when using broadband measurements, since the spectral characteristics of the aerosol properties are indicative of aerosol type [e.g., *Bergstrom et al.*, 2007; *Russell et al.*, 2010; *Yu et al.*, 2009; *Kaufman et al.*, 2002]. Spectral features in cloud transmittance have been used to retrieve cloud particle effective

radius with higher sensitivity than other methods [McBride *et al.*, 2011]. Other spectral features in reflectance have been used to determine cloud thermodynamic phase [Pilewskie and Twomey, 1987].

### 1.3 Measurement and Instrumentation

To answer the science questions, new measurement systems and components were designed, built, and operated. A large part of the work required for the completion of this thesis involved the design, the manufacture, and the operation of measurement systems. The 3 most important contributions to measurement systems that were achieved during my time as a graduate student are: 1) building and operating the Skywatch observatory, 2) design, build, test, and deploy the light collector for measuring zenith radiance, and 3) contribute to the development and testing of an actively stabilized leveling platform for the irradiance light collector .

The Skywatch observatory (<http://skywatch.colorado.edu/>) is a set of instruments combined under the general guise of radiation and precipitation measurements for atmospheric science research. It is used as a teaching observatory and research facility. The Skywatch observatory is located on the roof of the Duane physics building at the University of Colorado, in Boulder, Colorado. It contains radiometers for measuring downwelling broadband shortwave (pyranometer) and longwave (pyrgeometer) radiation. It also contains spectrometers for measuring direct sun radiance spectra (sun photometer) , spectra of irradiance, and zenith radiance (Solar Spectral Flux Radiometer). Precipitation instruments include a zenith pointing rain radar, a ceilometer for determining cloud base height, a disdrometer for measuring drop size distributions, and a total precipitation gauge. There is also an ozone meter and a sky web cam. All instruments continuously collect data, which is available via the internet.

A narrow field-of-view collimating light collector is required to measure zenith radiance spectra. For a light collector to correctly sample radiance, it must only be sensitive to radiation within its field-of-view. The radiance as a function of the angle between incident light and the normal of the light collector is presented in Fig. 1.2. If the light collector is sensitive to radiation incident

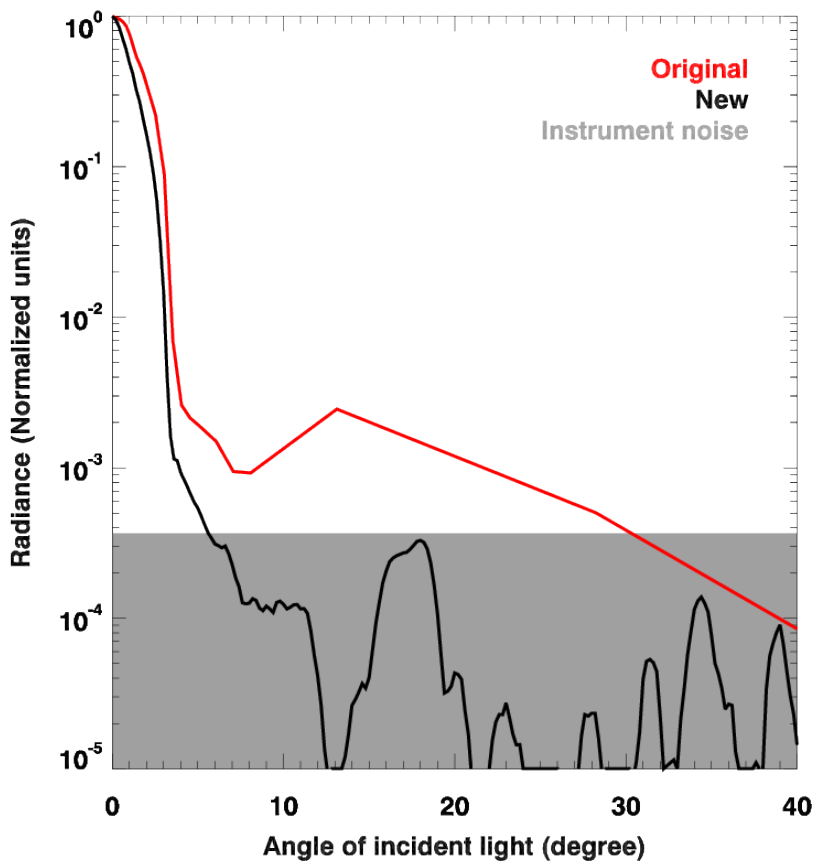


Figure 1.2: Radiance in a midvisible wavelength measured by the original and new narrow field-of-view light collector as a function of the angle between the incident light and the normal of the light collector. The radiance is presented as a fraction of the incident light at  $0^\circ$ .

from outside its field-of-view, the measure of radiance is erroneous because of this stray light. The original light collector is sensitive to light from up to  $30^\circ$  from the center of the field-of-view, even though its field-of-view was reported as  $2.8^\circ$  (red line in Fig. 1.2). Stray light in the transmitted radiance, such as the direct beam of the sun outside the field-of-view, used for remote sensing of cloud optical thickness, may have been falsely interpreted as cloud measurements when there were no clouds in partly cloudy skies [Chiu *et al.*, 2006, 2009; Marshak *et al.*, 2009; McBride *et al.*, 2011]. To resolve the problem, a collimating light collector was modified to reject all incident light that is not within the field-of-view. The original light collector contained a simple collimating lens focused on the entrance of a fiber optic bundle. A set of baffles in front of the lens was added to

the light collector to reduce stray light. The interior side walls of the light collector were threaded and coated by an absorbing black paint to further reduce stray light down to the noise floor of the spectrometer. The field-of-view of the new light collector was verified to be  $2.8^\circ$ . Incident radiance from outside this field-of-view is reduced below the noise floor of the instrument. The new light collector was used in this thesis to measure transmittance from which cloud microphysical and optical properties were extracted. The same light collector was also used by *McBride et al.* [2012].

The radiant energy flux contribution (per unit time and area) that is perpendicular to a horizontal plane defines irradiance. To measure irradiance, a light collector with a hemispherical field-of-view is used. If the irradiance light collector is not level with the horizon, light incident from the other hemisphere will also influence the measurement. Therefore, larger measurement uncertainty is obtained compared to when the light collector is parallel with the horizon. When measuring irradiance on an airborne platform, the light collector is typically mounted directly on the skin of the aircraft in a fixed position, where it follows the natural pitch and roll movements of the aircraft. To help reduce these uncertainties, a new actively stabilized platform was developed. Contributions to developing the leveling platform included building and testing the control software, and testing the leveling platform during field missions.

## 1.4 Overview

Each of the questions has been investigated in separate studies, presented in their entirety in the following three chapters. Chapter 2 details observations of airborne spectral irradiance that quantify aerosols from the Los Angeles basin, and northern Alberta, Canada. Chapter 3 and 4 refer to a new method to retrieve cloud optical and microphysical properties from transmitted spectral radiance. Chapter 3 introduces spectral features in ice or liquid water clouds spectral transmittance and their quantification. These features are used to retrieve cloud optical thickness, effective radius, and thermodynamic phase from radiance measurements for 3 cloud case studies. This new retrieval is then evaluated by quantifying the information content from the multiple spectral features in Chap. 4. By assuming naturally occurring variability in environmental conditions, which are

necessary inputs when modelling shortwave radiation, realistic uncertainties in cloud properties are derived. Sensitivity of spectral features to variability in environmental conditions, or non-retrieved information, is also quantified. A summary and outlook the thesis is presented in Chap. 5.

## Chapter 2

### Spectral aerosol direct radiative forcing from airborne radiative measurements during CalNex and ARCTAS

This study presents the aerosol radiative forcing derived from airborne measurements of shortwave spectral irradiance during the 2010 Research at the Nexus of Air Quality and Climate Change (CalNex). Relative forcing efficiency, the radiative forcing normalized by aerosol optical thickness and incident irradiance, is a means of comparing the aerosol radiative forcing for different conditions. In this study, it is used to put the aerosol radiative effects of an air mass in the Los Angeles basin in context with case studies from three field missions that targeted other regions and aerosol types, including a case study from the Arctic Research of the Composition of the Troposphere from Aircraft and Satellites (ARCTAS). For CalNex, we relied on irradiance measurements onboard the NOAA P-3 aircraft during a flight on 19 May 2010 over a ground station. CalNex presented a difficulty for determining forcing efficiency since one of the input parameters, optical thickness, was not available from the same aircraft. However, extinction profiles were available from a nearby aircraft. An existing retrieval algorithm was modified to use those measurements as initial estimate for the missing optical thickness. In addition, single scattering albedo and asymmetry parameter (secondary products of the method), were compared with CalNex in situ measurements. The CalNex relative forcing efficiency spectra agreed with earlier studies that found this parameter to be constrained at each wavelength within 20% per unit of aerosol optical thickness at 500 nm regardless of aerosol type and experiment, except for highly absorbing aerosols sampled near Mexico City. The diurnally averaged below-layer forcing efficiency integrated over the wavelength

range of 350-700 nm for CalNex is estimated to be  $-58.6 \pm 13.8 \text{ W/m}^2$ , whereas for the ARCTAS case it is  $-48.7 \pm 11.5 \text{ W/m}^2$ .

## 2.1 Introduction

Aerosols contribute the largest uncertainty to the net anthropogenic radiative forcing of climate [Forster *et al.*, 2007]. Aerosol particles can directly modify the net irradiance, which is a measure of the net radiative energy density. This is termed the aerosol direct radiative forcing. Aerosol direct radiative forcing may offset global carbon dioxide forcing by 5 to 50% [Forster *et al.*, 2007], making its understanding crucial for characterizing climate change. The global annually averaged aerosol direct radiative forcing at the top of the atmosphere is determined by models utilizing in situ and satellite measurements [Bellouin *et al.*, 2005; Chung *et al.*, 2005]. However, the use of models with their associated uncertainties largely contribute to the uncertainty of this forcing [Yu *et al.*, 2006; Remer and Kaufman, 2006; Forster *et al.*, 2007]. The forcing uncertainties are large in part because they are often derived indirectly from remote sensing or in situ measurements of aerosol optical thickness, single scattering albedo, and asymmetry parameter [Massoli *et al.*, 2009]. Reducing model uncertainties, improving satellite observations, and continuing intensive airborne studies are all needed to reduce forcing uncertainty.

In the past, multiple airborne studies directly measured atmospheric irradiance and aerosol optical thickness, which provided a more accurate estimation of the local aerosol direct radiative forcing [Redemann *et al.*, 2006]. One such method is presented in this current work. These studies determined the aerosol direct radiative forcing for some specific time, region, and prevailing aerosol type [Redemann *et al.*, 2006; Schmidt *et al.*, 2010; Bergstrom *et al.*, 2003]. Uncertainties of simulated aerosol radiative forcing can be minimized by tying these values to measurements of irradiance at specific levels of the atmosphere and regions, or by validating the simulated aerosol radiative forcing with observations [Magi *et al.*, 2008].

Table 2.1: Input and output of different methods used to obtain layer-averaged aerosol optical properties as well as relative forcing efficiency ( $f_e$ ) from airborne spectral irradiance ( $F$ ) and aerosol optical thickness ( $\tau$ ) measurements

Methods	Required Input		Output				Comments
	$\tau$	$F$	$f_e$	$\varpi$	$g$	$\alpha$	
<i>Redemann et al.</i> [2006]	X	X	X	X		X	When aerosol optical properties and surface albedo stay constant
<i>Bergstrom et al.</i> [2003]	X	X		X			Based on deriving the amount of absorption in a layer
<i>Schmidt et al.</i> [2010]	X	X	X	X	X	X	Based on deriving the amount of absorption, transmission, and reflection in a layer
Current Method	X	X	X	X	X	X	Similar to <i>Schmidt et al.</i> [2010], but $\tau$ only needs to be an initial approximation.

### 2.1.1 Radiative Forcing

Instrument uncertainties and various assumptions in aerosol retrieval models propagate to uncertainties in calculated radiative forcing [*Magi et al.*, 2008]. Although direct measurement of aerosol direct radiative forcing would be the preferred path to reduce these uncertainties, it is impossible to measure forcing directly. Aerosol radiative forcing is the change to net radiation due to aerosols. Its determination would require simultaneous measurements of atmospheric radiation in the presence and absence of aerosols, which is physically impossible. Previously, the radiative forcing was estimated by measuring the change of net irradiance along a gradient in aerosol optical thickness, with the restriction that aerosol intensive properties and surface albedo stay constant [e.g., *Redemann et al.*, 2006].

Another method to obtain aerosol direct radiative forcing was developed by *Schmidt et al.* [2010], adapted from *Bergstrom et al.* [2003]. *Schmidt et al.* [2010] used airborne spectral irradiance ( $F$ ) and spectral aerosol optical thickness ( $\tau$ ), which, if not measured directly [e.g., *Redemann et al.*, 2006], can be determined by a combination of aerosol optical thickness at one wavelength and the extinction Ångström exponent ( $a$ ). These measurements of irradiance above and below an aerosol layer were used to derive aerosol radiative properties and surface albedo ( $\alpha$ ). The derived aerosol

radiative properties (described in detail in 2.7) were the aerosol single scattering albedo ( $\varpi$ ) and the asymmetry parameter ( $g$ ). These radiative properties along with the aerosol optical thickness were then used as inputs in a radiative transfer model to calculate spectral irradiance in the presence of the aerosol layer under study, while the clear sky spectral irradiance was calculated using only the retrieved surface albedo. The difference between the simulated irradiance with and without aerosol gives the aerosol direct radiative forcing. A comparison of the different methods used to obtain aerosol direct radiative forcing, including the one presented in this work, is presented in Table 2.1.

### 2.1.2 Relative Forcing Efficiency

Aerosol direct radiative forcing ( $f$ ) is the change in net irradiance due to aerosols,  $f = F_{net,aerosols} - F_{net,clear}$ . It can be defined at different time scales (such as instantaneous, diurnal, or since the pre-industrial period) and at different levels of the atmosphere (top of the atmosphere, at the tropopause, top of the layer, below a layer, or at the surface). In this study, the focus is on instantaneous radiative forcing above and below aerosol layers. Aerosol direct radiative forcing depends on aerosol optical thickness and incident irradiance at the top of the layer. Forcing efficiency, the radiative forcing normalized by aerosol optical thickness at 500 nm, was introduced by *Meywerk and Ramanathan* [1999] to reduce large variability in aerosol loading which affects the comparison of forcing for different cases. Relative forcing efficiency ( $f_e$ ) [*Redemann et al.*, 2006]:

$$f_e = \frac{f}{\tau_{500nm} F_{top}^{\downarrow}} \times 100\% \quad (2.1)$$

is a measure of the radiative forcing as a percentage of the incident irradiance and per unit of midvisible aerosol optical thickness ( $\tau_{500nm}$ ) (normalized by the incident irradiance at the top of the layer [ $F_{top}^{\downarrow}$ ]).

The aerosol direct radiative forcing can vary considerably between different types of aerosol and their regions. Since the first-order dependence of this forcing on aerosol optical thickness and incident irradiance above the aerosol layer is removed in the relative forcing efficiency, this enables us to compare the forcing from various different regions of the world on the same scale. Although

the relative forcing efficiency removes much of the dependencies to the solar zenith angle, there are still some second order effects related to the optical path, such as differences in multiple scattering. Regardless of these second order effects, relative forcing efficiency provides a more uniform basis of comparison of the aerosol's effect on radiation from various regions than the aerosol's direct forcing itself.

### **2.1.3 This Study**

This study focuses on the derived relative forcing efficiency from data collected during an intensive field campaign in the Los Angeles basin. In addition, this study shows a comparison of the CalNex relative forcing efficiency to that from other similar regional studies. Using measurements of spectral irradiance from the Solar Spectral Flux Radiometer (SSFR; presented in section 2.2.1) and profiles of aerosol extinction from the High Spectral Resolution Lidar (HSRL) (presented in section 2.2.2), relative forcing efficiency is determined from measurements taken during the Research at the Nexus of Air Quality and Climate Change (CalNex) (presented in section 2.3) intensive field campaign. Relative forcing efficiency is derived via a modified retrieval of aerosol single scattering albedo, optical thickness, asymmetry parameter and surface albedo (presented in Sect. 2.8). These new analysis tools are introduced to accommodate the incomplete (spectrally) and non-concurrent measurements of aerosol optical thickness. These tools are tested with concurrent measurements of aerosol optical thickness and spectral irradiance taken during another intensive field mission with similar instrumentation, the Arctic Research of the Composition of the Troposphere from Aircraft and Satellites (ARCTAS) based in Cold Lake, Alberta, Canada. Relative forcing efficiency spectra calculated from the measurements taken during these two field campaigns (CalNex and ARCTAS) and other field campaigns are presented in section 2.4.

## **2.2 Instrumentation and Radiative Transfer Model**

Measurements of solar spectral irradiance taken during CalNex are used as input to a retrieval algorithm that determines the relative forcing efficiency. Both the SSFR, which measures solar

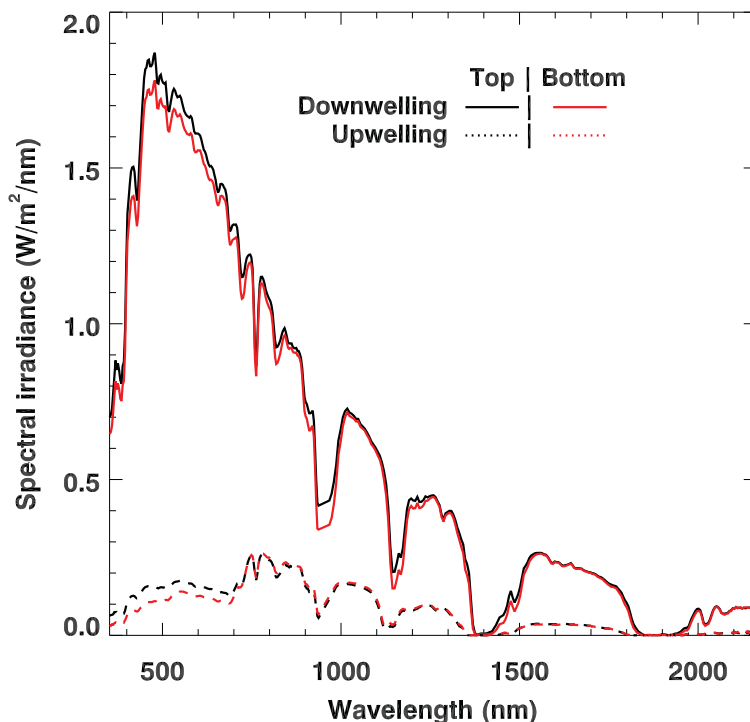


Figure 2.1: Upwelling and downwelling irradiance spectra from 1.6 km West of Caltech measured at the top flight leg ( $\sim 1000\text{m}$  altitude) and the bottom flight leg ( $\sim 500\text{m}$  altitude) with the Solar Spectral Flux Radiometers (SSFR) during the Research at the Nexus of Air Quality and Climate Change field mission (CalNex). Solar spectral irradiance that is transmitted through part of the atmosphere is labeled downwelling. Upwelling spectral irradiance shows the influence of reflectance from the underlying surface.

spectral irradiance, and the radiative transfer model, which is used in the retrieval algorithm, are presented below. Ancillary instruments are also presented below.

### 2.2.1 Solar Spectral Flux Radiometer

The SSFR [Pilewskie *et al.*, 2003] is a moderate spectral-resolution (8 to 12 nm) instrument designed to measure solar spectral irradiance under varying atmospheric conditions. The SSFR is composed of two pairs of spectrometers for acquiring zenith and nadir irradiance over the nearcomplete shortwave spectrum (350–2150 nm). The SSFR has a precision of 0.1–0.2%, represented by the standard deviation of a collection of spectra with SSFR illuminated by a stable lamp source. Radiometric uncertainty is 3 to 5% across the spectrum, determined primarily by a NIST-traceable

lamp used for calibration. Fiber optic bundles connect aircraft skinmounted hemispheric light collectors to the rack-mounted spectrometers in the aircraft cabin. The light collectors measure full hemispheric ( $2\pi\text{sr}$ ) downwelling and upwelling spectral irradiance. Spectral irradiance measurements are subject to larger uncertainty when fix-mounted on an aircraft surface that deviates from level attitude in flight. Sample irradiance spectra from the SSFR from a scene over Ontario, California, during CalNex are shown in Fig. 2.1.

### 2.2.2 Ancillary Instruments

Measurements of spectral irradiance alone are not sufficient to be able to quantify the relative forcing efficiency of aerosols. Measurements of the aerosol layer optical thickness are also required. During CalNex, the HSRL [Hair *et al.*, 2008] provided profiles of aerosol extinction coefficients at a wavelength of 532 nm. This highly robust downward pointing lidar, which is radiometrically calibrated internally, also provides aerosol backscatter and aerosol depolarization at two wavelengths. During ARCTAS, the NASA Ames 14-channel Airborne Tracking Sunphotometer (AATS-14) [Redemann *et al.*, 2005; Shinozuka *et al.*, 2011] was used to determine the aerosol optical thickness above the aircraft level. Additionally, measurements of the entire column’s aerosol optical thickness, single scattering albedo, asymmetry parameter, and Ångström exponent is returned from an Aerosol Robotic Network (AERONET) sunphotometer [Holben *et al.*, 1998].

In situ measurements of microphysical and optical properties of aerosol particles are used to compare secondary products (single scattering albedo and asymmetry parameter) obtained when determining relative forcing efficiency. Optical aerosol properties were provided by five instruments onboard the NOAA P-3. The Cavity Ring Down aerosol extinction Spectrometer (CRDS) [Langridge *et al.*, 2011] measured total dry aerosol light extinction at 532, 405 and 662 nm and the dependence of extinction on relative humidity. The Photoacoustic Absorption Spectrometer (PAS) [Lack *et al.*, 2012] measured total dry aerosol light absorption at the same wavelengths as the CRDS. Aerosol size distributions with particle diameters of 4–6300 nm weremeasured using the combination of a White-Light Optical Particle Counter (WLOPC) [Brock, 2003], an Ultra High

Sensitivity Aerosol Size spectrometer (UHSAS) [Brock, 2004], and a Nucleation Mode Aerosol Size Spectrometer (NMASS) [Brock, 2004]. Aerosol extinction at ambient humidity conditions is derived from these measurements using kappa-Köhler theory [Petters and Kreidenweis, 2007].

### 2.2.3 Radiative Transfer Model

The radiative transfer model used in this retrieval is the N-stream DISORT [Wiscombe and Grams, 1976] with SBDART [Ricchiuzzi et al., 1998] for atmospheric molecular absorption, which is publicly available within LibRadtran [Mayer and Kylling, 2005]. The extraterrestrial solar spectral irradiance was taken from Kurucz [1994] at 1-nm spectral resolution. Mie scattering calculations were used to obtain the optical properties of aerosol particles using the in situ measurements. Wiscombe [1979] describes the code that calculates Mie scattering.

## 2.3 Research at the Nexus of Air Quality and Climate Change

CalNex was conducted in California during May and June 2010. Its primary focus was the impact of trace gases and aerosols from urban-industrial pollution on air quality and climate-relevant parameters (specifically, direct and indirect aerosol radiative forcing) in the state of California and the eastern Pacific coastal regions. Multiple aircraft, one research ship, two major ground measurement sites, tall instrumented towers, ozone sondes, satellite instruments, and forecast models were involved in this multiagency effort. Data taken from instruments situated on two of the research aircrafts and one of the major ground sites are presented in this study.

Radiative measurements were taken onboard the NOAA WP-3D research aircraft (hereafter, P-3), along with the contingent of cloud probes, gas-phase chemistry, aerosol optical properties, and meteorological instruments. The P-3 flew a suite of radiation instruments that measured solar spectral irradiance, spectral actinic flux, as well as solar and infrared broadband irradiance. The primary radiation measurements applied in this study were spectral irradiance, acquired from the SSFR.

In situ measurements of microphysical and optical properties of aerosol particles were acquired

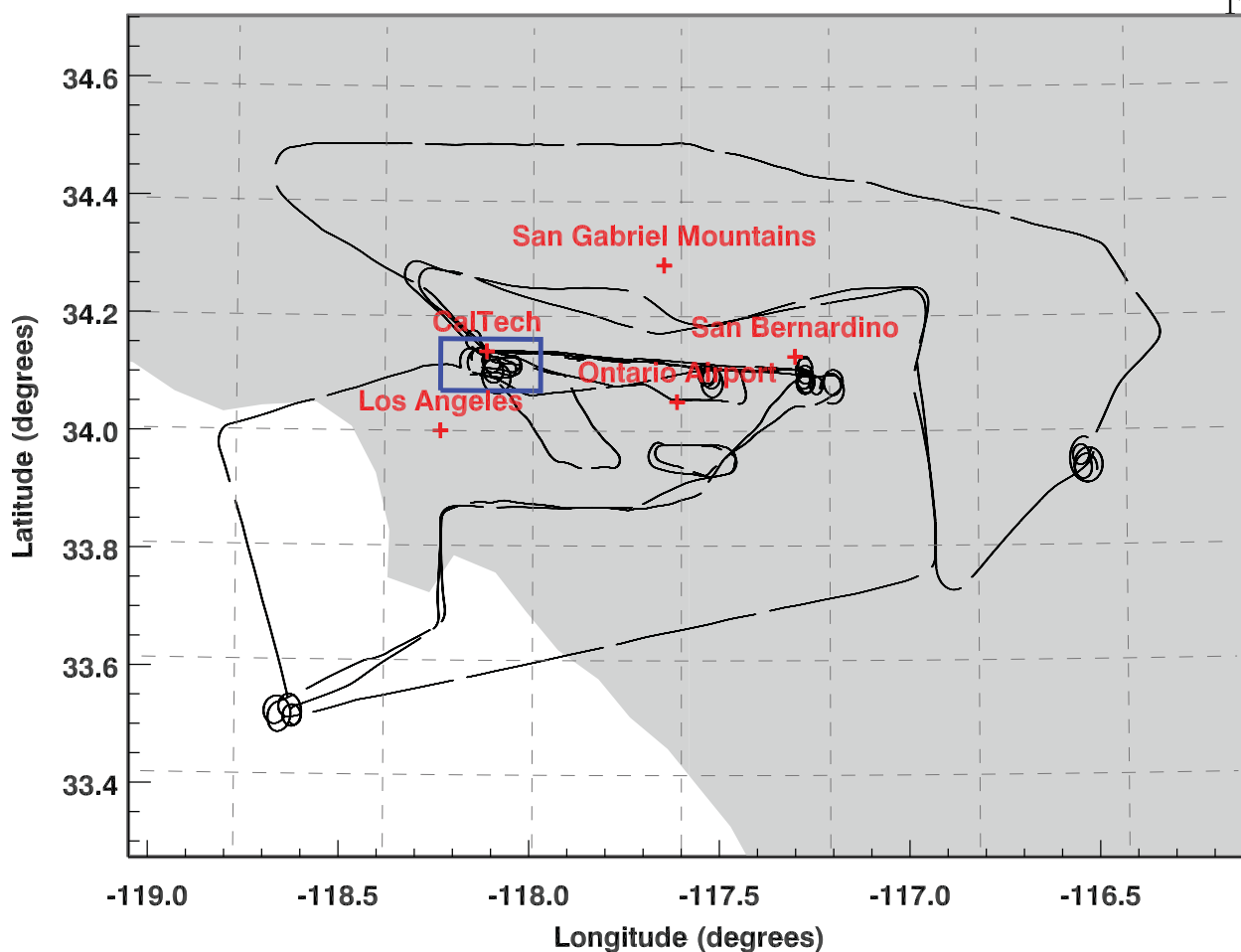


Figure 2.2: Map of the P-3 airborne platform's flight path around the Los Angeles region on 19 May 2010. The start and end of the flight path (center of the plot) is located in Ontario, California. The flight legs of interest in this figure are located near the Caltech ground site (blue square).

from the CRDS, PAS, WLOPC, UHSAS, and NMASS located on the P-3. Other measurements were taken by the HSRL onboard the NASA King Air B-200 (hereafter, NASA King Air) and by AERONET at the Caltech ground site in Pasadena, California.

In this work we focus on one case on 19 May 2010 (flight track in Fig. 2.2), when the P-3 encountered cloudfree conditions and high aerosol concentrations, which is compared to flights from other field missions. On this day, the plane sampled the outflow of pollution from the Los Angeles basin across the San Gabriel mountain range, which runs east-west just north of San Bernardino. Flight legs in smog conditions over the Caltech ground site in Pasadena were coordinated with

the NASA King Air. Above the Caltech ground site, the P-3 flew a series of stacked level legs within 30 min of the NASA King Air. A comparison between ambient aerosol extinction, derived from in situ measurements, and the aerosol extinction profile from the HSRL on board the NASA King Air (stacked-level flight legs, shown in Fig. 2.3a and 2.3b) shows general agreement. General agreement has also been observed during CalNex between the integrated aerosol extinction profile measured by HSRL and aerosol optical thickness measured by AERONET. We note that in situ measurements of aerosol extinction were generally lower than extinction measured remotely by the HSRL. This was possibly due to the influence of particles larger than 2 microns diameter, which were not sampled by the CRDS but were often present during CALNEX. The layer-integrated aerosol extinction profile (between 400 and 800 m) measured by HSRL was equivalent to an aerosol optical thickness of approximately 0.13; the layer-integrated aerosol extinction measured by CRDS is approximately 0.16. In contrast, the total column aerosol optical thickness at 500 nm measured by AERONET is approximately 0.34. Since AERONET samples the entire column, including the near surface layer, while the other measurement methods sample the 400–800 m layer, a higher aerosol optical thickness is expected. In this layer, the measured depolarization values (at 532 nm) were  $<0.05$ , therefore the majority of aerosol particles were spherical.

## 2.4 Results and Discussion from CalNex: 19 May 2010

Relative forcing efficiency has been retrieved for the CalNex case study on 19 May 2010 and for the ARCTAS case on 9 July 2008 and compared to values from different regions. For the CalNex case study secondary products of aerosol optical properties and surface albedo have been retrieved using the algorithm modified from *Schmidt et al.* [2010] described in 2.8. In this algorithm, aerosol optical thickness is retrieved when the values of the asymmetry parameter determined from transmittance and reflectance converge to a single value. These properties, along with single scattering albedo and surface albedo are determined by matching modeled spectral irradiance to its measurement above and below an aerosol layer. To measure upwelling and downwelling irradiance above and below an aerosol layer with a single aircraft, a flight path of stacked level legs is required.

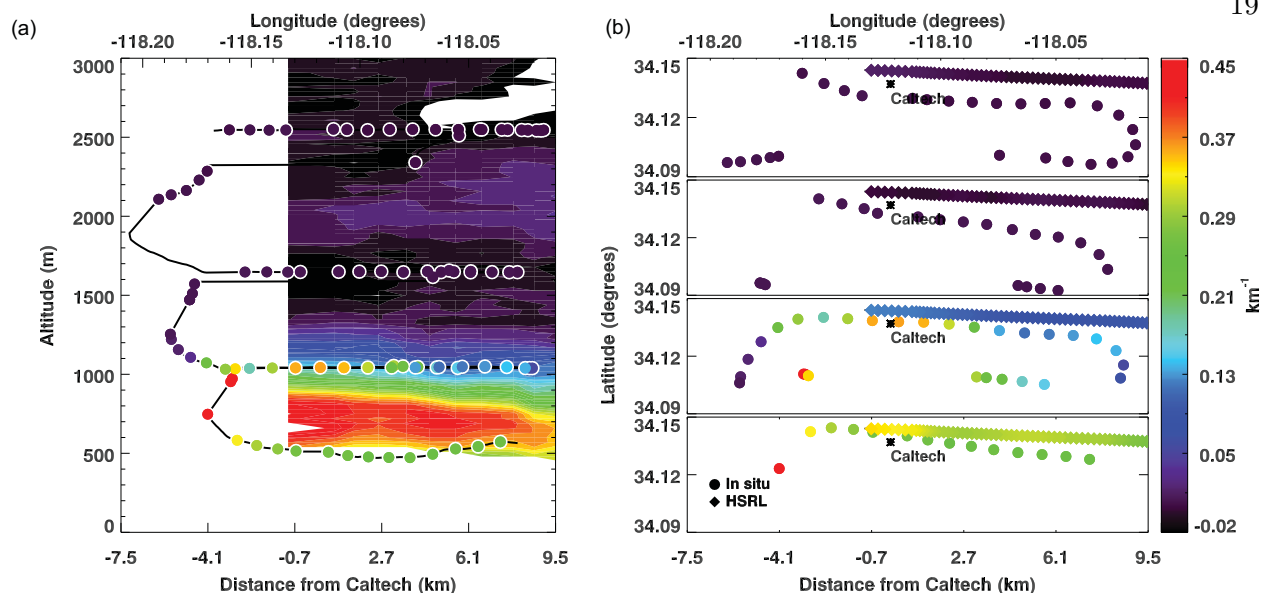


Figure 2.3: Profiles of in situ measured-extinction coefficients from the P-3 flight track (circles) and extinction coefficients derived from the High Spectral Resolution Lidar (HSRL, diamonds) at 532 nm at ambient humidity. (a) Vertical profile of aerosol extinction coefficients (lidar curtain) overlaid with the in situ extinction coefficient (point measurements) along the flight track. (b) In situ extinction coefficient maps at each altitude (2000–3000 m, 1500–2000 m, 800–1400 m, 400–800 m from top to bottom respectively) measured at approximately 5 min intervals for approximately 20 min).

A diagram of the measurement geometry used in this method is presented in Fig. 2.4. This method can be applied to the entire spectral range of SSFR, from 350 to 2150 nm. However, above 1050 nm the aerosol radiative effect is not significant compared to the radiometric uncertainty. Therefore, we only analyzed a limited wavelength range from 350 to 1050 nm.

#### 2.4.1 Spectra of Retrieved Aerosol Properties

The spectra of retrieved parameters for 19 May 2010 over the Caltech ground site are presented in Fig. 2.5. Aerosol single scattering albedo ( $\varpi$ ), asymmetry parameter ( $g$ ), optical thickness ( $\tau$ ), and surface albedo ( $\alpha$ ) all lie within plausible ranges (see Fig. 2.5a). Single scattering albedo values (black) lie within the range 0.85–0.98 throughout most of the spectrum. In comparison, various types of aerosol show different spectral single scattering albedo, both in shape and value, as compared to those sampled during CalNex. For the aerosol sampled during ARCTAS, its single

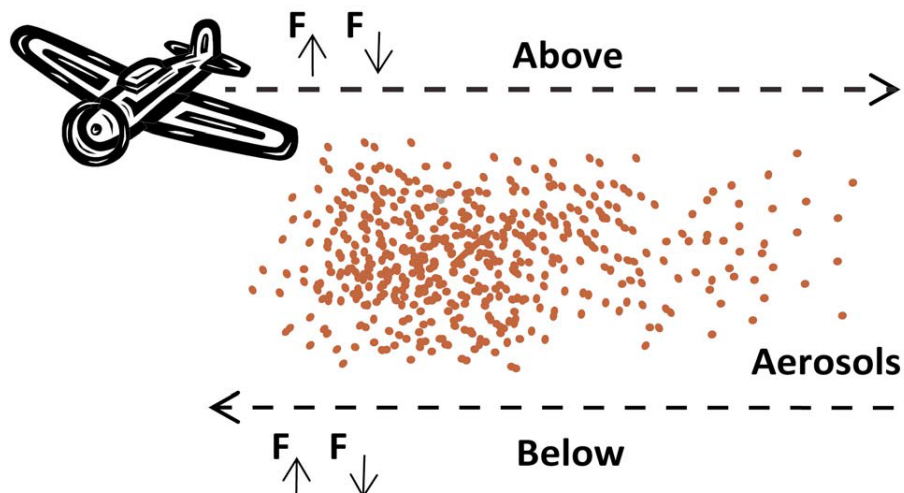


Figure 2.4: Flight leg geometry used to characterize aerosol properties within the aerosol layer. The dashed lines represent the aircraft flight altitude above and below the aerosol layer.

scattering albedo increases from 0.85 to 0.92 and then decreases to 0.8 at 350 nm, 550 nm, and 1050 nm respectively. For another field mission, the Megacity Initiative: Local and Global Research Observations (MILAGRO) near Mexico City [Schmidt *et al.*, 2010], the single scattering albedo for freshly emitted highly absorbing aerosol decreases from 0.85 at 350 nm to 0.7 at 1050 nm. For slightly aged aerosols sampled during MILAGRO, the single scattering albedo increases from 0.85 at 350 nm to a near constant 0.9 at longer wavelengths. A broadband estimate of single scattering albedo from another field mission, the Intercontinental Chemical Transport Experiment - North America (INTEX-NA) over the Gulf of Maine [Redemann *et al.*, 2006], reports values between 0.88 to 1.00, which is similar to the range of spectral values reported for CalNex. The retrieved spectral asymmetry parameter for aerosol sampled during CalNex decreases from 0.8 at 350 nm to a constant 0.6 at 700–1050 nm. A decreasing asymmetry parameter with increasing wavelength is also observed during MILAGRO, where slightly aged and highly absorbing aerosol's asymmetry parameter decreased from 0.8 at 350 nm to 0.55 at 850 nm and 0.95 at 350 nm to 0.74 at 600 nm respectively. For the ARCTAS case, the asymmetry parameter decreases from 0.75 at 350 nm to 0.65 at 550 nm and then increases to 0.95 at 1050 nm. For CalNex, the surface albedo spectrum (blue) shows a pattern that resembles a mixed vegetation scene (increase in near infrared [Horler

*et al.*, 1983]). The aerosol optical thickness (red curve, right axis) exponentially decreases with increasing wavelength, typical for ambient aerosol particle extinction. A similar spectral shape of aerosol optical thickness is also observed for cases from ARCTAS, MILAGRO and INTEX-NA. The spectral absorption, measured during CalNex (red spectrum in Fig. 2.5b), matches the modeled spectral absorption at the wavelengths denoted by the black dots, as required for a successful retrieval. Since we assume a plane parallel, horizontally homogeneous aerosol layer, there is no net horizontal transport of photons, thus the absorbed spectral irradiance of a layer is equivalent to the vertical flux divergence. The difference between above- and below-layer net spectral irradiance (derived from the irradiances shown in Fig. 2.1) is the absorbed spectral irradiance of this layer. The absorbed spectral irradiance at longer wavelengths ( $>600$  nm) is lower than the absorbed spectral irradiance at shorter wavelengths ( $<600$  nm). Although the measurement uncertainty over this range is nearly constant, the relative uncertainty increases with lower absorbed spectral irradiance, consequently the relative uncertainty in the retrieved properties is also increased (larger shaded area at higher wavelengths in Fig. 2.5a).

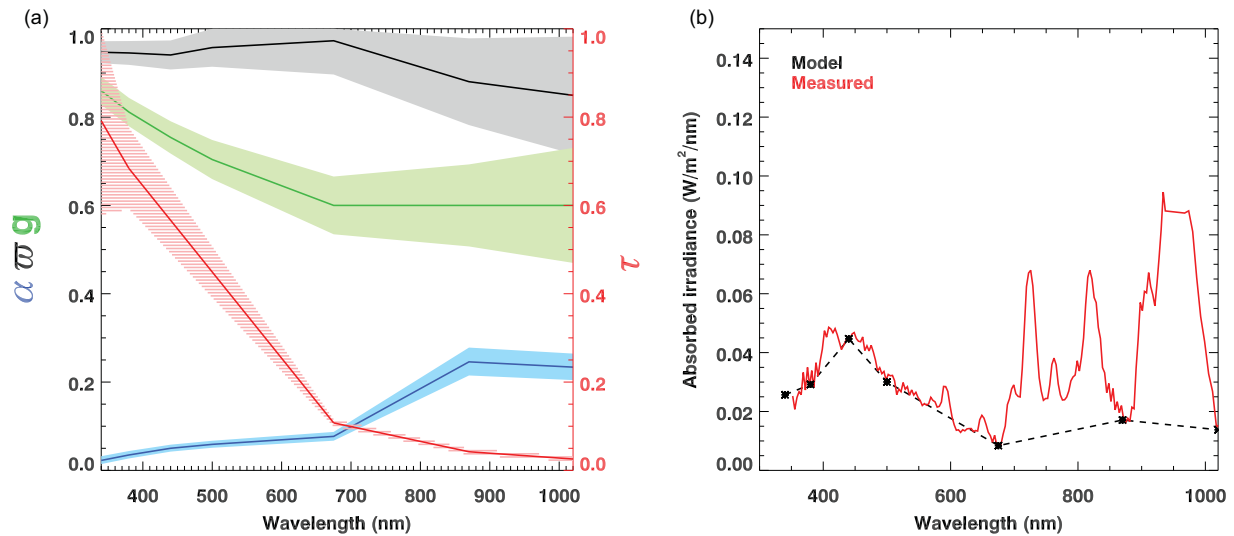


Figure 2.5: Retrieved aerosol single scattering albedo, asymmetry parameter, optical thickness, and surface albedo, and measured absorption for a single point 1.6 km west of Caltech during the CalNex case of 19 May 2010. (a) Retrieved secondary properties where the shading denotes their uncertainty range. (b) Measured and modeled absorption. Modeled values (at the discrete points) are outside of gas absorption bands. Dashed lines are interpolations between window values.

### 2.4.2 Retrieved Along-Path Aerosol Properties

Spatial variations of the retrieved parameters at two wavelengths can be seen by the colored lines as a function of the distance from the Caltech ground site along the flight path in Fig. 2.6. The single scattering albedo, evaluated at 380 nm, ranges from 0.84 (high absorption) to 0.96 (moderate absorption). The mean asymmetry parameter of this aerosol layer, evaluated at 380 nm, is around 0.85, which is higher than the value typically associated with an urban environment of 0.74 (determined at 440 nm [Dubovik *et al.*, 2002, Fig. 10a]). Nevertheless, the spectral shape of asymmetry parameter (decreasing with longer wavelengths) does coincide with observations from urban environments observed in worldwide locations from AERONET [Dubovik *et al.*, 2002]. The higher value, compared to AERONET asymmetry parameter indicates stronger forward scattering and suggests larger aerosol particles than found from other urban environments (Greenbelt, Maryland, USA; Crete-Paris, France; Mexico City, Mexico; Maldives). Aerosol optical thickness, single scattering albedo, and asymmetry parameter exhibit variability throughout the flight leg, while the surface albedo stays fairly constant. In some cases, such as about 6 km east from the Caltech ground site, a noticeable change in the single scattering albedo and the asymmetry parameter at 500 nm coincide with the location of major roads in Pasadena. At this location, and a few others, single scattering albedo is lower than the average, thus signifying an increase in light absorption of these aerosol particles. Toward the west of the Caltech ground site, the airborne video of the surface shows an increase in vegetation. This increase in vegetation can be seen by the increased separation between the surface albedo at 380 nm and 870 nm, which is indicative of vegetation's spectral reflectance feature, the near-IR edge. This retrieved surface albedo thus reflects the changes in the physical environment.

### 2.4.3 Retrieved Relative Forcing Efficiency

The aerosol direct radiative forcing is derived by calculating the spectral irradiance with and without aerosols, following the method described by Schmidt *et al.* [2010]. A negative direct

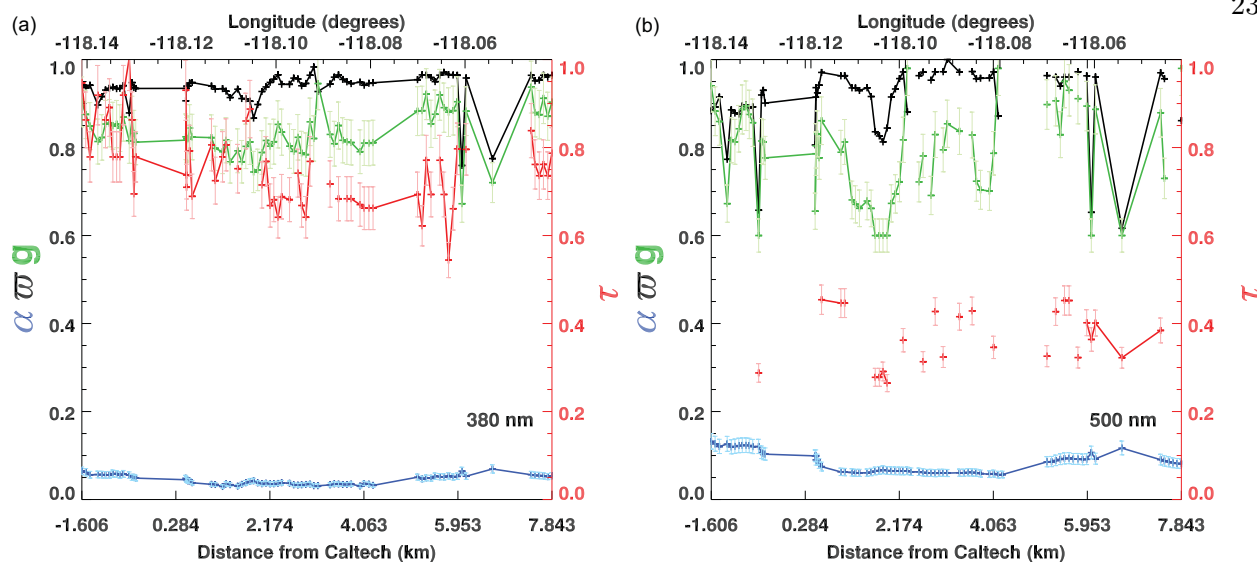


Figure 2.6: Retrieved aerosol single scattering albedo ( $\varpi$ , in black), asymmetry parameter ( $g$ , in green), optical thickness ( $\tau$ , in red), and the surface albedo ( $\alpha$ , in blue) for two wavelengths, (a) 380 nm and (b) 500 nm, along the flight path over Caltech during CalNex flight on 19 May, 2010. The x-axis represents the distance from Caltech (west to east), and the y-axis represents the magnitude of the retrieved properties. Blank spaces indicate when the retrieval failed to converge.

radiative forcing represents a negative change in the net irradiance, and therefore cooling, while a positive direct radiative forcing represents heating. The same is true for relative forcing efficiency. The resulting aerosol relative forcing efficiency from CalNex is shown in Fig. 2.7. The separation between the above- and below-layer relative forcing efficiency is a relative indication of the amount of absorption of within that layer. Even though the above- and below-layer forcing evaluated at 500 nm (Fig. 2.7a) vary considerably, their difference remains fixed, except when there is increased absorption. The dips of relative forcing efficiency and the increased absorption coincide with the lower values of single scattering albedo at 500 nm, specifically near a major road in Pasadena (6 km east of Caltech). These dips of relative forcing efficiency are related to cooling, both above the layer and more significantly below the layer. At the same time, they are indicator of increased warming within the layer.

The relative spectral forcing efficiency from measurements taken during CalNex and other field missions, including ARCTAS, is shown in Fig. 2.7b. The relative forcing efficiency spectra

from CalNex are compared to those from MILAGRO over the Gulf of Mexico, INTEX-NA off the coast of Maine, and ARCTAS in northern Alberta. The comparison reveals that the general spectral shape of the above- and below-layer forcing during CalNex is similar to those derived for the other field missions. For example, near the pollution sources during MILAGRO, freshly emitted and highly absorbing aerosols were measured. There were also slightly aged aerosols, measured at a larger distance from the same aerosol source. The relative forcing efficiency from an aged aerosol plume measured during MILAGRO agrees with the average relative forcing efficiency from the urban aerosols measured during CalNex.

The relative forcing-efficiency spectra from the various experiments have similar magnitude and spectral shapes. These similarities suggest that for the field experiments under study, relative forcing efficiency at any one wavelength between 350–1050 nm is constrained within 20% per unit of midvisible aerosol optical thickness regardless of aerosol type, except for highly absorbing aerosol.

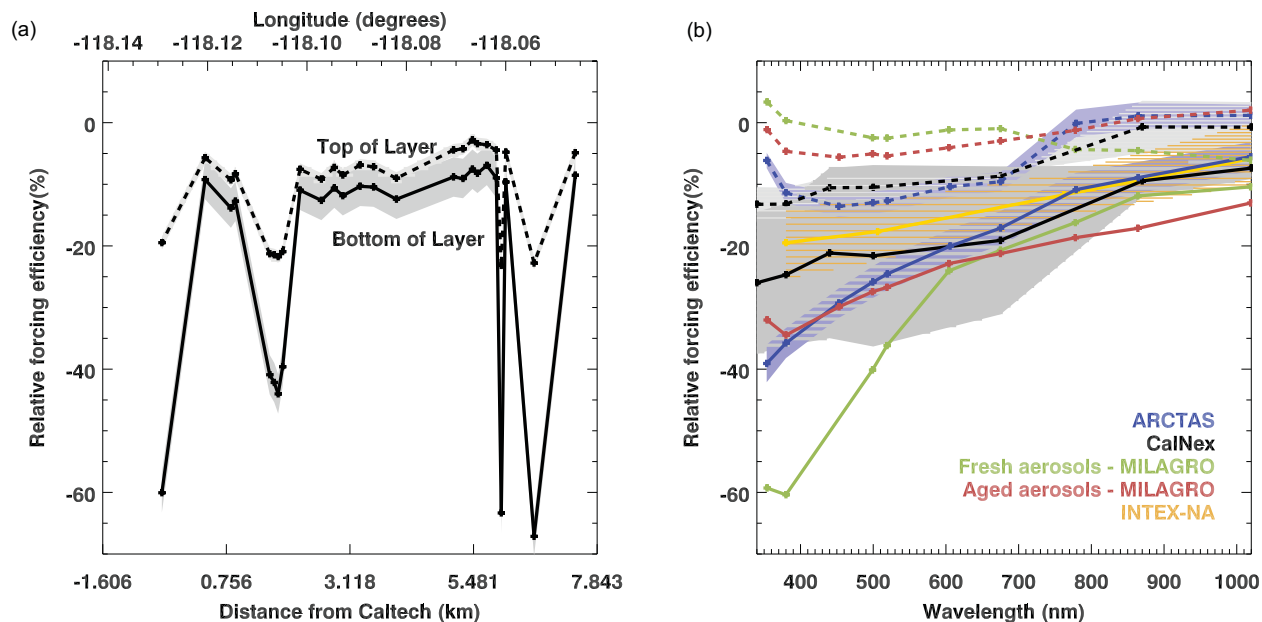


Figure 2.7: Aerosol direct radiative forcing for (a) along-flight, at 500 nm, and (b) the spectral averages over the entire flight leg. In (b) results from ARCTAS, MILAGRO [Schmidt *et al.*, 2010], and INTEX-NA [Redemann *et al.*, 2006] are shown for comparison. The shading in (a) represents the relative forcing efficiency uncertainty; in (b) it represents the standard deviation over the flight legs. Dashed lines are above-layer forcing, solid lines, below-layer forcing.

The below-layer relative forcing efficiency spectra increases with increasing wavelength, but always represents cooling, even when the value and spectral shape of single scattering albedo, asymmetry parameter and surface albedo differs. The recurring spectral shape of the relative forcing efficiency may be due to aerosol optical thickness since it is the only optical property that does not change spectral shape between the various experiments. The relative forcing efficiency at each wavelength varies by no more than 20% per unit of midvisible aerosol optical thickness for all missions indicated in Fig. 2.7b, with the exception of the freshly emitted aerosols shown for the MILAGRO case. The entire range of below-layer relative forcing efficiency at all wavelengths goes from -5% to -60% per unit of midvisible aerosol optical thickness. The above-layer relative-forcing efficiencies also have similar spectral shapes. Starting from near 0% at 350 nm, the above-layer relative forcing efficiencies decreases to their lowest values near 500 nm and then increases with increasing wavelength. These values all lie between -15% to +5% per unit of midvisible aerosol optical thickness with the largest spread between experiments at the lowest wavelengths. These above-layer forcings are modulated by the change in the upwelling irradiance. For aerosol similar to those sampled during CalNex, a modeled change in upwelling irradiance at 500 nm due to the aerosols is about -7.5% per unit of midvisible aerosol optical thickness [Russell *et al.*, 1997]. Although this is only an approximation, the modeled change in upwelling irradiance per unit of midvisible aerosol optical thickness is within one standard deviation of the measured mean above-layer relative forcing efficiency.

#### 2.4.4 Corresponding Diurnal Average of Forcing Efficiency

In order to compare the instantaneous spectral relative forcing efficiency to other often reported values of broadband diurnally averaged forcing efficiency, we used a conversion method described below. The instantaneous spectral relative forcing efficiency was multiplied with the downwelling irradiance above the aerosol layer to compute the instantaneous spectral forcing efficiency. The instantaneous broadband forcing efficiency is then calculated by integrating the resulting spectral forcing efficiency over the wavelength range of 350–700 nm. The conversion

of the instantaneous broadband forcing efficiency to its diurnal average was done by using the well-confined ratios calculated by *Redemann et al.* [2006]. These ratios represent the below-layer relationship between instantaneous broadband forcing efficiency at various solar zenith angles to diurnally averaged values. The diurnally averaged broadband forcing efficiency at the bottom of the aerosol layer for the CalNex case is  $-58.6 \pm 13.8 \text{ W/m}^2$ , whereas for the ARCTAS case it is  $-48.7 \pm 11.5 \text{ W/m}^2$ . Other radiometrically determined estimates of diurnally averaged forcing efficiency show  $-45.8 \pm 13.1 \text{ W/m}^2$  for INTEX-NA,  $-48 \text{ W/m}^2$  from broadband (400–700 nm) irradiance measured during an Indian ocean experiment by *Meywerk and Ramanathan* [1999],  $38.5 \pm 4.0 \text{ W/m}^2$  and  $42.2 \pm 4.8 \text{ W/m}^2$  from ground-based radiometer measurements of broadband (400–700 nm) irradiance taken during the Indian ocean experiment and another in Asia by *Bush and Valero* [2002]; *Bush* [2003]. Although CalNex represents the highest below-layer diurnally averaged forcing efficiency presented here, its uncertainty falls within the reported values from ARCTAS, INTEX-NA, and the Indian Ocean experiment.

## 2.5 Summary and Discussion

Measurements by SSFR deployed on the P-3 during the field mission CalNex were used to derive relative forcing efficiency and its spectral dependence. A comparison of this spectral relative forcing efficiency to those from other field missions, including ARCTAS, reveals that for these cases, the relative forcing efficiency at each wavelength vary by no more than 20% per unit of midvisible aerosol optical thickness, with the exception of highly absorbing urban-industrial aerosol.

Previous algorithms for determining relative forcing efficiency required measurements of spectral irradiance and optical thickness as inputs. During CalNex, no concurrent measurements of aerosol optical thickness were available on one aircraft (P-3). Instead, profiles of aerosol extinction coefficients were available from an HSRL onboard a separate platform (NASA King Air). To derive relative forcing efficiency, an existing algorithm was modified to use the extinction-coefficient profile from HSRL. We adjusted this profile for the temporal and spatial displacement of the P-3 and the NASA King Air and to extend this profile to other wavelengths. In addition to relative forcing

efficiency, the algorithm provides spectral single scattering albedo, the asymmetry parameter, and the effective surface albedo. We tested our retrieval with data from the ARCTAS field mission where, in addition to HSRL and SSFR measurements, the spectral aerosol optical thickness was available from a sunphotometer (AATS-14). A comparison of the adjusted aerosol optical thickness from HSRL and the true aerosol optical thickness from AATS-14 was used to assess the accuracy of the new algorithm. Beyond this simple comparison, the accuracy of the retrieval was estimated by determining the uncertainty of the retrieved properties, as well as the sensitivity of the retrieved aerosol optical thickness to its initial estimate. The accuracy of this retrieval during CalNex is also evaluated by comparing retrieved single scattering albedo and asymmetry parameter to their in situ measured counterparts. Although the secondary retrieved products differ slightly from in situ measurements and from measurements of aerosol optical thickness, the relative forcing efficiency derived for CalNex compares at each wavelength to within 20% per unit of midvisible aerosol optical thickness of other field missions, with the exception of freshly emitted aerosol. This result indicates that different aerosol types can be characterized by quite similar relative forcing-efficiency spectra.

The variation between these different aerosol types can be understood more thoroughly with more measurements of airborne spectral irradiance from different field missions. Although the relative forcing efficiency removes most regionally dependent factors, the regional effect of surface albedo, among others, still influence the relative forcing efficiency. By understanding this and other effects a more thorough comparison, and possibly a better constraint on the relative forcing efficiency, can be achieved. Since relative forcing efficiency is mostly constrained within 20% per unit of midvisible aerosol optical thickness for these cases it can be used as a parameterization of the aerosol direct radiative forcing of climate with the midvisible aerosol optical thickness as the only parameter. To obtain the value of the aerosol direct radiative forcing for these cases, you can simply multiply the spectrally resolved downwelling short-wave irradiance and the aerosol optical thickness at 500 nm to the average relative forcing efficiency described in this paper. Climate models, which show disagreement of aerosol absorption [*Forster et al.*, 2007], can integrate these below layer forcings and therefore help constrain the aerosol direct radiative forcing of climate.

## 2.6 Appendix A: Acronyms

In this section we present the various acronyms, organized alphabetically, used throughout this chapter.

AATS-14 - Ames 14-channel Airborne Tracking Sunphotometer

ARCTAS - Arctic Research of the Composition of the Troposphere from Aircraft and Satellites

AERONET - Aerosol Robotic Network

CalNex - Research at the Nexus of Air Quality and Climate Change

Caltech - California institute of technology

CRDS - Cavity ringdown aerosol extinction spectrometer

HG - Henyey-Greenstein phase function approximation

HSRL - High Spectral Resolution Lidar

IPCC - Intergovernmental Panel on Climate Change

IPY - International Polar Year

NASA - National Aviation and Space Administration

NOAA - National Oceanic and Atmospheric Administration

NMASS - Nucleation Mode Aerosol Size Spectrometer

PAS - Photoacoustic Absorption Spectrometer

SSFR - Solar Spectral Flux Radiometer

UHSAS - Ultrahigh Sensitivity Aerosol Size Spectrometer

WOPC - White-Light Optical Particle Counter

## 2.7 Appendix B: Radiative Properties

Presented here are the various definitions of measured and derived radiative quantities. All quantities introduced here are wavelength dependent, unless specifically mentioned.

### 2.7.1 Spectral Irradiance

Spectral irradiance ( $F$ ) is the hemispherically integrated cosine-weighted radiative energy per unit time per unit area per wavelength. The net irradiance ( $F_{net}$ ) is defined as the difference between the downwelling ( $F^\downarrow$ ) and upwelling ( $F^\uparrow$ ) irradiance ( $F_{net} = F^\downarrow - F^\uparrow$ ). The albedo ( $\alpha$ ) is the ratio of the upwelling-to-downwelling irradiance ( $\alpha = F^\uparrow/F^\downarrow$ ). In absence of net horizontal photon transport, the difference of net irradiance at the top of the layer ( $F_{top}^{net}$ ) and at the bottom of the layer ( $F_{bot}^{net}$ ) can be used to derive the layer-absorbed irradiance. Absorptance ( $A$ ) is defined as absorbed irradiance normalized by incident irradiance  $\left( A = \frac{F_{top}^{net} - F_{bot}^{net}}{F_{top}^\downarrow} \right)$ .

### 2.7.2 Aerosol Optical Thickness

Aerosol optical thickness ( $\tau$ ) is a measure of the total mean free path of photons through a layer. Scattering ( $\beta$ ) and absorption ( $\kappa$ ) coefficients are the inverse of the distance that a photon must travel before it is either scattered or absorbed. The sum of these coefficients is the extinction coefficient ( $\sigma_{ext}$ ). Aerosol optical thickness is obtained from integrating the extinction coefficient over a column:

$$\tau = \int_0^z (\kappa + \beta) dz = \int_0^z \sigma_{ext} dz. \quad (2.2)$$

### 2.7.3 Single Scattering Albedo

Single scattering albedo ( $\varpi$ ) is the ratio of scattering and extinction coefficients:

$$\varpi = \frac{\beta}{\sigma_{ext}} = \frac{\beta}{(\kappa + \beta)}. \quad (2.3)$$

The single scattering albedo of a nonabsorptive layer would be unity. It describes the absorption properties of an aerosol layer.

#### 2.7.4 Asymmetry Parameter

The asymmetry parameter ( $g$ ) is the first moment of the scattering phase function ( $P(\theta)$ ) and describes the overall direction of photon scattering [*Hansen and Hovenier, 1974*]:

$$g = \frac{1}{2} \int_0^\pi \cos(\theta) \sin\theta d\theta. \quad (2.4)$$

This parameter can be used in the Henyey-Greenstein (HG) phase-function approximation, which adequately represents the actual phase function for a spherical particle within the N-stream radiative model code DISORT [*Bohren and Clothiaux, 2006; Wiscombe and Grams, 1976*]. The asymmetry parameter ranges from -1 for backscattering to +1 for forward scattering. At a given wavelength, the largest particles scatter light more in the forward direction, and thus have a larger asymmetry parameter than the smallest particles.

#### 2.7.5 Ångström Exponent

An Ångström exponent ( $a$ ) is often used to parameterize the wavelength dependence of optical thickness. A power law approximates the relationship between wavelength ( $\lambda$ ) and aerosol optical thickness to a reference aerosol optical thickness ( $\tau_0$ ) given at a reference wavelength ( $\lambda_0$ ):

$$\tau = \tau_0 \left( \frac{\lambda}{\lambda_0} \right)^{-a}. \quad (2.5)$$

The Ångström exponent is often used as a qualitative indicator of aerosol particle size. Values of  $a \leq 1$  indicate size distributions dominated by larger aerosols (radii  $\geq 0.5$   $\mu\text{m}$ ), which are typically associated with dust and sea salt. Values of  $a \geq 2$  indicate size distributions dominated by smaller aerosols (radii  $\leq 0.5$   $\mu\text{m}$ ), which are usually associated with urban pollution and biomass burning [*Eck et al., 1999; Westphal and Toon, 1991*]. This relationship is used in this work to extrapolate aerosol optical thickness measured at a single wavelength to aerosol optical thickness at multiple wavelengths.

## 2.8 Appendix C: Aerosol Retrieval

The aerosol retrieval method described in *Schmidt et al.* [2010], used as an intermediate step to get the relative forcing efficiency, is based on minimizing the difference between modeled and measured upwelling and downwelling spectral irradiance at the top and bottom of a layer. Figure 2.4 shows the measurement geometry. Model input parameters, i.e., single scattering albedo, asymmetry parameter, and surface albedo, are varied in a radiative transfer model until the calculated spectral irradiances match the measured values. This method requires concurrent measurements of aerosol optical thickness from a sunphotometer (e.g., AATS-14) or from HSRL and spectral irradiance (e.g., from SSFR).

The retrieval algorithm applied to the observations from CalNex required a modification to the one developed by *Schmidt et al.* [2010] because spectral aerosol optical thickness was not measured onboard the P-3. In lieu of directly measured spectral aerosol optical thickness onboard the same aircraft, the modified retrieval method uses the layer-integrated extinction from HSRL on the King air as initial estimate of optical thickness at 532 nm. This estimate is then adjusted iteratively to account for the temporal (30 min) and spatial (up to 2.5 km) mismatch between P-3 and King Air. The initial estimate at other wavelengths is extrapolated from the HSRL measurements using the AERONET optical thickness (that is, full-column) measurements at the Caltech ground site via the Ångström exponent.

By varying the initial estimate of aerosol optical thickness, the aerosol asymmetry parameter, derived with two different methods (transmittance and reflectance) described by *Schmidt et al.* [2010], can converge to a single value. Only a correct combination of aerosol optical thickness, single scattering albedo, and surface albedo will produce convergent asymmetry parameters from the two methods.

To evaluate the accuracy of the retrieved relative forcing efficiency, the uncertainty has been determined for both the relative forcing efficiency and the secondary products (aerosol optical thickness, single scattering albedo, asymmetry parameter, and surface albedo). These uncertainties

are determined by varying the inputs of the retrieval (spectral irradiance) within their uncertainty range. While the uncertainty has been determined by varying the input spectral irradiance within its uncertainty range, the uniqueness of the retrieved properties is determined by varying the initial estimate of the aerosol optical thickness within a wide range of values. This uniqueness test presents the retrieved products sensitivity to the initial estimate of aerosol optical thickness and at which initial estimate the retrieved products are no longer unique. Another evaluation of the accuracy of the retrieval is based on the comparison of in situ measurements of the asymmetry parameter and the single scattering albedo, taken during CalNex with their retrieved counterparts. An independent way to determine the accuracy of the relative forcing efficiency uses data taken during another field mission (ARCTAS) where concurrent measurements of aerosol optical thickness and spectral irradiance were in fact available. By applying this retrieval to ARCTAS, a comparison of retrieved to measured aerosol optical thickness is used to evaluate the accuracy of the retrieved relative forcing efficiency.

### 2.8.1 Retrieval Description

A conceptual map of the modified *Schmidt et al.* [2010] retrieval algorithm is shown in Figure 2.8. This algorithm is sequentially iterative, where one aerosol property is modified within each step to obtain matching modeled and measured spectral irradiance at each selected wavelength. Single scattering albedo ( $\varpi$ ) is determined by matching the absorbed spectral irradiance ( $A$ ), similar to the method described in *Bergstrom et al.* [2003]. The surface albedo ( $\alpha$ ) is derived from the reflected spectral irradiance ( $F_{bot}^\uparrow$ ). The asymmetry parameter can be obtained from layer-transmitted spectral irradiance ( $F_{bot}^\downarrow$ ) or from layer-reflected spectral irradiance ( $F_{top}^\uparrow$ ) [*Schmidt et al.*, 2010], resulting in two values for the asymmetry parameter,  $g$ , from transmittance and  $\hat{g}$ , from the reflectance. In the original algorithm [*Schmidt et al.*, 2010], the consistency of  $g$  and  $\hat{g}$  indicates whether the retrieval is successful. If  $g \neq \hat{g}$ , the retrieval is discarded. For the modified algorithm applied here, the consistency of  $g$  and  $\hat{g}$  is used as the basis for modifying the initial estimate for the optical thickness from HSRL. The aerosol optical thickness is modified by a factor

$(\Delta\tau)$  until  $g$  and  $\hat{g}$  converge within a specified limit.

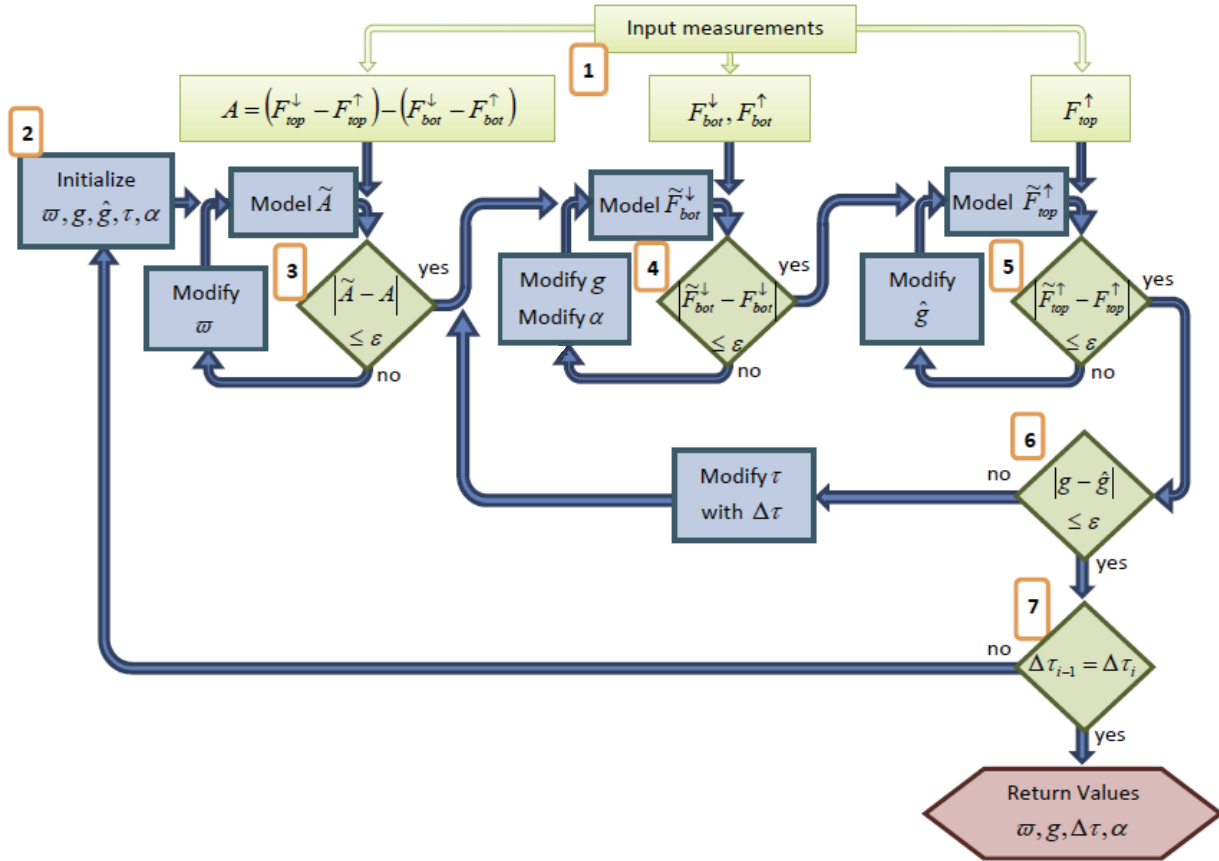


Figure 2.8: Conceptual map of the aerosol retrieval algorithm. Starting from measured spectral irradiance above and below the aerosol layer (1) and initial estimates for single scattering albedo, asymmetry parameter, surface albedo, and aerosol optical thickness (2). The steps 3, 4, and 5 compare modeled spectral irradiance to the measured values after modifying the single scattering albedo, and two values of the asymmetry parameter, respectively. If the two methods for deriving asymmetry parameter do not agree (step 6), the aerosol optical thickness is adjusted until the two methods return the same asymmetry parameter. Steps 2–6 are repeated until the aerosol optical thickness modification obtained does not vary (7) between each repetition.

The modeled top-of-layer incident irradiance spectra do not always coincide with the measurements. These in turn affect all the modeled irradiance spectra. To address this issue, we introduce a correction factor, the ratio of the modeled and measured incident spectral irradiance on top of the aerosol layer. The correction factor rescales all four spectral irradiance components. This correction factor rarely differs by more than 5% from unity. When it does, then the retrieval is discarded. A pre-defined measurement-model convergence threshold,  $\epsilon$ , is based on measurement

uncertainty and an empirical optimization of computing time. When the modeled spectral irradiances are equal to the spectral irradiance measurements (within  $\varepsilon$ ), the convergence criterion is satisfied.

The following paragraphs describe the retrieval algorithm. In the retrieval algorithm description, the subscript  $i$  denotes the current iteration value, while  $i - 1$  denotes the previous iteration value, and  $i + 1$ , the next iteration step. Modeled values are denoted by a  $\sim$ . The numbered steps correspond to the numbers in the Figure 2.8.

- (1) Input the pairs of above-layer and below-layer measured spectral irradiance.
- (2) Initialization routine sets  $\varpi$  to 0.9,  $g$  and  $\hat{g}$  to 0.6,  $\alpha$  to the ratio of  $F_{bot}^\uparrow$  and  $F_{bot}^\downarrow$ , and  $\tau$  to the initial estimate of aerosol optical thickness from HSRL and AERONET.
- (3) Step  $\varpi$ 
  - (a) Model the absorptance,  $\tilde{A}$ , defined in Sect. 2.7.1, with current values of  $\varpi$ ,  $g$ ,  $\alpha$ , and  $\tau$ .
  - (b) If  $|\tilde{A} - A| < \varepsilon$ , where  $\varepsilon = 0.001$ , proceed to step (4).
  - (c) Modify  $\varpi$  for next iteration while keeping all other variables constant using:

$$\varpi_{i+1} = \varpi_i \times \left( \frac{\tilde{A}}{A} \right)^{0.1}. \quad (2.6)$$

- (4) Step  $g$  and  $\alpha$

- (a) Model the transmitted spectral irradiance,  $F_{bot}^\downarrow$ , and below-layer upwelling spectral irradiance,  $F_{bot}^\uparrow$ .
- (b) If  $|F_{bot}^\downarrow - \tilde{F}_{bot}^\downarrow| < \varepsilon$ , where  $\varepsilon = F_{bot}^\downarrow \cdot 0.01$ , proceed to step (5).
- (c) Modify both  $g$  and  $\alpha$  for the next iteration, using

$$g_{i+1} = g_i \times \left( \frac{F_{bot}^\downarrow}{\tilde{F}_{bot}^\downarrow} \right), \quad (2.7)$$

$$\alpha_{i+1} = \alpha_i \times \left( \frac{F_{bot}^\uparrow / F_{bot}^\downarrow}{\tilde{F}_{bot}^\uparrow / \tilde{F}_{bot}^\downarrow} \right). \quad (2.8)$$

- (5) Step  $\hat{g}$ .

- (a) Model above the layer upwelling spectral irradiance,  $F_{top}^\uparrow$ .
- (b) If  $|F_{top}^\uparrow - \tilde{F}_{top}^\uparrow| < \varepsilon$ , where  $\varepsilon = 0.002$ , proceed to step (6).
- (c) Modify  $\hat{g}$  for the next iteration, using:

$$\hat{g}_{i+1} = \hat{g}_i \times \left( \frac{F_{top}^\uparrow}{\tilde{F}_{top}^\uparrow} \right). \quad (2.9)$$

- (6) Consistency of  $g$  and  $\hat{g} - \Delta\tau$  step.

- (a) If  $|g - \hat{g}| < \varepsilon$ , where  $\varepsilon = 0.02$ , proceed to step (7).
- (b) Variation of  $\tau$  by  $\pm 4\%$  of  $\tau$  ( $\Delta\tau = 0.04 \tau$ ):

$$\tau_{i+1} = \tau_i \pm \Delta\tau. \quad (2.10)$$

- (c) Return to step (4), keeping  $\varpi$  constant, using the new  $\tau$ .
- (7) Final consistency test of  $\Delta\tau$ .
- (a) The new variation of  $\Delta\tau_i$  must be equal to the last derived variation  $\Delta\tau_{i-1}$ . If  $\Delta\tau_i = \Delta\tau_{i-1}$ , then return the values of  $\varpi$ ,  $g$ ,  $\alpha$ , and  $\Delta\tau$ .
  - (b) If  $\Delta\tau_i - \Delta\tau_{i-1} \neq 0$  return to step (3) starting with the current values of  $\varpi$ ,  $g$ ,  $\hat{g}$ , and  $\alpha$ , while initializing  $\tau$  to its original value.

The exponent in step (3c) is determined from tests designed to minimize the time of convergence while still having convergence. During these test, there was no evidence that the exponent influenced the results. In step (6), agreement between the two methods of evaluating the asymmetry parameter indicated convergence of the aerosol optical thickness. If the retrieval is successful, the values of the asymmetry parameter retrieved by the two different methods match ( $g - \varepsilon < \hat{g} < g + \varepsilon$ ). If the two values do notmatch ( $g + \varepsilon < \hat{g}$  or  $g - \varepsilon > \hat{g}$ ), then the aerosol optical thickness is either increased or decreased by 4%. The 4% optical thickness modification increment was based on the uncertainty of the inputs and empirical tests aimed at minimizing computing time.

If the aerosol properties between the lower leg and the surface are unknown, the retrieved surface albedo may not be representative of the true value. However, in the sense of an effective surface albedo, it is sufficient to use it when deriving the aerosol radiative forcing of the layer, which depends on the albedo at the low flight level, regardless of the actual surface albedo. The effective surface albedo encompasses contributions from the surface and the aerosol layer of unknown properties between the bottom flight leg and the surface.

### 2.8.2 Retrieval Uncertainty

To quantify uncertainties, an approximation of the total derivative method [Bevington and Robinson, 2003] is used for deriving the error associated with this retrieval. For a function  $y(x_1, x_2, \dots, x_i)$ , the uncertainty ( $\Delta y$ ) is:

$$\Delta y = \sqrt{\left(\frac{\partial y}{\partial x_1}\right)^2 \Delta x_1^2 + \left(\frac{\partial y}{\partial x_2}\right)^2 \Delta x_2^2 + \dots + \left(\frac{\partial y}{\partial x_i}\right)^2 \Delta x_i^2}, \quad (2.11)$$

where  $\left(\frac{\partial y}{\partial x_1}, \dots, \frac{\partial y}{\partial x_i}\right)$  are partial derivatives of this function with respect to the variables  $(x_1, \dots, x_i)$ , and the uncertainties of the independent variables are  $(\Delta x_1, \dots, \Delta x_i)$ . For the aerosol retrieval, changes in the input irradiances  $(F_{top}^\downarrow, F_{top}^\uparrow, F_{bot}^\downarrow, F_{bot}^\uparrow)$  produce a change in the retrieved single scattering albedo, asymmetry parameter, and surface albedo. This numerically derived change is used to approximate partial derivatives. For example, the change in  $\varpi$  due to a change in  $F_{top}^\downarrow$ ,  $\frac{\delta \varpi}{\delta F_{top}^\downarrow}$ , is:

$$\frac{\delta \varpi}{\delta F_{top}^\downarrow} = \frac{\left(\varpi|_{F_{top}^\downarrow + \Delta F_{top}^\downarrow}\right) - \left(\varpi|_{F_{top}^\downarrow - \Delta F_{top}^\downarrow}\right)}{\left(F_{top}^\downarrow + \Delta F_{top}^\downarrow\right) - \left(F_{top}^\downarrow - \Delta F_{top}^\downarrow\right)}, \quad (2.12)$$

where  $\varpi|_{F_{top}^\downarrow + \Delta F_{top}^\downarrow}$  ( $\varpi|_{F_{top}^\downarrow - \Delta F_{top}^\downarrow}$ ) denotes the single scattering albedo that has been retrieved from the downwelling spectral irradiance measured above the layer that corresponds to  $F_{top}^\downarrow + \Delta F_{top}^\downarrow$  ( $F_{top}^\downarrow - \Delta F_{top}^\downarrow$ ). This approximation is also used for all the other input parameters. The total uncertainty in  $\varpi$ :

$$\Delta \varpi = \left[ \frac{\delta \varpi^2}{\delta F_{top}^\downarrow} \Delta F_{top}^\downarrow^2 + \frac{\delta \varpi^2}{\delta F_{top}^\uparrow} \Delta F_{top}^\uparrow^2 + \frac{\delta \varpi^2}{\delta F_{bot}^\downarrow} \Delta F_{bot}^\downarrow^2 + \frac{\delta \varpi^2}{\delta F_{bot}^\uparrow} \Delta F_{bot}^\uparrow^2 \right]^{1/2}, \quad (2.13)$$

combined with the approximations for the partial derivatives as described above is

$$\begin{aligned} \Delta \varpi = & \left[ \left( \frac{\left(\varpi|_{F_{top}^\downarrow + \Delta F_{top}^\downarrow}\right) - \left(\varpi|_{F_{top}^\downarrow - \Delta F_{top}^\downarrow}\right)}{\left(F_{top}^\downarrow + \Delta F_{top}^\downarrow\right) - \left(F_{top}^\downarrow - \Delta F_{top}^\downarrow\right)} \right)^2 \Delta F_{top}^\downarrow^2 + \left( \frac{\left(\varpi|_{F_{top}^\uparrow + \Delta F_{top}^\uparrow}\right) - \left(\varpi|_{F_{top}^\uparrow - \Delta F_{top}^\uparrow}\right)}{\left(F_{top}^\uparrow + \Delta F_{top}^\uparrow\right) - \left(F_{top}^\uparrow - \Delta F_{top}^\uparrow\right)} \right)^2 \Delta F_{top}^\uparrow^2 \right. \\ & \left. + \left( \frac{\left(\varpi|_{F_{bot}^\downarrow + \Delta F_{bot}^\downarrow}\right) - \left(\varpi|_{F_{bot}^\downarrow - \Delta F_{bot}^\downarrow}\right)}{\left(F_{bot}^\downarrow + \Delta F_{bot}^\downarrow\right) - \left(F_{bot}^\downarrow - \Delta F_{bot}^\downarrow\right)} \right)^2 \Delta F_{bot}^\downarrow^2 + \left( \frac{\left(\varpi|_{F_{bot}^\uparrow + \Delta F_{bot}^\uparrow}\right) - \left(\varpi|_{F_{bot}^\uparrow - \Delta F_{bot}^\uparrow}\right)}{\left(F_{bot}^\uparrow + \Delta F_{bot}^\uparrow\right) - \left(F_{bot}^\uparrow - \Delta F_{bot}^\uparrow\right)} \right)^2 \Delta F_{bot}^\uparrow^2 \right]^{1/2}. \end{aligned} \quad (2.14)$$

The uncertainties of the asymmetry parameter and surface albedo can be derived in the same way.

The uncertainty of the aerosol optical thickness is determined by using a case from ARCTAS [Jacob *et al.*, 2009] on 9 July 2008 where a boreal forest fire plume was sampled. During the summer component of ARCTAS, based out of Cold Lake, Alberta, Canada, measurements from SSFR

and the AATS-14 were taken, where both instruments were mounted on the NASA P-3. AATS-14 provided aerosol optical thickness measurements simultaneously with spectral irradiance measurements from SSFR. Some NASA King Air flights, with the HSRL onboard, were coordinated with the NASA P-3, as they were during the CalNex case study. The relevant radiative measurements available during CalNex and ARCTAS are presented in Table 2.2.

Table 2.2: Available spectral radiative measurements on board aircrafts during CalNex and ARCTAS field missions

Field missions	$F$	$\tau$
ARCTAS	SSFR on board NASA P-3	Airborne sunphotometer (AATS-14) on board NASA P-3 and coordinated measurements with HSRL on board NASA King Air
CalNex	SSFR on board NOAA P-3	Coordinated measurements with HSRL on board NASA King Air

Using data obtained during ARCTAS, the retrieval of aerosol optical thickness and its uncertainty was possible. The two asymmetry parameter values ( $g$  and  $\hat{g}$ ) and their absolute difference vary with a change of the assumed (and a priori unknown) optical thickness (Fig. 2.9a and 2.9b). The aerosol optical thickness which minimizes the difference between these two asymmetry parameter retrievals (within  $\epsilon$ ) represents the best estimate for the optical thickness given all irradiance measurements. In the case of the ARCTAS measurements where the true aerosol optical thickness was known from AATS-14, the irradiance-derived optical thickness is in agreement with the AATS-14 derived value. In contrast to the uncertainty estimation of the single scattering albedo and the asymmetry parameter, Eq. 2.11 - 2.13 cannot be used to determine the range of uncertainty in the aerosol optical thickness, since the relationship of  $\tau_i$  versus  $|g - \hat{g}|$  exhibits discontinuities over the range of observed aerosol optical thickness; note the jump of  $|g - \hat{g}|$  near optical thickness 0.65 in

Fig. 2.9b. These discontinuities, which arise from determining  $g$  and  $\hat{g}$  either from increasing or decreasing aerosol optical depth, represent a change in the solution set of single scattering albedo and asymmetry parameter at one aerosol optical depth. The range of aerosol optical thickness that leads to consistent values of  $g$  and  $\hat{g}$  within their uncertainties, i.e.,  $|g - \hat{g}| \leq \sqrt{\Delta g^2 + \Delta \hat{g}^2}$ , is represented by values of  $|g - \hat{g}| < \varepsilon$  (marked in red in Figure 2.9b).

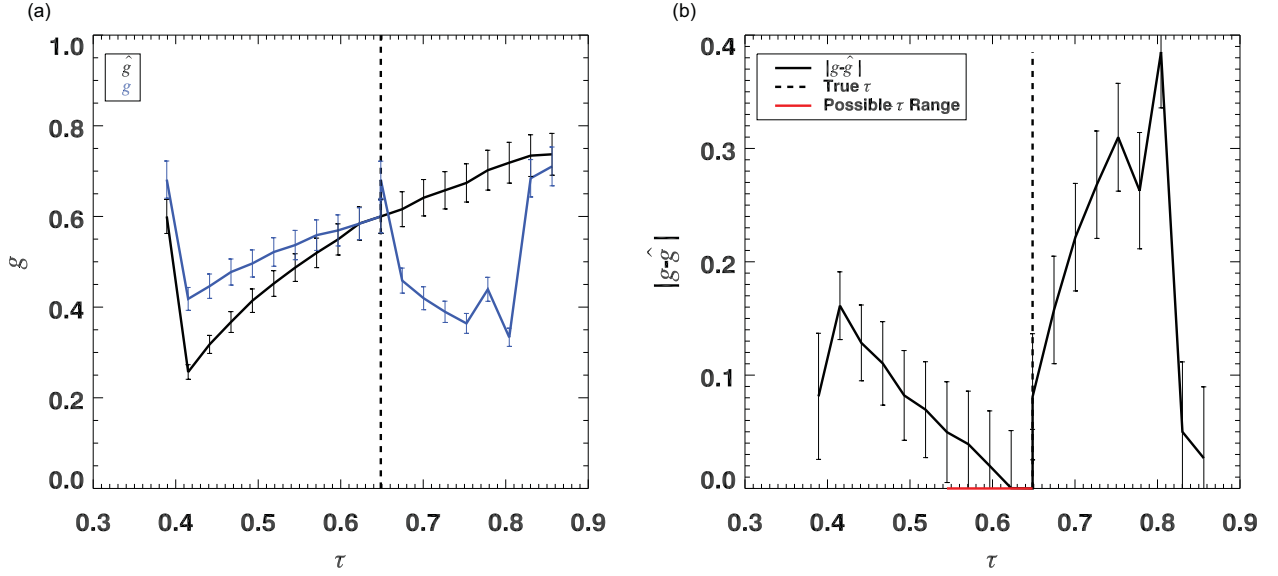


Figure 2.9: Determination of the aerosol optical thickness and its uncertainty by using: (a) Retrieved asymmetry parameter from the two different methods ( $g$  and  $\hat{g}$ ), (b) Difference between  $g$  and  $\hat{g}$  as a function of aerosol optical thickness. The red line is the range in uncertainty for the retrieved aerosol optical thickness. Here the difference between the two values of the asymmetry parameter is near zero. The error bars for  $g$  and  $\hat{g}$  have been determined from an approximation of the total derivative method (Eq. 2.11), while the dotted line represents the measured aerosol optical thickness.

The uncertainty in relative forcing efficiency  $e$  is determined by  $\tau_{500nm}$ ,  $F_{top}^\downarrow$ , forcing ( $f$ ), and their uncertainties (from Eq. 2.1 and Eq. 2.11):

$$\Delta f_e = \sqrt{\left(\frac{f}{\tau_{500nm}^2 F_{top}^\downarrow}\right)^2 \Delta \tau_{500nm}^2 + \left(\frac{f}{\tau_{500nm} F_{top}^\downarrow}\right)^2 \Delta F_{top}^{\downarrow 2} + \left(\frac{1}{\tau_{500nm} F_{top}^\downarrow}\right)^2 \Delta f^2} \quad (2.15)$$

where the uncertainty in the radiative forcing ( $\Delta f$ ) is determined by:

$$\Delta f = \left[ \left( \frac{(f|_{\varpi+\Delta\varpi}) - (f|_{\varpi-\Delta\varpi})}{(\varpi + \Delta\varpi) - (\varpi - \Delta\varpi)} \right)^2 \Delta\varpi^2 + \left( \frac{(f|_{g+\Delta g}) - (f|_{g-\Delta g})}{(g + \Delta g) - (g - \Delta g)} \right)^2 \Delta g^2 + \left( \frac{(f|_{\alpha+\Delta\alpha}) - (f|_{\alpha-\Delta\alpha})}{(\alpha + \Delta\alpha) - (\alpha - \Delta\alpha)} \right)^2 \Delta\alpha^2 + \left( \frac{(f|_{\tau+\Delta\tau}) - (f|_{\tau-\Delta\tau})}{(\tau + \Delta\tau) - (\tau - \Delta\tau)} \right)^2 \Delta\tau^2 \right]^{1/2}. \quad (2.16)$$

### 2.8.3 Retrieval Testing

One of the intermediate steps of the new relative forcing efficiency retrieval is tested by applying this retrieval to the ARCTAS case, described above, and comparing the retrieved aerosol optical thickness to the measured aerosol optical thickness. We compared the retrieved aerosol optical thickness to measurements acquired from AATS-14 (Fig. 2.10). The initial estimate of aerosol optical thickness used the 532 nm aerosol extinction profile from HSRL extrapolated to the entire spectrum with the Ångström exponent from AATS-14. Differently from CalNex, AATS-14 is used to obtain the Ångström exponent in lieu of a surface AERONET station, since there was none in the flight vicinity. At wavelengths near 532 nm, the irradiance-derived aerosol optical thickness agrees with the AATS-14 aerosol optical thickness within 15%. At the shorter and longer wavelengths (<452 nm, >675 nm respectively), the irradiance-derived aerosol optical thickness deviates from the AATS-14 derived values by an average of up to 35%. Although the disagreement is considerably larger than AATS uncertainty ( $\sim 0.013$ ) [Redemann *et al.*, 2005], the range of uncertainty in the irradiance-derived optical thickness is consistent with the AATS retrievals. Where the range of retrieved values doesn't overlap with the measurements, they are only separated by up to 0.1, which can be said to be the minimum uncertainty. Therefore, this retrieval can be used even when concurrent aerosol optical thickness measurements are unavailable, albeit with a reduced accuracy in aerosol optical thickness.

### 2.8.4 Retrieval Sensitivity and Uniqueness

The retrieval of aerosol optical thickness, single scattering albedo, asymmetry parameter, and surface albedo may not be unique, given the irradiance measurements alone. For example, while

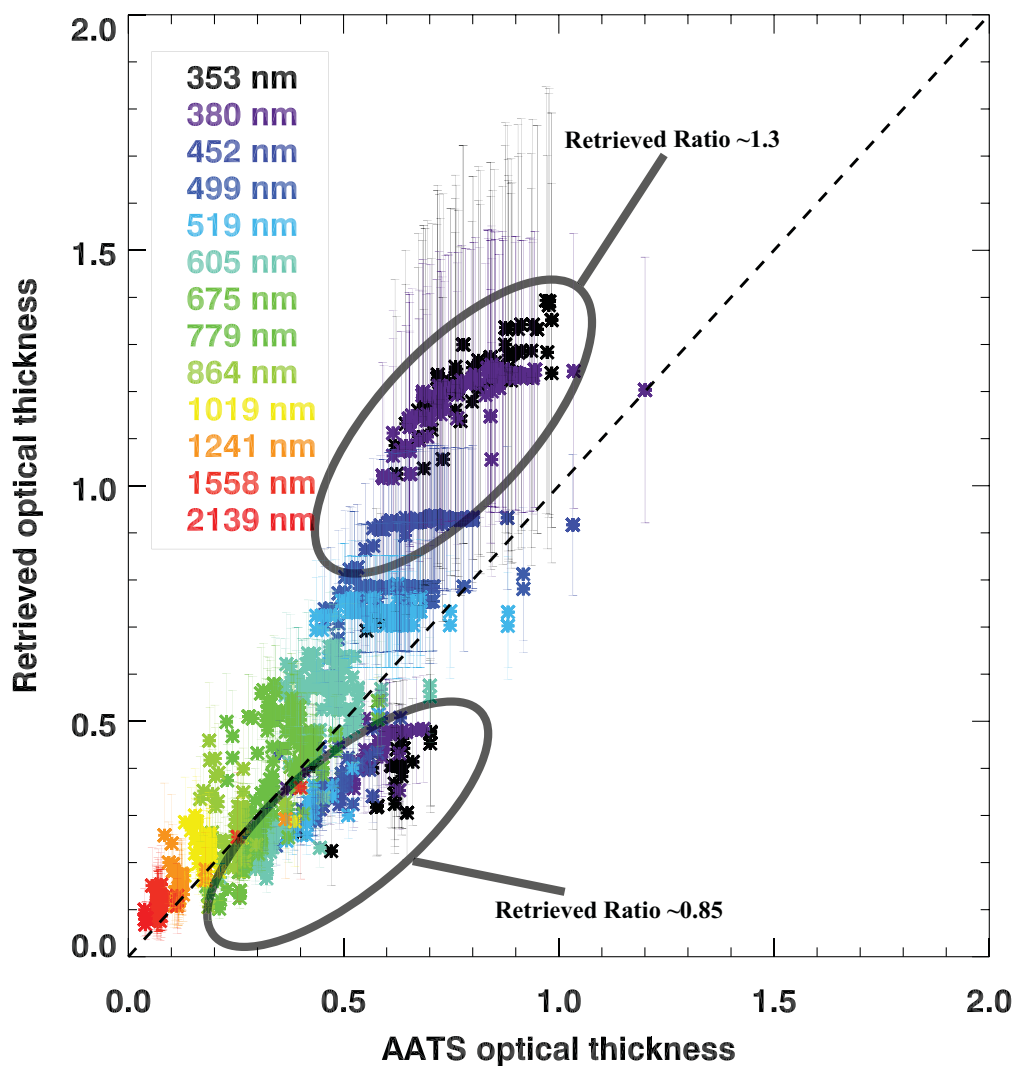


Figure 2.10: Retrieved aerosol optical thickness (y axis) compared with measured aerosol optical thickness (AATS-14; x axis) during the ARCTAS case on 9 July 2008. Wavelength is indicated by the symbol colors. The dotted line denotes a slope of one. The two circled areas represent regions where the ratio of retrieved optical thickness to AATS optical thickness are approximately 1.3 and 0.85, respectively.

Fig. 2.9b shows only one solution for optical thickness, the absolute difference between the two values for the asymmetry parameter may have multiple minima as a function of optical thickness. In this case, a-priori information, i.e., an initial estimate for the optical thickness parameter (for example, from a nearby platform) is required. To retrieve a unique solution of aerosol optical thickness, single scattering albedo, asymmetry parameter, and surface albedo, the initial estimate has to be within a factor of 0.55 to 1.30 to the true aerosol optical thickness to ensure a unique

solution.

To determine this range, we used the data gathered during the ARCTAS case where the actual value of aerosol optical thickness is known as input to retrieve relative forcing efficiency and its secondary products. The sensitivity of the retrieved aerosol optical thickness to its initial estimate indicates the maximum deviation of the initial estimate from the true aerosol optical thickness. This sensitivity is determined by considering the range of solutions for the optical thickness when varying the initial estimate for the aerosol optical thickness (e.g., 0 to 2.5 at 500 nm). If the initial estimate is either larger than a factor 1.3 or smaller than a factor 0.55 of the actual optical thickness, the solutions become multimodal. Therefore, an initial estimate within a reasonable range of the true optical thickness is essential.

### 2.8.5 Retrieval Comparisons of Secondary Aerosol Optical Properties

Tests for the secondary retrieved parameters were conducted by comparing them to their in situ measured counterparts (Fig. 2.11). In situ measurements of single scattering albedo and asymmetry parameter were not available at ambient humidity. Instead, the humidified single scattering albedo was obtained by combining measurements of dry-particle absorption from the PAS and calculations of extinction at elevated humidity, based upon measurements of dry particle extinction made by the CRDS. This approach assumed that absorption was independent of relative humidity. A combination of kappa-Köhler [*Petters and Kreidenweis, 2007*] and Mie theories [*Wiscombe, 1979*] were used to calculate the degree to which scattering was enhanced at elevated relative humidity with respect to dry conditions. This scattering enhancement is determined by evaluating the hygroscopicity parameter (the growth of a particle due to an uptake of water vapor). The hygroscopicity parameters for aerosol of ambient composition were derived by volumeweighting the hygroscopicity parameter assigned to each of the non-refractory components measured by an aerosol mass spectrometer aboard the P3 (ammonium nitrate: 0.59, ammonium sulphate: 0.53, organics 0.01) and to black carbon (0). This calculation-based approach was preferred to using direct measurements of the relative humidity enhancement made by the CRDS as it provided slightly more data during

the period of interest. Comparison of calculated and measured enhancement factors during periods of concurrent coverage showed excellent agreement. For obtaining the asymmetry parameter, Mie scattering calculations were based on the ambient relative humidity aerosol particle size distribution, which was calculated from the measured dry particle size distributions using kappa-Köhler theory as described above. These Mie scattering calculations represent spherical aerosol particles at a constant refractive index. Variations in both the aerosol particles geometrical shape and refractive index can add more variability to the resulting asymmetry parameter.

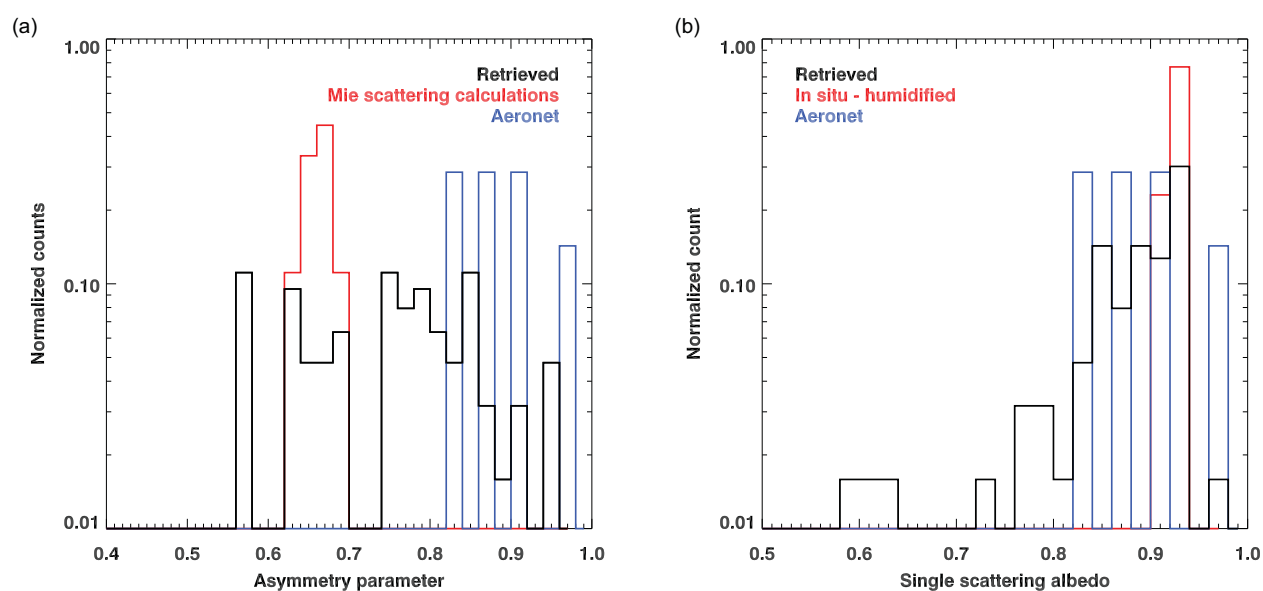


Figure 2.11: Distributions of retrieved and in situ-measured aerosol properties at 532 nm. (a) The derived asymmetry parameter determined by Mie-scattering calculations. These calculations use inputs of aerosol particle-size distribution from the White-Light Optical Particle Counter (WOPC), Ultrahigh Sensitivity Aerosol Size Spectrometer (UHSAS), and Nucleation Mode Aerosol Size Spectrometer (NMASS). (b) Comparison of single scattering albedo as measured by the Cavity Ring Down (CRDS) and Photoacoustic Absorption Spectrometer (PAS) instruments to its retrieved values. These values are also compared to the values determined by AERONET which were measured  $\sim 5$  h later.

The frequency distribution of the retrieved asymmetry parameter and single scattering albedo is compared to the distribution of their in situ and AERONET retrieved counterparts (Fig. 2.11). The retrieved asymmetry parameter distribution (Fig. 2.11a) derived from SSFR measurements seems to overlap with both the distributions from AERONET and in situ based Mie scattering

calculations, even though these two distributions do not mutually overlap, albeit the AERONET distribution of asymmetry parameter only contains 7 points. Similarly to previous studies [*Esteve et al.*, 2012], the asymmetry parameter values derived from AERONET measurements are higher than those derived from in situ measurements. Although the distributions overlap, there are large differences between the distributions of these aerosol properties. Differences between aerosol properties derived from radiative measurements and in situ measurements may be due to a difference in the sampling volume. The aerosol properties derived from SSFR measurements represent the column-integrated values between the two flight legs, equivalent to about  $100\,000\,000\text{ m}^3/\text{s}$ , while the aerosol properties derived from the in situ measurements represent point-like measurements along the flight path, equivalent to about  $0.0005\text{ m}^3/\text{s}$ . In this view, the calculated single scattering albedo and asymmetry parameter, along with their uncertainty (not shown here) represent an effective aerosol property of the whole layer rather than a few aerosol particles. Although this can account for some of the differences, there may be also errors in the aerosol particles humidification process, described above, which may also contribute to the differences. This humidification process and the Mie scattering calculations therein use some approximations that may not always hold, such as constant refractive indices and spherical aerosol particles.

## 2.9 Acknowledgements

This work was supported through NOAA CalNex (grant NA06OAR4310085) and NASA ARCTAS (grant NNX08AF93G). The authors would like to recognize the efforts from Warren Gore and Antony Trias from NASA Ames for their continued and reliable support of the SSFR during these deployments. We thank the NASA Langley B200 King Air and NOAA WP-3D flight crews for their outstanding work in support of these measurements. Support for the HSRL measurements came from the NASA HQ Science Mission Directorate Radiation Sciences Program, the NASA CALIPSO project, and the Department of Energys Atmospheric Science Program Atmospheric System Research, an Office of Science, Office of Biological and Environmental Research program, under grant DE-AI02-05ER63985.

## Chapter 3

### **A generalized method for discriminating thermodynamic phase and retrieving cloud optical thickness and effective radius using transmitted shortwave radiance spectra**

A new retrieval scheme for cloud optical thickness, effective radius, and thermodynamic phase was developed for ground-based measurements of cloud shortwave spectral transmittance. 15 parameters were derived to quantify variations in shortwave transmittance by their sensitivity to absorption and scattering of liquid water and ice clouds, manifested by slope, curvature, and shifts in spectral features. To retrieve cloud optical thickness and effective particle radius a weighted least square fit that matched the modeled parameters was applied. The measurements for this analysis were made with a ground-based Solar Spectral Flux Radiometer (SSFR) in Boulder, Colorado, between May 2012 and January 2013. We compared the cloud optical thickness and effective radius from the new retrieval to two other retrieval methods. By using multiple spectral features, we find a closer fit (with a root mean square difference of 3.1% for a liquid water cloud and 5.9% for an ice cloud) between measured and modeled spectra compared to two other retrieval methods, which diverge by a root-mean-square of up to 6.4% for a liquid water cloud and 22.5% for an ice cloud. The new retrieval introduced here has an average uncertainty in effective radius ( $\pm 1.2\mu m$ ) smaller by factor of at least 2.5 than two other methods when applied to an ice cloud.

### 3.1 Introduction

Clouds strongly influence Earth’s radiative energy balance by modulating the transfer of shortwave radiation through the atmosphere. Clouds reduce the globally averaged solar radiation absorbed at the surface by  $53 \text{ Wm}^{-2}$  and produce a net cooling of  $21 \text{ Wm}^{-2}$  [Allan, 2011]. Cloud radiative effects are governed by optical thickness ( $\tau$ ), cloud particle effective radius ( $r_e$ ) and thermodynamic phase ( $\phi$ ) [see, for example, Key and Intrieri, 2000; Sun and Shine, 1995; Wiscombe et al., 1984]. Droplet size and water phase influences single-scattering and absorption, primarily in the near-infrared region [Slingo, 1990; Twomey and Bohren, 1980; Wiscombe et al., 1984]. For example, a liquid water droplet scatters more strongly in the forward direction than an ice particle of equivalent size [e.g., Baum et al., 2011]. Furthermore, differences in bulk liquid water and ice absorption in the near infrared (between 700–2500 nm) have observable consequences in cloud spectral reflectance and transmittance that can be exploited to retrieve cloud thermodynamic phase [e.g., Pilewskie and Twomey, 1987].

In the shortwave spectral region, optical thickness, particle size, and thermodynamic phase are most often retrieved using reflectance measurements [e.g., Nakajima and King, 1990; Platnick et al., 2001; Twomey and Cocks, 1989]. Radiation reflected at cloud top has been scattered by particles in the uppermost regions of clouds, unlike transmitted radiation which has interacted with particles throughout the entire cloud layer. For this reason, transmittance based retrievals are more representative of layer-average properties [Platnick, 2000] than their reflectance-based counterparts.

Uncertainties in retrieved cloud optical thickness and effective radius from transmittance are often much larger than from reflectance, particularly for thin clouds [Turner et al., 2007]. Large uncertainties arise in transmittance retrievals because the information content from inverse methods optimized for reflectance is reduced when applied to cloud transmittance, particularly for particle size. This demands new methods of extracting information based on the unique physics of cloud transmittance, which is revealed in the observed spectral signatures. Another problem

with transmittance-based retrievals is that optical thickness is not uniquely defined for all given transmittance, requiring additional information to retrieve optical thickness.

These problems have motivated the development of novel retrieval approaches specific to cloud transmittance. Such approaches include: the transmittance at two wavelengths for a cloud overlying a vegetated surface [*Chiu et al.*, 2010; *Marshak et al.*, 2004], the transmittance at two wavelengths where condensed water absorption varies [*Kikuchi et al.*, 2006; *Rawlins and Foot*, 1990], differential optical absorption spectroscopy (DOAS) [*Daniel*, 2002; *Daniel et al.*, 2003, 2006; *Schofield et al.*, 2007], and the slope of transmittance in selected spectral bands [*McBride et al.*, 2012, 2011]. Each of these methods has limitations. For example, using transmittance at wavelengths of differing condensed water absorption [*Kikuchi et al.*, 2006; *Rawlins and Foot*, 1990] results in non-unique solutions of  $\tau$  and  $r_e$  at optical thicknesses below 10 and large uncertainties in  $r_e$  at larger optical thicknesses. DOAS requires either assumptions or measurements of the photon path length to retrieve  $\tau$ ,  $r_e$ , and  $\phi$ . The method described by *McBride et al.* [2011] has higher sensitivity to effective radius than others, yet it is susceptible to systematic biases in absolute radiometric calibration and surface albedo [*Coddington et al.*, 2013] and has thus far been applied to liquid clouds only.

The current work introduces 15 parameters that quantify several spectral features of normalized cloud-transmitted radiance that are sensitive to  $\tau$ ,  $r_e$ , and  $\phi$ . This work is motivated by *McBride et al.* [2011] who derived one parameter, the spectral slope of transmittance between 1565–1637 nm to retrieved liquid cloud  $\tau$  and  $r_e$ . In this work, a general method is derived that incorporates characteristics of the transmittance spectra that have not been previously exploited in a retrieval scheme. Furthermore, the sensitivity to calibration biases is reduced by utilizing normalized radiance. To find the most likely combination of  $\tau$ ,  $r_e$ , and  $\phi$ , we implement a two-step least squares fit of measured parameters to modeled parameters. Thermodynamic phase is retrieved first, followed by  $\tau$  and  $r_e$ . A quantitative analysis of the retrieval scheme using the GEneralized Nonlinear Retrieval Analysis [GENRA, *Vukicevic et al.*, 2010] is presented in the next chapter.

Section 3.2 details the instrumentation and measurements used in this paper. Case studies are presented in Sect. 3.3, followed by the radiative transfer model, the variance in radiance spectra

due to changes in optical thickness, effective radius, and thermodynamic phase, and the 15 spectral parameters in Sect. 3.4. In Sect. 3.5, we introduce the retrieval and analysis methods, and apply the retrieval to measured radiance spectra and compare the results to other retrieval methods. Section 3.6 summarizes this work and presents its important conclusions.

## 3.2 Instrumentation and Measurements

Measurements of the spectral signatures of shortwave cloud transmittance were taken with the Solar Spectral Flux Radiometer [*McBride et al.*, 2011; *Pilewskie et al.*, 2003]. The SSFR is typically used to measure upwelling and downwelling spectral irradiance onboard airborne research platforms [e.g., *Kindel et al.*, 2010; *LeBlanc et al.*, 2012]. In this study, the SSFR was deployed with a suite of instruments on a rooftop observatory (Skywatch, <http://skywatch.colorado.edu/>) located above the Duane Physical Laboratory at the University of Colorado, Boulder (see Sect. 3.2.2).

### 3.2.1 Solar Spectral Flux Radiometer

The ground-based SSFR used in this study has a spectral resolution of 8 – 12 nm and covers the wavelength range between 350 – 1700 nm [*McBride et al.*, 2011]. SSFR has two light collectors: one for measuring spectral downwelling irradiance and the other, spectral zenith radiance. The radiance light collector is composed of a collimating lens with a set of baffles to restrict stray light from outside the narrow field-of-view of 2.8°. Stray light rejection was determined by rotating the light collector with respect to a collimated stable light source at 50 cm. Stray light rejection was  $10^{-5}$ , below the noise floor of the SSFR [0.1% – 0.2%, *Pilewskie et al.*, 2003]. The radiance calibration was performed with a NIST-traceable lamp illuminating a flat Spectralon panel of known reflectance. The flat panel was viewed with the radiance light collector at 45° from normal to the panel.

The accuracy of SSFR, determined using a NIST-traceable lamp, is 3-5% over the spectral range of SSFR [e.g., *LeBlanc et al.*, 2014, , Chap. 2]. The SSFR was calibrated three times over the course of the multi-month measurement period. A change of 8% was observed in successive absolute

radiometric calibrations. Because of the large time gap between calibrations, rather than correct the data using updated calibrations which would have additional uncertainties due to interpolation error, we estimated absolute accuracy to be 8%, the conservative upper limit based upon the spread in calibration curves. The spectrum-to-spectrum average variation, or precision, was much better, at  $0.01 \text{ Wm}^{-2}\text{nm}^{-1}\text{sr}^{-1}$  (0.2%) for a midvisible wavelength (near 500 nm), determined by the standard deviation a measurements from a stable light source.

When a radiance spectrum is normalized by its maximum value (found to always lie between 451 nm to 490 nm) or by its value at 1000 nm, accuracy depends on wavelength-to-wavelength stability of the sensor. This stability is evaluated by the relative change of each wavelength in the 3 radiometric calibrations. The mean variation between radiance evaluated at each wavelength and the maximum radiance was 4.6 % (or 1.1% for normalizing by the radiance at 1000 nm). This represents less variation throughout the measurement period than the absolute radiometric accuracy. Finally, the instrument was spectrally calibrated by measuring the output from a HeNe laser, Hg lamp, and a Near-IR laser diode.

### 3.2.2 Skywatch Observatory

The Skywatch Observatory (<http://skywatch.colorado.edu/>) hosts a number of instruments for measuring atmospheric radiation and precipitation. The instruments that provided data for this study were: pyranometer, pyrgeometer, ceilometer, micro rain radar (MRR), sky webcam, and a spectral sunphotometer. The pyranometer and pyrgeometer measured broad band downwelling irradiance in the wavelength ranges of 300 to 2800 nm and 4500 to 42000 nm respectively. The MRR is a K-band (24 GHz) vertical profiler of hydrometeors. These calibrated instruments provided ancillary measurements for estimating the cloud thermodynamic phase and evaluating the cloud homogeneity during SSFR measurement periods.

### 3.2.3 Satellite measurements

Coincident cloud observations were made with the Geostationary Operational Environmental Satellite [GOES, *Minnis et al.*, 1995] and the Moderate Resolution Imaging Spectroradiometer [MODIS, *Platnick et al.*, 2003]. For selected cases studied in this work, cloud top height from GOES was available for the days 2012-05-25 and 2012-08-06. MODIS derived cloud top height, cloud optical thickness, and effective radius were available on 2013-01-10. We used the MODIS 16-day averages of surface albedo [*Schaaf et al.*, 2002] for determining the surface albedo used in the radiative transfer modeling.

## 3.3 Case studies

The SSFR was deployed at Skywatch from May 2012 to February 2013. From the collected dataset, 3 cases were selected for further study based on criteria of i) cloud horizontal homogeneity and ii) variations in thermodynamic phase: liquid cloud (2012-05-25), mixed phase cloud (2012-08-06), and ice cloud (2013-01-10). In this section, we describe the ancillary data used to identify the case studies.

Cloud horizontal homogeneity is required for validity of the plane-parallel assumption in the forward-model. We determined horizontal homogeneity by small temporal variability in cloud base height (measured from the ceilometer) and broadband downwelling irradiance (measured with the pyranometer for shortwave and pyrgeometer for longwave). Visual inspection of time lapse movies, captured with a sky webcam over the selected time periods, was also used to filter for heterogeneous cloud cases. An example of data taken under heterogeneous and homogeneous cloud scenes is shown in Fig. 3.1. In this example, the heterogeneous case has variability in shortwave irradiance of more than  $800 \text{ Wm}^{-2}$  over 10 minutes,  $40 \text{ Wm}^{-2}$  in longwave irradiance over 20 minutes, and cloud base heights varying from 0 (clear sky) to 6 km. By contrast, the homogeneous cloud case has little variability in short- (less than  $200 \text{ Wm}^{-2}$  over a 4 hour period) and long-wave irradiance (less than  $20 \text{ Wm}^{-2}$  over a 4 hour period), and cloud base heights near 2 km, varying by less than 1 km.

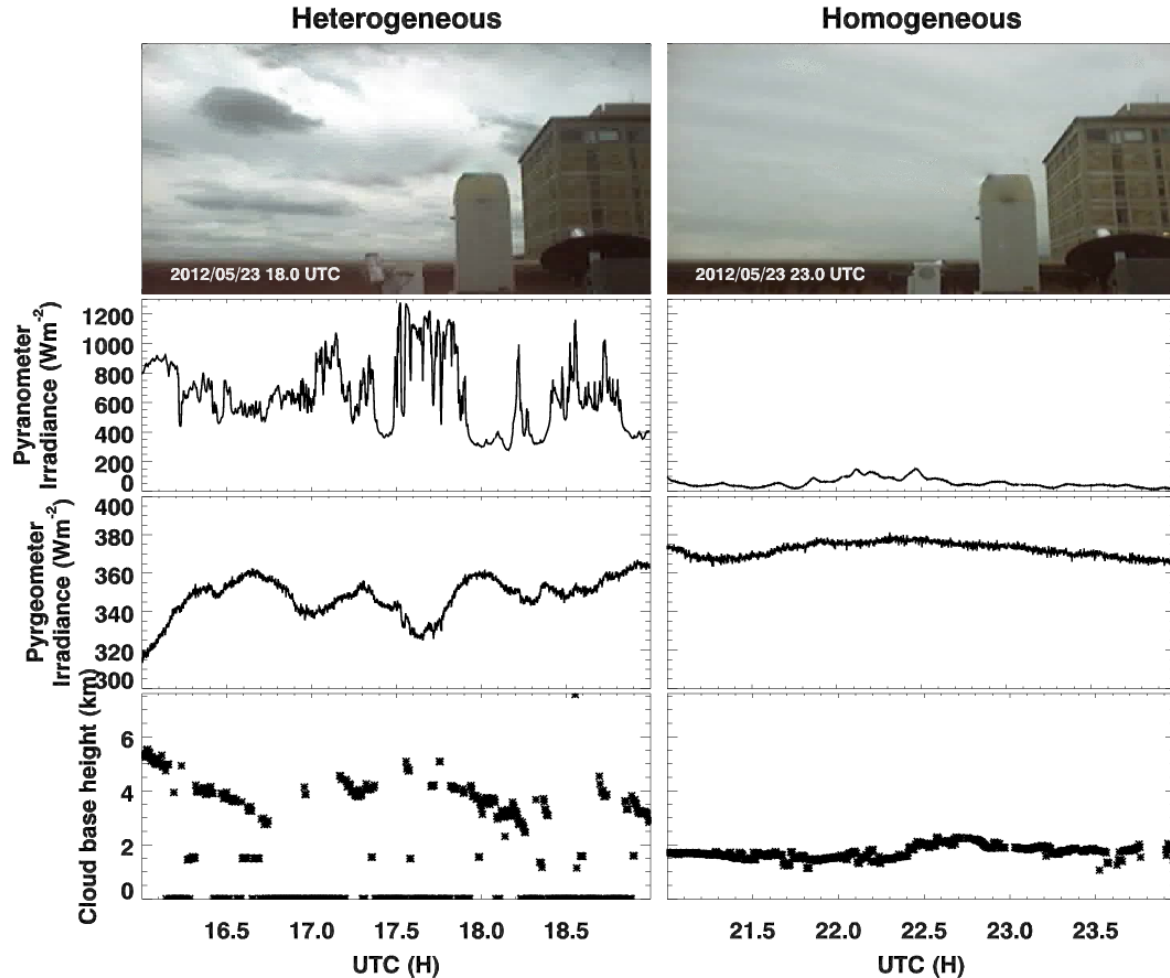


Figure 3.1: Broadband short- (pyranometer) and long-wave (pyrgeometer) irradiance and cloud base heights (ceilometer) for horizontally heterogeneous (left panel) and homogeneous (right panel) clouds taken on 23 May 2012. The top panel presents one image from the sky web cam for either heterogeneous or homogeneous clouds taken from the Skywatch observatory.

The cloud thermodynamic phase was estimated using MRR, the ceilometer, atmospheric soundings, GOES, MODIS, and SSFR measurements of spectral radiance. The atmospheric soundings for the 3 different time periods are presented in Fig. 3.2. Cloud base height is retrieved using the ceilometer located at the Skywatch facility for the time of interest. The cloud top height was obtained from GOES for 2012-05-25 and 2012-08-06, and from MODIS for 2013-01-10. The GOES cloud top height for 2012-05-25 was below the freezing level obtained from the atmospheric sounding. Therefore, we assume that the cloud on 2012-05-25 was composed entirely of liquid

water. The mixed phase case, 2012-08-06, and the ice case, 2013-01-10, had cloud base heights above the freezing level. On 2012-08-06, MRR measurements of backscatter indicated the presence of a melting layer that was also present 1 hour prior to the selected case study period. In addition, GOES-retrieved cloud thermodynamic phase, at cloud top, was ice 15 minutes prior to the measurement period, and liquid during the measurement period. Therefore, we assume that the cloud on 2012-08-06 was likely mixed-phase, for this context meaning that both ice and liquid cloud particles influenced the transmitted radiation. On 2013-01-10 cloud base height was higher than 9.4 km above sea level (ASL), higher than the upper limit of the ceilometer measurement. During the measurement period on 2013-01-10, MODIS cloud phase was determined to be ice. SSFR measurements of zenith transmittance showed a sharp decrease in spectral radiance near 1000 nm and 1200 nm (not shown), representative of ice absorption features [*Pilewskie and Twomey, 1987*]. Therefore, we assume that the cloud on 2013-01-10 was an ice cloud.

### 3.4 Radiative Transfer Simulations and Description of Retrieval Parameters

#### 3.4.1 Radiative transfer model

The radiative transfer model used in this study is the N-stream DISORT 2.0 [*Stamnes et al., 2000*] with SBDART [*Ricchiazzi et al., 1998*] for atmospheric molecular absorption; both are publicly available within LibRadtran [*Mayer and Kylling, 2005*]. We varied optical thickness from 1 to 100 in increments of 1 to 10, thermodynamic phase, and effective radius from 2.5  $\mu\text{m}$  to 30  $\mu\text{m}$  in 2.5  $\mu\text{m}$  increments for liquid drops and from 10  $\mu\text{m}$  to 60  $\mu\text{m}$  in 2.5  $\mu\text{m}$  increments for ice particles. For liquid water clouds, Mie scattering calculations were used to obtain the scattering phase function and single scattering albedo of the cloud droplets [*Evans, 1998; Wiscombe, 1980*]. A Gamma distribution with  $\alpha = 7$ , typical for liquid clouds [*Mayer and Kylling, 2005*], was used to represent the size distribution of the cloud droplets for each value of effective radius. For ice crystals, we used the scattering models for severely roughened general habit mixture described by *Baum et al.* [2011]. The scattering phase function was represented by a set of 256 Legendre coefficients

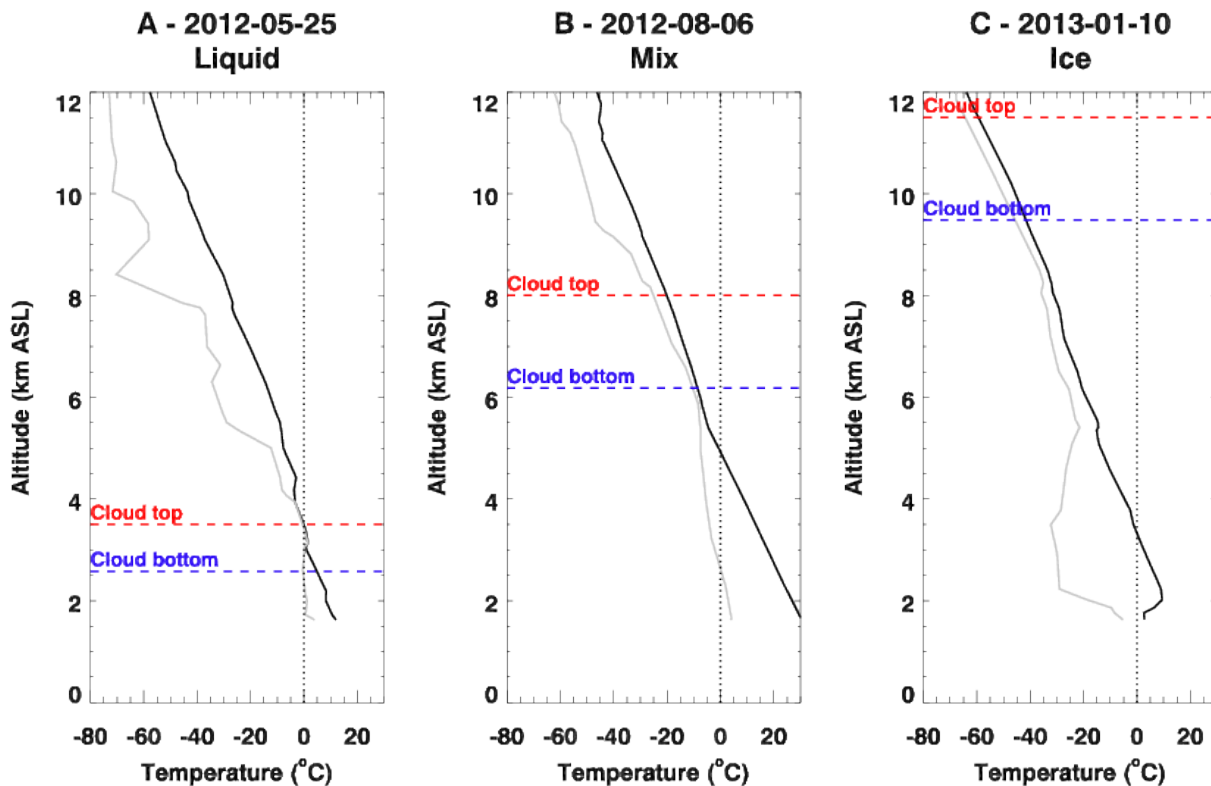


Figure 3.2: Atmospheric sounding profiles of temperature (black) and dew point (grey) taken near Denver International Airport for the case study time periods: (A) liquid cloud case on 25 May 2012, (B) mixed-phase cloud case on 6 August 2012, and (C) ice cloud case on 10 January 2013. Cloud bottom and top values determined from ground-based and satellite data (see text).

calculated using the method by *Hu et al.* [2000]. We used 28 streams in DISORT 2.0 to model the spectral zenith radiance. The use of more Legendre coefficients than streams is accomplished by the truncation approximation developed by *Nakajima and Tanaka* [1988], which is incorporated in DISORT 2.0. The extraterrestrial solar spectral irradiance was taken from *Kurucz* [1994] at 1 nm spectral resolution and convolved to the slit function and spectral resolution of the SSFR.

### 3.4.2 Ancillary inputs

Spectral radiance transmitted through clouds was modeled using a set of ancillary inputs given by a prescribed spectral surface albedo, cloud base altitude, cloud extent, and atmospheric state. The atmospheric state is defined by the profiles of number concentration of atmospheric gases,

pressure, temperature, and water vapor calculated from soundings taken at the Denver airport for each day of interest (see Fig. 3.2). Even though  $\tau$ ,  $r_e$ , and  $\phi$  control most of the variance in radiance, these sets of ancillary inputs impact the spectral radiance through multiple reflections of the below-cloud radiation.

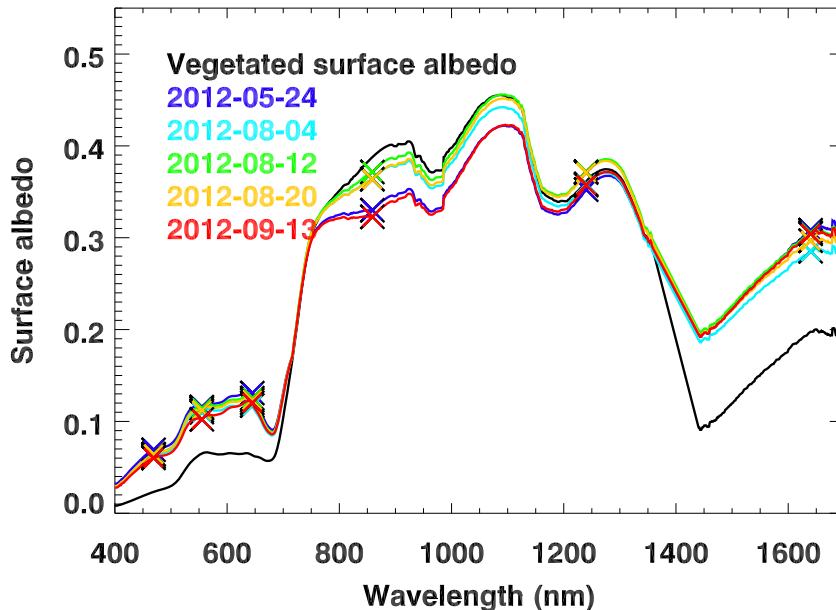


Figure 3.3: Spectral surface albedo used as input for the radiative transfer modeling for spring/summer. To approximate a full spectrum for varying days, the vegetated spectral surface albedo (black line) measured by *Michalsky et al.* [2003] is scaled using the discrete-band surface albedo product retrieved from Moderate Resolution Imaging Spectroradiometer (MODIS) measurements [*Schaaf et al.*, 2002] at the wavelengths denoted by X. This scaling is interpolated between the discrete MODIS bands.

The accuracy and precision of the retrieved cloud properties depend on an accurate knowledge of the surface albedo and atmospheric state for each measurement period. By choosing conditions that occurred for each day during the measurement, we seek to reduce this source of error. Of the 3 days selected for case study, 2 days were in the spring/summer period (2012-05-25, 2012-08-06) when surface albedo was dominated by vegetation. The remaining day (2013-01-10) was in winter with a fresh snow albedo.

Surface albedos for the spring/summer measurement period were determined by scaling a

measured, spectral albedo of a vegetated surface [Michalsky *et al.*, 2003] (Fig. 3.3). This scaling matched the 16-day average surface albedo from MODIS for Boulder, Colorado, at the discrete spectral bands 470 nm, 555 nm, 645 nm, 858 nm, 1240 nm, 1640 nm, and 2130 nm. We linearly interpolated between these bands and linearly extrapolated to shorter wavelengths to span the observed spectral range of SSFR. We applied this scaling to obtain the 16 day average surface albedo centered on 24 May 2012, on 4, 12, 20 August 2012, and on 13 September 2012 which spans our spring/summer measurement period (Fig. 3.3). We determined winter surface albedo (not shown) in a similar manner using a reference fresh snow surface albedo [Wiscombe and Warren, 1980] and scaling it to the retrieved albedo from MODIS for 10 January, 2013 in the manner described above. The cloud base height was determined with the Skywatch ceilometer measurements and cloud top height from GOES and MODIS.

### 3.4.3 Modeled Look-Up-Tables (LUT)

A set of modeled radiance spectra for varying  $\tau$ ,  $r_e$ , and  $\phi$  (presented above) is used to build a grid of spectral parameters (described in Sect. 3.4.5) commonly referred to as look-up-tables (LUT). The modeled radiance spectra were interpolated to a finer grid in  $\tau$  (resolution of 1) and  $r_e$  (resolution of  $1 \mu\text{m}$ ). For each of these interpolated radiance spectra, we calculate the 15 parameters. This LUT of parameters is calculated for multiple solar zenith angles with resolution 0.05 in cosine of the solar zenith angle, ranging from 0.6 to 0.75 for case A, 0.6-0.7 for case B, and 0.4-0.45 for case C.

### 3.4.4 Variability in normalized radiance spectra due to $\tau$ , $r_e$ , and $\phi$ physical basis

The spectral features in cloud transmittance that vary with bulk liquid and ice absorption (Fig. 3.4a) and asymmetry parameter spectrum (Fig. 3.4b) were chosen as the basis for deriving the 15 parameters. The ice absorption spectrum has local maxima that are shifted to longer wavelengths than in liquid water absorption, itself shifted to longer wavelengths than the absorption maxima in water vapor (Fig. 3.4a). Cloud-transmitted radiation at absorption maxima (for gas, liquid, and ice)

is reduced more than the radiation at the surrounding wavelengths. For cloud particle absorption, this is also dependent on particle size. Further reduction occurs due to multiple scattering within cloud, the amount of which depends upon cloud optical thickness. Asymmetry parameter is a measure of forward- to back-scattering. The asymmetry parameter for ice crystals is generally lower than for liquid droplets of equivalent effective radius (see Fig. 3.4b), meaning that radiance transmitted through an ice cloud is consistently lower than radiance transmitted through a liquid cloud with the same optical thickness.

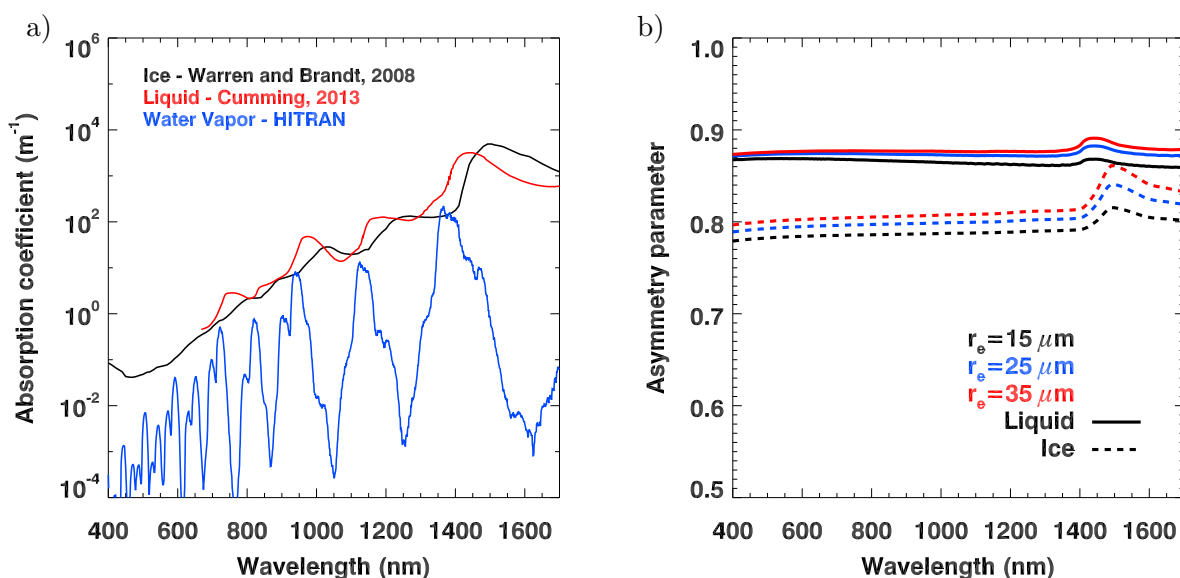


Figure 3.4: (a) Spectral bulk absorption coefficient and (b) asymmetry parameter for different thermodynamic phases of water. Notice the local maxima offset between ice water, liquid water, and water vapor near 900 nm, 1100 nm, and 1400 nm. The bulk ice absorption coefficient has been determined by *Warren and Brandt* [2008], while the bulk liquid water absorption coefficient has been determined by *Cumming* [2013]. The bulk water vapor absorption has been calculated using the HITRAN model described by *Rothman et al.* [2009] for an optical path length of 10 m with pure water vapor pressure of 15 hPa at 293 K [*Ptashnik et al.*, 2004]. The asymmetry parameter for liquid drops were calculated from Mie scattering calculation following the methodology developed by *Wiscombe* [1980]. Ice asymmetry parameter were obtained from the scattering models for severely roughened general habit mixture described by *Baum et al.* [2011].

By modulating scattering and absorption properties of cloud particles, combinations of  $\tau$ ,  $r_e$ , and  $\phi$  result in unique cloud-transmitted radiance spectra (Fig. 3.4). In general, the largest

variability throughout the entire wavelength range, outside of the gas absorption bands, is controlled by changes in  $\tau$ . By normalizing each radiance spectra by its maximum, the broad range in magnitude due to  $\tau$  (considered to be the first-order dependence on  $\tau$ ) evident in Fig. 3.5a is virtually eliminated in Fig. 3.5b. The broad range in magnitude in the near-infrared (NIR, wavelengths longer than 700 nm) due to  $\tau$  is also eliminated when normalizing each radiance spectrum by its value at 1000 nm. An added benefit of using normalized radiance is the reduction in uncertainty from 8% for radiance to 4.6% for its maximum-normalized counterpart. In addition, the change in magnitude of radiance spectra in the NIR due to variation in solar zenith angles up to  $80^\circ$  is nearly eliminated by normalizing the radiance spectra (not shown).

After normalization, the first-order dependence of the radiance spectra on  $\tau$  is removed, but variability in spectral radiance linked to spectral features that differ for  $r_e$ ,  $\phi$ , and  $\tau$  remains. By normalizing the radiance spectra, spectral features and shapes are amplified while the large scale variation in magnitude of the radiance spectra is eliminated (see Fig. 3.5). In some cases, the remaining spectral features, particularly in the NIR, become more distinct for normalized radiance spectra than non-normalized radiance spectra. One such case occurs for an ice cloud of  $\tau = 10$  (dashed red line), which coincides in the NIR with a liquid cloud of  $\tau = 50$  (solid blue line) (Fig. 3.5a). However, once normalized, these two clouds can be distinguished by their NIR spectral features (Fig. 3.5b): location of the local maximum is at 1050 nm for the liquid cloud (solid blue line) and at 1000 nm for the ice clouds (dashed red line); lower magnitude in normalized radiance near 1200 nm for the liquid than ice cloud; and steeper spectral slope near 1600 nm for the liquid than ice cloud.

Not all  $\tau$  dependence is eliminated by normalization, especially at wavelengths near the liquid and ice absorption maxima in the NIR (see Fig. 3.4a). The effects of absorption in the NIR are amplified with increases in  $\tau$ , illustrated by the large variability of normalized radiance in the NIR in Fig. 3.6. For clouds with  $\tau > 4$ , the radiance in the NIR decreases with increasing  $\tau$  and asymptotes to zero. The amount by which the NIR radiance is decreased is due to the absorption by cloud particles.

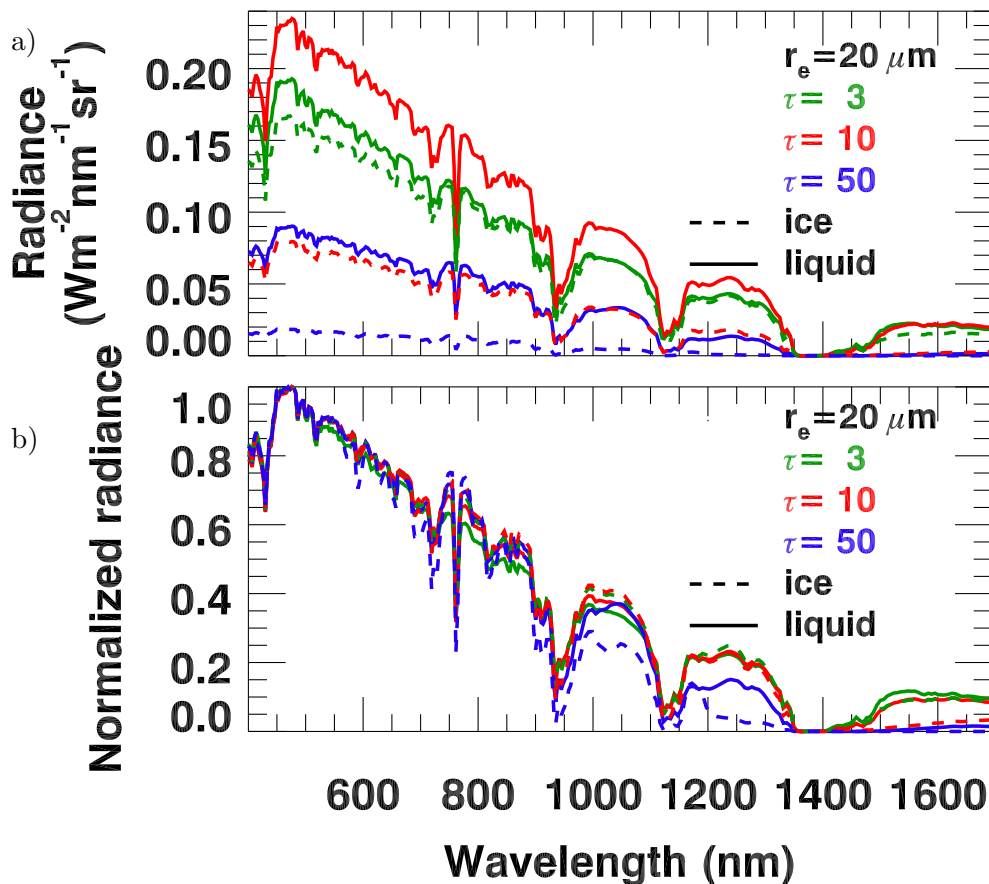


Figure 3.5: Modeled zenith radiance spectra transmitted through clouds with a few combinations of optical thickness ( $\tau$ ) for ice and liquid water clouds with an effective radius ( $r_e$ ) of  $20 \mu\text{m}$  for the atmospheric state and surface albedo defined for 2012-05-25 and a solar zenith angle of  $50^\circ$ . Top panel (a) shows the radiance spectra in  $\text{Wm}^{-2}\text{nm}^{-1}\text{sr}^{-1}$  units and bottom panel (b) shows the radiance spectra normalized by their maximum value (unitless). The radiance minima centered at 760 nm, 940 nm, 1130 nm, and 1400 nm represent gas absorption bands that are ignored in this work.

Not only does an increase in  $\tau$  reduce the NIR transmitted signal (hereafter, transmittance), differences in spectrally dependent absorption also result in features that become more distinct with increases in  $\tau$  (Fig. 3.6). Transmittance is defined here by normalization by maximum signal rather than top-of-cloud spectral radiance; note that for our purposes, the features characterizing the transmitted spectra would not change for either definition of transmittance, but may differ in magnitude. As examples of spectral features linked to differences in liquid and ice absorption, we

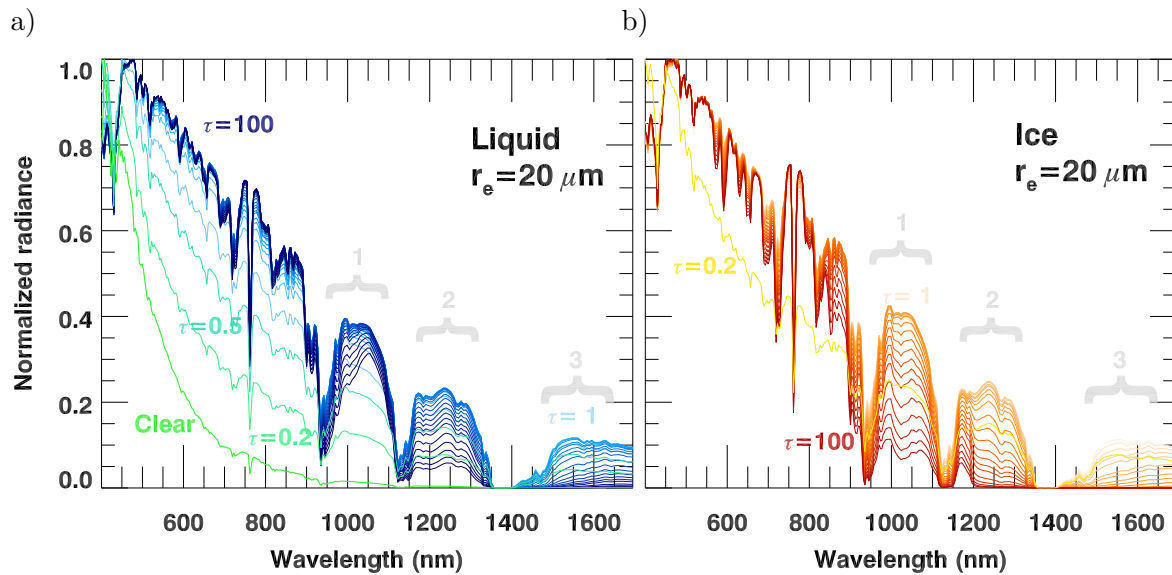


Figure 3.6: Normalized radiance spectra for liquid (left) and ice (right) clouds with an  $r_e$  of  $20 \mu\text{m}$  and  $\tau$  varying from 0.2 to 100 (where darker colors denotes optically thicker clouds). A clear sky normalized radiance (denoted in green) is added for comparison to the optically thinnest clouds. Three wavelength ranges where there are spectral features are indicated by the grey curly brackets.

examine three wavelength ranges: 1) 950 - 1100 nm, 2) 1150 - 1350 nm, and 3) 1450 - 1650 nm. The location of the peak radiance in 1) shifts from 1000 nm to 1060 nm as  $\tau$  increases for liquid clouds (Fig. 3.6a). In the same wavelength range, radiance transmitted through an ice cloud has a local radiance minimum that deepens with increases in  $\tau$ . Another spectral feature is observed in normalized radiance transmitted through ice clouds in 2) where radiance at wavelengths longer than 1200 nm is preferentially absorbed. As  $\tau$  increases, the normalized radiance in 2) changes from a convex shape with a local maximum at 1230 nm, to a concave shape with a local minimum. The spectral feature in 3) is a curved shape with a maximum near 1500 nm that flattens with increases of  $\tau$  for both ice and liquid clouds.

Since these spectral features are linked to absorption, whenever the transmittance is entirely attenuated, these features disappear. This attenuation occurs at lower  $\tau$  for ice clouds than liquid clouds in the wavelength range 1500 - 1600 nm (see Fig. 3.6). This is caused by higher ice absorption than liquid in that wavelength range (see Fig. 3.4a). Transmittance through ice clouds at 1250 nm is also entirely attenuated at lower  $\tau$  than at 1180 nm, because of higher absorption at 1250 nm

than 1180 nm.

For clouds with  $\tau < 4$ , where radiance in the midvisible is still increasing with  $\tau$ , the transmittance spectra show an influence from molecular scattering. The spectra in Fig. 3.6a for  $\tau = 0.2$  matches more closely the clear sky spectra, which is inversely proportional to the 4<sup>th</sup> power of the wavelength, than the normalized radiance spectra for  $\tau = 100$ , which is roughly proportional to the inverse of the wavelength. As  $\tau$  is reduced, the magnitude of signal at wavelengths between 550 nm and 700 nm decreases and its slope becomes more negative, until they match the spectrum of clear sky. The clear sky spectrum (green spectrum in Fig. 3.6a) is entirely dependent on scattering by molecules (Rayleigh scattering) and the solar zenith angle. The slope of the spectrum in the visible is proportional to  $\tau$  until scattering by cloud particles dominates scattering by molecules. This transition occurs at lower  $\tau$  for ice clouds (near 1) than liquid clouds (near 2), obscured by radiance transmitted through optically thicker clouds in Fig. 3.6. After this transition, the slope of normalized radiance in the visible varies less and depends on  $\tau$ ,  $r_e$ , and  $\phi$ , rather than on molecular scattering.

The normalized spectra are modified by  $\phi$  and  $r_e$ , especially in the 3 wavelength ranges which show variations with  $\tau$ . Changes of transmittance due to  $\phi$  and  $r_e$ , when  $\tau$  is kept constant, can be observed in Fig. 3.7. Outside of these 3 wavelength ranges and gas absorption bands, transmittance through both liquid and ice clouds overlaps for all cloud particle sizes, except for particles smaller than  $5 \mu\text{m}$ . In the 3 wavelength ranges, ice and liquid clouds can be distinguished by the shape and magnitude of the transmittance. Transmittance for ice clouds has the largest dynamic range with  $r_e$  in the wavelength regions 1) and 2), while for liquid clouds it varies the most with  $r_e$  in the wavelength region 3) (see Fig. 3.7). In the wavelength range 1), the local minimum observed for ice clouds deepens as cloud particle sizes increase, whereas liquid water cloud transmittance does not produce a local minimum. For the spectral range 2), transmittance through a liquid cloud with distinct  $r_e$  (denoted by the thin lines with different shadings of blue in Fig. 3.7) varies only by the mean magnitude. In the same range, the peak signal at 1230 nm for ice clouds (denoted by different shadings of orange in Fig. 3.7) vanishes for largest  $r_e$ , resulting in a concave shape.

Transmittance in 3) tends to 0 for ice clouds, but not for liquid water clouds. The magnitude and spectral slope of liquid water cloud transmittance in 3) are reduced as  $r_e$  increases.

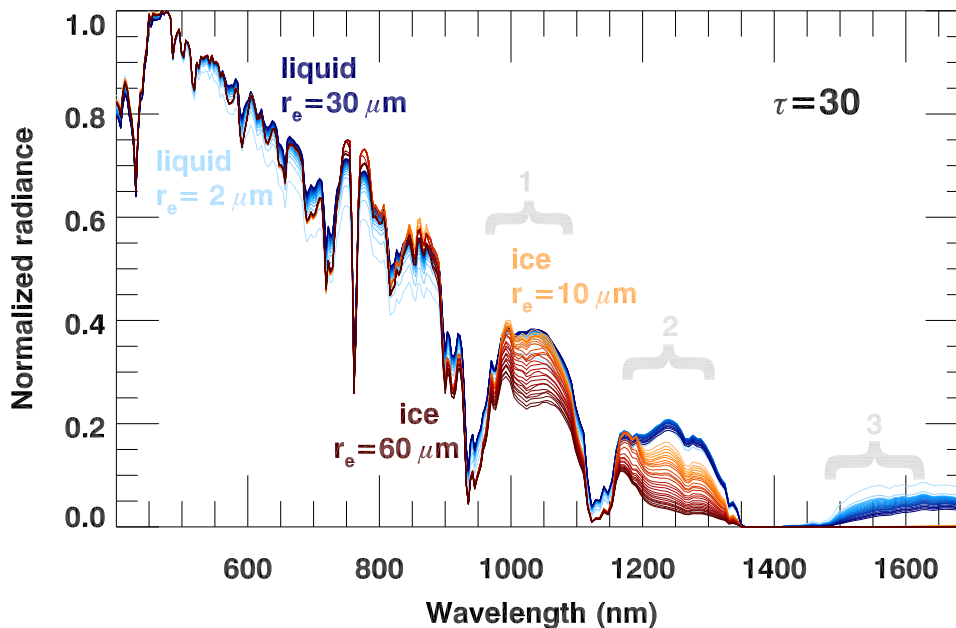


Figure 3.7: Normalized radiance spectra transmitted through liquid and ice clouds of  $\tau$  of 30 and  $r_e$  ranging from  $2 \mu\text{m}$  to  $30 \mu\text{m}$  for liquid clouds and  $10 \mu\text{m}$  to  $60 \mu\text{m}$  for ice clouds. Darker orange lines represent radiance spectra transmitted through larger ice particles. Darker blue lines represent the radiance spectra transmitted through larger liquid cloud droplets. 3 wavelength ranges where there are spectral features are indicated by the grey curly brackets.

### 3.4.5 Definition of spectral parameters

To quantify the spectral features discussed in Sect. 3.4.4, we introduce 15 parameters, designated by  $\eta_1$  through  $\eta_{15}$ , with distinct spectral transmittance characteristics that will be used to infer cloud properties. The features represent the largest patterns of variations (outside of those due to water vapor) that were observed in a set of over 800,000 cloud transmittance spectra spanning 15 days. In order to minimize the influence of water vapor on the cloud retrieval, wavelength ranges were restricted to those where water vapor absorption changed the signal by less than 5% for precipitable water ranging from 0 mm to 40 mm. This is a far larger range of precipitable water observed over Boulder, where the mean is about 11 mm.

The largest variability in spectral features is found in the 3 wavelength regions identified in Fig. 3.6 and Fig. 3.7, and has been quantified by 13 of the 15 parameters. The transmittances in a subset of wavelengths used to calculate the first 3 parameters are highlighted in Fig. 3.8. The first spectral feature is the peak radiance in the wavelength range 1). It is quantified by the curvature of the radiance spectrum, normalized by the radiance at 1000 nm, and denoted by parameter 1, or  $\eta_1$ . The curvature is calculated from the area bounded by the transmittance and a linear interpolation between 1000 nm and 1100 nm, and is the sum of the difference between the transmittance and the linear interpolation at every wavelength. It is represented by the shaded area in Fig. 3.8. As  $\tau$  increases, the shaded area for liquid clouds increases (for ice clouds, it decreases), which consequently increases (decreases)  $\eta_1$ . The change in spectral transmittance through ice clouds in 2), which is transformed from convex to concave curvature around 1230 nm as  $\tau$  increases, is quantified by the 2nd parameter,  $\eta_2$ . This parameter is the spectral derivative of transmittance at 1200 nm, at the edge of the convex/concave shape with a maximum/minimum at 1230 nm.  $\eta_2$  is identified by 2 and is highlighted to illustrate the trend with varying  $\tau$  for ice clouds in Fig. 3.8. The spectral feature in 3), the curvature, is diminished as  $\tau$  increases. This spectral feature is quantified with parameter  $\eta_3$ .  $\eta_3$  is defined by the spectral derivative of transmittance at 1500 nm, which decreases with increasing  $\tau$  for both ice and liquid clouds.

10 more parameters were defined to quantify the similar spectral features in the 3 wavelength ranges.  $\eta_7$ ,  $\eta_9$ ,  $\eta_{12}$ , and  $\eta_{13}$  are defined within region 1) by the mean magnitude of normalized radiance ( $\eta_7$ ); the slope of the spectral derivative ( $\eta_9$ ); the value of the normalized radiance at one wavelength ( $\eta_{12}$ ); and the ratio of radiances at two different wavelengths ( $\eta_{13}$ ). In region 2), 3 additional parameters were defined by: the ratio of radiances at two different wavelengths ( $\eta_4$ ); the mean magnitude of normalized radiance ( $\eta_5$ ); and the slope of the spectral derivative ( $\eta_{10}$ ). For region 3),  $\eta_8$  quantifies the curvature by the same method described for  $\eta_1$ . In addition,  $\eta_6$  and  $\eta_{15}$  quantify the mean normalized radiance and the spectral slope in region 3), respectively. The equations used calculate all 15 spectral parameters, and short descriptions of the spectral parameter with expected behavior are listed in Table 3.1.

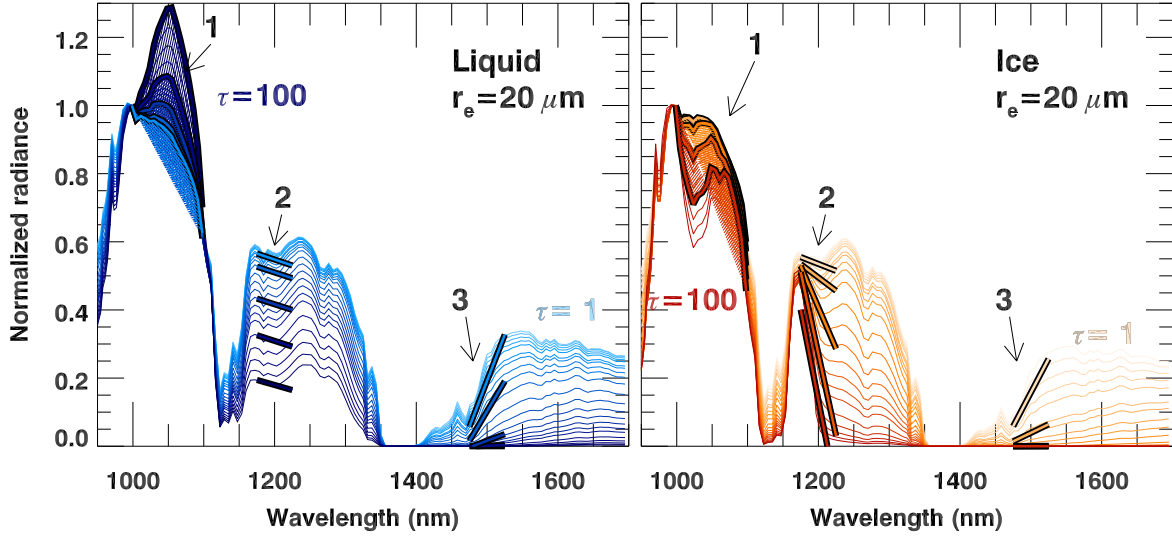


Figure 3.8: Radiance spectra normalized by its value at 1000 nm for liquid (left) and ice (right) clouds with  $r_e = 20 \mu\text{m}$  and  $\tau$  varying from 1 to 100 (where darker colors denotes optically thicker clouds). Three spectral features, which vary with changes of  $\tau$ , (see text) are quantified by the first 3 parameters,  $\eta_1$ ,  $\eta_2$ , and  $\eta_3$ . The transmittance that contribute to calculating  $\eta_1$ ,  $\eta_2$ , and  $\eta_3$  are highlighted and indicated by the numbers 1, 2, and 3, respectively. The shaded areas indicated by 1 overlap for different optical thickness. To increase visibility of the smaller shaded areas (denoted by lighter blues and darker oranges), these are plotted in front of the larger shaded areas.

The characteristics in a fourth spectral region, between 530-610 nm exhibiting spectral variability in cloud transmittance are the basis for defining an additional parameter. For transmittance from clouds with  $\tau < 4$ , the spectral slope in this regions becomes progressively more negative and the magnitude of transmittance decreases as  $\tau$  decreases, until it reduces to the clear sky spectrum (see Fig. 3.9a).  $\eta_{11}$  quantifies the spectral slope of normalized radiance between 530 nm and 610 nm, highlighted in Fig. 3.9a. The slopes calculated from these and other normalized spectra increase with  $\tau$  until a maximum is reached (see Fig. 3.9b) at a value of  $\tau \sim 3$  for ice clouds and  $\tau$  up to 7 for liquid clouds.

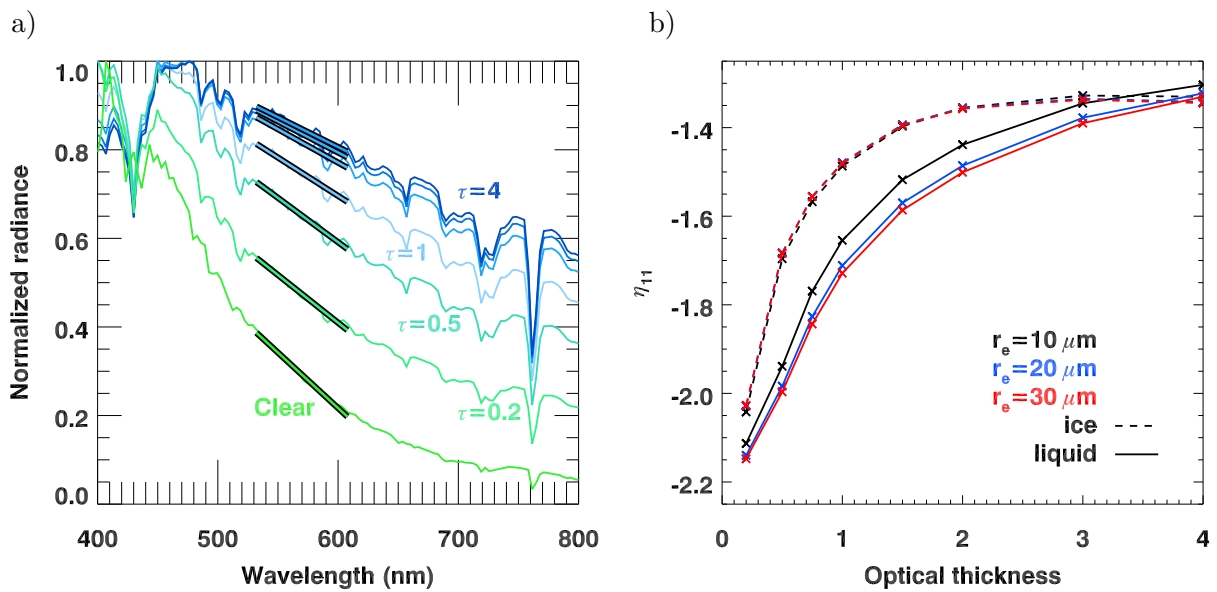


Figure 3.9: (a) Transmittance of liquid water clouds of varying optical thickness and effective radius of 20  $\mu\text{m}$  and (b) the slope of normalized radiance for the wavelength range in 530 - 610 nm,  $\eta_{11}$ , as a function of  $\tau$  for ice and liquid clouds, evaluated for 3 different effective radii. In (a), the slope in the visible is identified by the highlighted region. The normalized radiance spectra and the  $\eta_{11}$  calculated from them were modeled with ancillary inputs based on 2012-05-25, for a solar zenith angle of  $50^\circ$ .

Table 3.1: Definition, wavelength range used, and expected behavior for the 15 spectral parameters.  $L_\lambda$  indicates the radiance evaluated at a wavelength,  $\lambda$ , in microns. The function  $lin(y; \lambda = a..b)$  describes the linear fit of values evaluated at  $\lambda = a$  and  $\lambda = b$ , where  $y$  represents any variable that is calculated from the radiance spectrum. The function  $m(y; \lambda = a..b)$  describes the slope of  $y$  evaluated over the range of  $\lambda = a$  to  $\lambda = b$ . The average value of  $y$  over the range of  $\lambda = a$  to  $\lambda = b$  is presented as  $\langle y \rangle|_{\lambda=a}^b$ . In addition to defining each spectral parameter by the symbol  $\eta_1$  through  $\eta_{15}$ , other symbols are used to provide additional insight into the nature of the parameter. For parameters defined by a measure of the curvature of radiance,  $C_\lambda$  is used, where a convex curvature represents a slope that decreases with increasing wavelength, and concave curvature for a slope that increases with increasing wavelength. The spectral derivatives of the normalized radiances are denoted by  $\partial/\partial\lambda$ . When this derivative, as a function of wavelength, is fitted to a line, its slope is represented by  $\partial^2/\partial\lambda^2$ . The slope of this derivative over a wavelength range is roughly equivalent to the average second derivative over the same wavelength range, but differences may result from the linear fitting process. Slopes, ratios, mean, and normalized radiances are presented as  $sl_\lambda$ ,  $r_\lambda$ ,  $\langle R \rangle_\lambda$ , and  $R_\lambda$  respectively, with  $\lambda$  denoting a representative wavelength in microns where the features are quantified.

	Wavelength(s) (nm)	Calculation	Method	Units	Description and expected behavior
$\eta_1$	1000– 1100	$C_{1.0} = \sum_{\lambda=1.0}^{1.1} \left( \frac{L(\lambda)}{L_{1.0}} - lin \left( \frac{L(\lambda)}{L_{1.0}}; \lambda=1.0..1.1 \right) \right)$	Curvature	–	At $\tau > 30$ , the curvature is positive for liquid clouds, and negative for ice clouds. Separation between ice and liquid clouds is larger for larger $r_e$ . Positive values represent a convex shape, while negative values represent a concave shape.
$\eta_2$	1200	$\partial/\partial\lambda_{1.2} = \frac{\partial}{\partial\lambda} \frac{L_{1.2}}{L_{1.0}}$	Derivative	$\mu\text{m}^{-1}$	Not dependent on $\tau$ and $r_e$ for liquid clouds, but becomes more negative for ice clouds as $\tau$ and $r_e$ are increased.
$\eta_3$	1500	$\partial/\partial\lambda_{1.5} = \frac{\partial}{\partial\lambda} \frac{L_{1.5}}{L_{1.0}}$	Derivative	$\mu\text{m}^{-1}$	Sensitive to differences in ice and liquid cloud with $\tau < 10$ . $\eta_3$ decreases as $r_e$ decreases and $\tau$ increases.
$\eta_4$	1200 & 1237	$r_{1.2} = \frac{L_{1.2}}{L_{1.237}}$	Ratio	–	Dependent on $\tau$ and $r_e$ for ice cloud especially for $\tau > 30$ , but not for liquid cloud. Increases with increasing $\tau$ of ice clouds.
$\eta_5$	1245– 1270	$\langle R \rangle_{1.25} = \left\langle \frac{L(\lambda)}{L_{max}} \right\rangle _{\lambda=1.245}^{1.27}$	Mean	–	Dependent on cloud water content independent of $\phi$ . Decreases with increasing water content.

Continued on next page

Table 3.1: (continued)

	Wavelength(s) (nm)	Calculation	Method	Units	Description and expected behavior
$\eta_6$	1565– 1640	$\langle R \rangle_{1.6} = \langle \frac{L(\lambda)}{L_{max}} \rangle  _{\lambda=1.565}^{1.64}$	Mean	–	Dependent on $\tau$ , $r_e$ , and $\phi$ for $\tau < 30$ . Decreases with increasing $\tau$ . Larger decrease for ice cloud than liquid cloud.
$\eta_7$	1000– 1050	$\langle R \rangle_{1.0} = \langle \frac{L(\lambda)}{L_{max}} \rangle  _{\lambda=1.0}^{1.05}$	Mean	–	Dependent on cloud water content, with only small variation due to $\phi$ as compared to variations due to $\tau$ . Decreases with increasing water content for ice cloud $\tau > 10$ , and liquid cloud $\tau > 20$ .
$\eta_8$	1490– 1600	$C_{1.6} = \sum_{\lambda=1.49}^{1.6} \left( \frac{L(\lambda)}{L_{1.0}} - \ln \left( \frac{L(\lambda)}{L_{1.0}}; \lambda=1.49..1.6 \right) \right)$	Curvature	–	Decreases with increasing $\tau$ . Clear separation between ice and liquid cloud, and $r_e$ at $\tau < 30$ . Positive values represent a convex shape, while negative values represent a concave shape.
$\eta_9$	1000– 1080	$\partial^2 / \partial \lambda_{1.0}^2 = m \left( \frac{\partial}{\partial \lambda} \frac{L(\lambda)}{L_{1.0}}; \lambda=1.0..1.08 \right)$	Slope of derivative	$\mu\text{m}^{-1}$ $\text{nm}^{-1}$	Increases with increasing ice cloud $\tau$ , but decreases with increasing liquid cloud $\tau$ . These changes are amplified as $r_e$ increases. Positive values only for ice cloud.
$\eta_{10}$	1200– 1310	$\partial^2 / \partial \lambda_{1.2}^2 = m \left( \frac{\partial}{\partial \lambda} \frac{L(\lambda)}{L_{1.0}}; \lambda=1.2..1.31 \right)$	Slope of derivative	$\mu\text{m}^{-1}$ $\text{nm}^{-1}$	Only ice clouds produce positive values. Increases with increasing ice cloud $\tau$ , and decreases with $\tau$ in liquid clouds for $\tau < 50$ .
$\eta_{11}$	530- 610	$sl_{0.55} = m \left( \frac{L(\lambda)}{L_{max}}; \lambda=0.53..0.61 \right)$	Slope	$\mu\text{m}^{-1}$	Largest gradient due to $\tau$ occurs at $\tau < 4$ . Dependence on $r_e$ and solar zenith angle for $\tau > 10$ .
$\eta_{12}$	1040	$R_{1.04} = \frac{L_{1.04}}{L_{max}}$	Normalized radiance	–	Smaller variations due to $r_e$ than $\eta_7$ . Decreases with decreasing $\tau$ for clouds of $\tau > 20$ .
$\eta_{13}$	1000 & 1065	$r_{1.0} = \frac{L_{1.0}}{L_{1.065}}$	Ratio	–	Decreases with increasing liquid cloud $\tau$ and $r_e$ . Increases with increase in ice cloud $\tau$ .

Continued on next page

Table 3.1: (continued)

Wavelength(s) (nm)	Calculation	Method	Units	Description and expected behavior
$\eta_{14}$ 600 & 870	$r_{0.6} = \frac{L_{0.6}}{L_{0.87}}$	Ratio	–	Most sensitive to $\tau$ for clouds with $\tau < 20$ . Little variation due to liquid $r_e$ compared to variations due to $\tau$ . Larger variations due to ice $r_e$ than $\tau$ .
$\eta_{15}$ 1565– 1634	$sl_{1.6} = m \left( \frac{L(\lambda)}{L_{1.565}}; \lambda=1.565..1.634 \right)$	Slope	$\mu\text{m}^{-1}$	Increases with increase in $\tau$ and $r_e$ . Larger increase for ice clouds than for liquid clouds same parameter introduced by <i>McBride et al.</i> [2011] but calculated from normalized radiance and not transmittance.

### 3.4.6 Dependence on thermodynamic phase, optical thickness, and effective radius

The dependencies of the 15 parameters (Sect. 3.4.5; Table 3.1) on  $\tau$  for ice clouds (dashed) and liquid clouds (solid) and for 3 different particle sizes are shown in Fig. 3.10. The accuracy for each of the parameters is estimated by propagating the measurement accuracy through the formula in Table 3.1. Modeled spectra are evaluated with the variation of SSFR's 3 radiometric calibrations and their related precision (Sect. 3.2.1). The standard deviation of the set of spectral parameters calculated from these modeled spectra is represented by the shaded area for each parameter in Fig. 3.10.

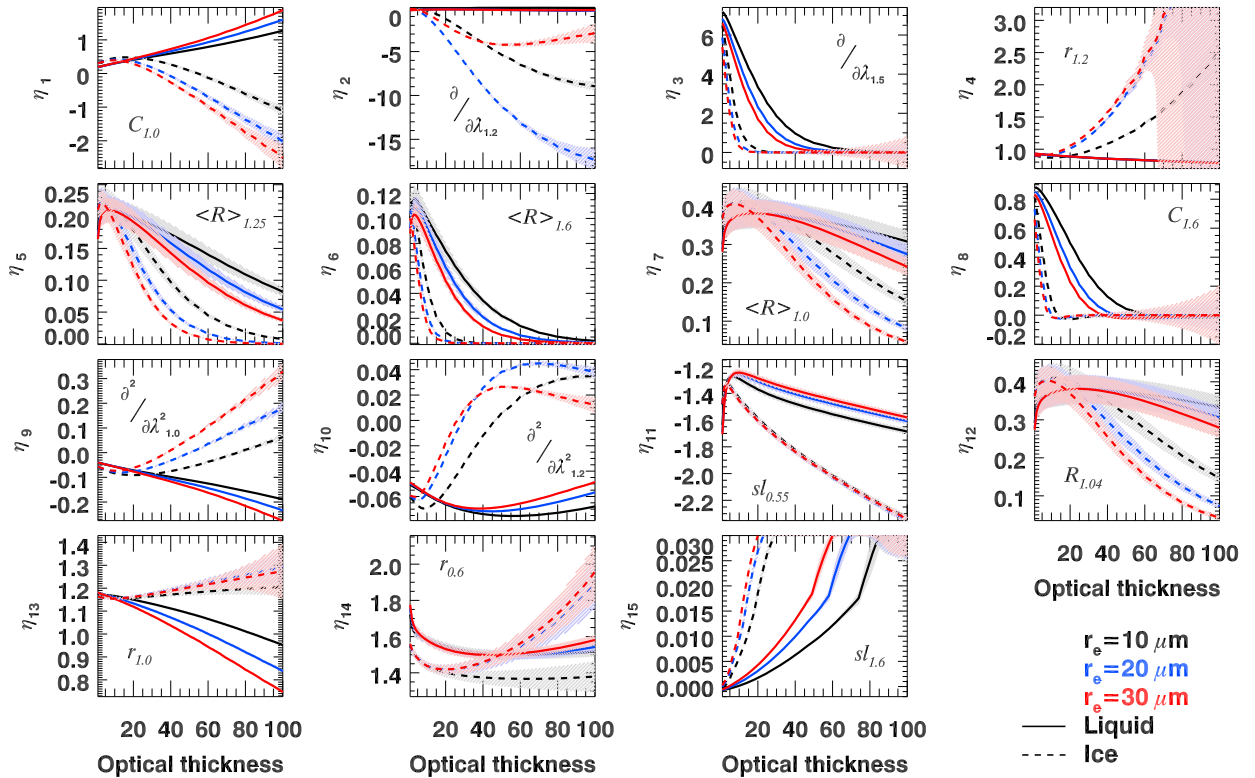


Figure 3.10: The value of the parameters,  $\eta_1$  through  $\eta_{15}$ , as a function of optical thickness for 3 effective radii (colors) for liquid (solid) and ice (dashed) clouds. The shading surrounding each line denotes the standard deviation of the variability in the parameters due to measurement uncertainty (see text).

Parameter sensitivity to  $\tau$ ,  $r_e$ , and  $\phi$  is larger than the measurement uncertainty (see Fig. 3.10), for several parameters, clearly establishing their suitability for distinguishing cloud properties.

For clouds with  $\tau < 10$ , the most appropriate parameters are:  $\boldsymbol{\eta}_3$ ,  $\boldsymbol{\eta}_8$ , and  $\boldsymbol{\eta}_{10}$  ( $\partial/\partial\lambda_{1.5}$ ,  $C_{1.6}$ , and  $\partial^2/\partial\lambda_{1.2}^2$ ). For clouds with  $\tau > 10$ , the spectral parameters  $\boldsymbol{\eta}_6$  and  $\boldsymbol{\eta}_{15}$  ( $\langle R \rangle_{1.6}$  and  $sl_{1.6}$ ) have largest sensitivity to  $\tau$  and  $r_e$ . The most suitable parameters for ice clouds are:  $\boldsymbol{\eta}_1$ ,  $\boldsymbol{\eta}_2$ , and  $\boldsymbol{\eta}_9$  ( $C_{1.0}$ ,  $\partial/\partial\lambda_{1.2}$ , and  $\partial^2/\partial\lambda_{1.0}^2$ ). The largest sensitivity to  $\tau$ , regardless of  $r_e$  and  $\phi$  is found in  $\boldsymbol{\eta}_{11}$  ( $sl_{0.55}$ ).

### Thermodynamic Phase

Thermodynamic phase is the largest contributor to the variability in  $\boldsymbol{\eta}_1$ ,  $\boldsymbol{\eta}_2$ ,  $\boldsymbol{\eta}_4$ ,  $\boldsymbol{\eta}_9$ ,  $\boldsymbol{\eta}_{10}$ , and  $\boldsymbol{\eta}_{13}$  ( $C_{1.0}$ ,  $\partial/\partial\lambda_{1.2}$ ,  $r_{1.2}$ ,  $\partial^2/\partial\lambda_{1.0}^2$ ,  $\partial^2/\partial\lambda_{1.2}^2$ , and  $r_{1.0}$  respectively). This is shown by the separability between the values of these parameters evaluated for a liquid cloud compared to an ice cloud (see Fig. 3.10). These parameters exploit spectral features that depend on cloud phase in the wavelength ranges 1) and 2); see Fig. 3.7.

The parameters  $\boldsymbol{\eta}_1$ ,  $\boldsymbol{\eta}_9$ , and  $\boldsymbol{\eta}_{13}$  ( $C_{1.0}$ ,  $\partial^2/\partial\lambda_{1.0}^2$ , and  $r_{1.0}$ ) quantify spectral features in the wavelength range 1). Along with  $\boldsymbol{\eta}_1$ ,  $\boldsymbol{\eta}_9$  also calculates the curvature but by the slope of spectral derivative, where negative values of  $\boldsymbol{\eta}_1$  and positive values of  $\boldsymbol{\eta}_9$  are attained only by ice clouds. Values of  $\boldsymbol{\eta}_{13}$ , lower than 1 are obtained by normalized radiance spectra transmitted through liquid clouds.

In the wavelength range 2), the transmittance for either ice and liquid water cloud result in large differences in the parameters  $\boldsymbol{\eta}_2$ ,  $\boldsymbol{\eta}_4$ , and  $\boldsymbol{\eta}_{10}$  ( $\partial/\partial\lambda_{1.2}$ ,  $r_{1.2}$ , and  $\partial^2/\partial\lambda_{1.2}^2$ ). Values of  $\boldsymbol{\eta}_2$  for liquid water clouds are never lower than  $-0.35 \mu m^{-1}$  and vary little, whereas only ice clouds values as low as  $-21.2 \mu m^{-1}$  (Fig. 3.8). These values hold for the ranges in surface albedo, cloud base height, atmospheric state, and solar zenith angle represented during the cases 2012-05-25 and 2012-08-06. Another measure of the spectral feature in 2) is the ratio of radiance at 1200 nm and 1237 nm ( $\boldsymbol{\eta}_4$ ), which increases to as high as 18.8 with increases in ice cloud  $\tau$ , but varies much less with changes in liquid water cloud properties. The signal to noise ratio of  $\boldsymbol{\eta}_4$  is reduced below 1 for large ice cloud  $\tau$  where the radiance at 1237 nm is entirely attenuated. The curvature of normalized radiance in 2), quantified by  $\boldsymbol{\eta}_2$ , is also quantified by the slope of the spectral derivative,  $\boldsymbol{\eta}_{10}$ , which increases (decreases) with optical thickness for ice (liquid) clouds. When transmittance is nearly entirely attenuated ( $\tau > 40$ ), the concave and convex shapes become less pronounced; therefore,

$\eta_{10}$  decreases for ice clouds, and increases for liquid clouds.

### Optical thickness

Parameters  $\eta_3$ ,  $\eta_5$ ,  $\eta_6$ ,  $\eta_7$ ,  $\eta_8$ ,  $\eta_{11}$ ,  $\eta_{12}$ ,  $\eta_{14}$ , and  $\eta_{15}$  ( $\partial/\partial\lambda_{1.5}$ ,  $\langle R \rangle_{1.25}$ ,  $\langle R \rangle_{1.6}$ ,  $\langle R \rangle_{1.0}$ ,  $C_{1.6}$ ,  $sl_{0.55}$ ,  $R_{1.04}$ ,  $r_{0.6}$ , and  $sl_{1.6}$ ) are most sensitive to changes in  $\tau$ . At  $\tau < 5$ , scattered radiation is the primary contributor to change in  $\eta_5$ ,  $\eta_6$ ,  $\eta_7$ ,  $\eta_{11}$ ,  $\eta_{12}$ , and  $\eta_{14}$ , and it varies with  $\tau$  (see Fig. 3.10). Of these parameters,  $\eta_5$ ,  $\eta_6$ ,  $\eta_7$ , and  $\eta_{12}$  quantify the magnitude of transmittance in all 3 wavelength ranges. Of the remaining parameters,  $\eta_{14}$  quantifies the same spectral feature presented in Fig. 3.9 and quantified by  $\eta_{11}$ . Unlike  $\eta_{11}$ , the influence of the underlying surface albedo on  $\eta_{14}$  increases with increasing  $\tau$  at  $\tau > 5$ , as expected by the physical process described by *Chiu et al.* [2006].

For  $\tau > 5$ , the spectral features that are quantified by  $\eta_3$ ,  $\eta_5$ ,  $\eta_6$ ,  $\eta_7$ ,  $\eta_8$ , and  $\eta_{12}$  ( $\partial/\partial\lambda_{1.5}$ ,  $\langle R \rangle_{1.25}$ ,  $\langle R \rangle_{1.6}$ ,  $\langle R \rangle_{1.0}$ ,  $C_{1.6}$ , and  $R_{1.04}$ ) are increasingly dominated by absorption. This causes a reduction in the magnitude of normalized radiance, evaluated by  $\eta_5$ ,  $\eta_6$ ,  $\eta_7$ , and  $\eta_{12}$ .  $\eta_3$ ,  $\eta_8$ , and  $\eta_{15}$  ( $\partial/\partial\lambda_{1.5}$ ,  $C_{1.6}$ , and  $sl_{1.6}$ ) quantifies the change in 3) due to ice and liquid water absorption, which is enhanced with increasing  $\tau$  due to higher order scattering. When the shape of transmittance flattens,  $\eta_3$  and  $\eta_8$  decrease, while  $\eta_{15}$  increases.

### Effective radius

Effective radius contributes to variability in all 15 parameters. In particular,  $\eta_1$  to  $\eta_{10}$ ,  $\eta_{12}$ ,  $\eta_{13}$ , and  $\eta_{15}$  quantify the spectral features that are linked to absorption modified by  $r_e$ , while  $\eta_3$ ,  $\eta_5$  to  $\eta_8$ ,  $\eta_{11}$ , and  $\eta_{15}$  quantify the changes in the spectral features due to the changes in scattering properties of different  $r_e$ .  $\eta_1$ ,  $\eta_2$ ,  $\eta_3$ ,  $\eta_4$ ,  $\eta_9$ ,  $\eta_{10}$ ,  $\eta_{13}$ , and  $\eta_{15}$  ( $C_{1.0}$ ,  $\partial/\partial\lambda_{1.2}$ ,  $\partial/\partial\lambda_{1.5}$ ,  $r_{1.2}$ ,  $\partial^2/\partial\lambda_{1.0}^2$ ,  $\partial^2/\partial\lambda_{1.2}^2$ ,  $r_{1.0}$ , and  $sl_{1.6}$ ) quantify spectral features that are unique to absorption, which increases with particle size at any one  $\tau$ . In the wavelength range 1), the separation between liquid water and ice values of  $\eta_1$ ,  $\eta_9$ , and  $\eta_{13}$  increases with  $r_e$ .  $\eta_2$ ,  $\eta_4$ , and  $\eta_{10}$  parameterize the transmittance feature in 2) linked to  $r_e$ -dependent ice particle absorption, but not liquid water absorption. For  $\eta_{15}$ , absorption decreases from 1565 nm towards longer wavelengths [*McBride et al.*, 2011] resulting in a dependence on  $r_e$ , also quantified by  $\eta_3$  in the same wavelength region.

Cloud particle size affects  $\eta_3$ ,  $\eta_5$ ,  $\eta_6$ ,  $\eta_7$ ,  $\eta_8$ , and  $\eta_{12}$  ( $\partial/\partial\lambda_{1.5}$ ,  $\langle R \rangle_{1.25}$ ,  $\langle R \rangle_{1.6}$ ,  $\langle R \rangle_{1.0}$ ,  $C_{1.6}$ , and  $R_{1.04}$ ) by modulating the spectral features through scattering and absorption. These spectral parameters are consistently higher at any one  $\tau$  and  $\phi$  for the smallest  $r_e$ , regardless if it is scattering or absorption that dominates.

### 3.5 Retrieval methodology

For any single transmittance spectrum, a single spectral parameter is insufficient to derive  $\tau$ ,  $r_e$ , and  $\phi$ . Multiple spectral parameters can be used to first identify thermodynamic phase ( $\phi$ ), followed by an additional procedure employing additional parameters, to derive  $\tau$  and  $r_e$ . Equation 3.1 is the statistic,  $\chi^2(\tau, r_e, \phi)$ , used to retrieve  $\tau$  and  $r_e$  from a weighted least-squares-fit between modeled and observed values of all 15 parameters ( $i = 1, 2, 3, \dots, 15$ ). The retrieval is defined at the closest match (minimum in  $\chi^2$ ) between measurement-derived parameters,  $\eta_i$ , and the parameters derived from forward-model LUT  $\eta_i^*(\tau, r_e, \phi)$  at cosine of the solar zenith angle closest to that of the observation.

$$\chi^2(\tau, r_e, \phi) = \sum_{i=1}^{15} \frac{1}{w_i} (\eta_i - \eta_i^*(\tau, r_e, \phi))^2 \quad (3.1)$$

In order to properly weight the contributions from each parameter, a factor,  $w_i$ , is derived from the full range of the parameters,  $P_i$ . Not all parameters can be determined with equal certainty; therefore, the measurement uncertainty,  $\Delta\eta_i$ , of each parameter is also included in the weighting factor in a manner similar to *Wan and Li* [1997], where the most uncertain parameter has lowest influence on the solution.

$$w_i = \Delta\eta_i P_i \quad (3.2)$$

$$P_i = \max(\eta_i^*(\tau, r_e, \phi)) - \min(\eta_i^*(\tau, r_e, \phi)) \quad (3.3)$$

Therefore, the maximum contribution of each parameter to  $\chi^2(\tau, r_e, \phi)$  is 1; the theoretical maximum value of  $\chi^2(\tau, r_e, \phi)$  is 15. The full range of each parameter is obtained by the maximum and minimum of the LUTs.

The retrieval process consists of two steps. In the first step, thermodynamic phase,  $\phi$ , can be discriminated by using a single parameter or with the combination of all 15 parameters.  $\boldsymbol{\eta}_1, \boldsymbol{\eta}_2, \boldsymbol{\eta}_4, \boldsymbol{\eta}_9, \boldsymbol{\eta}_{10}$ , and  $\boldsymbol{\eta}_{13}$  ( $C_{1.0}, \partial/\partial\lambda_{1.2}, r_{1.2}, \partial^2/\partial\lambda_{1.0}^2, \partial^2/\partial\lambda_{1.2}^2$ , and  $r_{1.0}$ ) return unique values for either ice or liquid clouds for clouds with optical thickness larger than 10. Positive values for  $\boldsymbol{\eta}_9$  and  $\boldsymbol{\eta}_{10}$ , and negative values for  $\boldsymbol{\eta}_1$ , and  $\boldsymbol{\eta}_2$  values below  $-0.35 \mu m^{-1}$  are unique to ice clouds. Outside this range, both ice and liquid water clouds produce the same parameters, and thus  $\phi$  cannot be discriminated with a single parameter. For all clouds with  $\tau$  lower than 10 (as  $r_e$  increases, this cutoff in  $\tau$  decreases), a combination of all 15 parameters is used to determine  $\phi$  by the best-fit LUT solution identified at the minimum  $\chi^2$  defined in Eq. 3.1. Although multiple parameters are required to discriminate  $\phi$ , this does not mean that  $\phi$  is any less certain than when using a single spectral parameter.

Once  $\phi$  is determined, a second step consists of a  $\phi$ -segregated retrieval of  $\tau$  and  $r_e$ . To apply the  $\phi$ -segregated retrieval, we use the LUT of the appropriate  $\phi$  (either  $\boldsymbol{\eta}_i^*(\tau, r_e, \phi = ice)$  or  $\boldsymbol{\eta}_i^*(\tau, r_e, \phi = liquid)$ ). The LUTs for ice or liquid clouds are defined with different ranges in  $r_e$ , which represent naturally occurring ice or liquid cloud particle size (see Sect. 3.4.3). The retrieved  $\tau$  and  $r_e$  represents the location in the LUT which defines minimum  $\chi^2$ , calculated from Eq. 3.1.

When determining  $\chi^2$ , some of the 15 parameters calculated from the measured spectrum do not fall within the range of the LUT. The parameters that do not fall within the LUT are deemed non-physical and are therefore omitted from the calculation of  $\chi^2$ . Values outside the LUT occur when the signal to noise ratio of the parameter is lower than one, or it is at the limit of ranges within the LUT. An example of small signal to noise ratio occurs for  $\boldsymbol{\eta}_4$  when evaluated for ice clouds with  $\tau > 65$  and  $r_e > 30 \mu m$ ; see the large shaded area in Fig. 3.10. Since each parameter results from different physical processes, the signal to noise ratio may be lower than one for certain parameters but not for others (for example,  $\boldsymbol{\eta}_4$  compared to  $\boldsymbol{\eta}_9$  for ice clouds with  $\tau > 65$ ). Therefore, the

solution may still be valid, even without the contributions from uncertain parameters.

A successful retrieval occurs when the parameters calculated from a measurement spectrum matches those modeled for at least one combination of  $\tau$ ,  $r_e$ , and  $\phi$ . This match is defined where the minimum  $\chi^2$  is lower than predefined value, 0.69. This value represents 4.6% of the total theoretical maximum  $\chi^2$ , which is the same percentage as the uncertainty in normalized radiance spectra (see Sect. 3.2.1).

### 3.5.1 Retrieval uncertainty

To obtain the retrieval uncertainty of  $\tau$  and  $r_e$ , we propagate measurement uncertainty through the retrieval equation. The uncertainty in the parameters,  $\Delta\boldsymbol{\eta}_i$ , and the slope of  $\chi^2$  as a function the parameters quantify the expected variation in  $\chi^2$  resulting from measurement uncertainty, described by  $\Delta\chi^2$  [adapted from *Taylor, 1997*].

$$\Delta\chi^2(\tau, r_e, \phi) = \sum_{i=1}^{15} \left( \frac{\partial\chi^2(\tau, r_e, \phi)}{\partial\boldsymbol{\eta}_i} \Delta\boldsymbol{\eta}_i \right)^2 \quad (3.4)$$

This expected variation in  $\chi^2$  due to measurement uncertainty ( $\pm\Delta\chi^2$ ) results in a range of  $\tau$  and  $r_e$  where  $\chi^2 \pm \Delta\chi^2$  is minimized. The minimum  $\chi^2 - \Delta\chi^2$  ( $\chi^2 + \Delta\chi^2$ ) occurs at the combination of  $\tau|_{\chi^2 - \Delta\chi^2}$  ( $\tau|_{\chi^2 + \Delta\chi^2}$ ) and  $r_e|_{\chi^2 - \Delta\chi^2}$  ( $r_e|_{\chi^2 + \Delta\chi^2}$ ). The difference between  $\tau$  and  $r_e$  evaluated at the extremes of the range of variability of  $\chi^2$ , represent their respective uncertainty,  $\Delta\tau$  and  $\Delta r_e$ .

$$\Delta\tau = \frac{1}{2} \left| \tau|_{\chi^2 - \Delta\chi^2} - \tau|_{\chi^2 + \Delta\chi^2} \right| \quad (3.5)$$

$$\Delta r_e = \frac{1}{2} \left| r_e|_{\chi^2 - \Delta\chi^2} - r_e|_{\chi^2 + \Delta\chi^2} \right| \quad (3.6)$$

### 3.5.2 Comparisons to other methods

The retrieval described herein is compared to two other methods: the method developed by *McBride et al. [2011]*, hereafter named the slope method, and the standard 2-wavelength method

often used in reflectance [Nakajima and King, 1990] but applied to transmittance as described by Kikuchi *et al.* [2006], hereafter named the 2-wavelength method.

### Slope method

The slope method uses transmittance at 515 nm and the slope of transmittance at 1565–1634 nm normalized by the transmittance value at 1565 nm to retrieve  $\tau$  and  $r_e$ . A least squares fit matches measured transmittance and slope values to a LUT containing modeled transmittances and slopes for a set of  $\tau$  and  $r_e$ . The retrieval is successful if the uncertainty in  $r_e$  is smaller than  $2 \mu\text{m}$ . The LUTs used for this retrieval method are based on the same radiative transfer calculations introduced in Sect. 3.4.1. For cases A and B, the slope method is applied using a liquid cloud LUT, while for case C, an ice cloud LUT is used. Case C represents the first time the method described by McBride *et al.* [2011], is applied to an ice cloud. For this case, all retrieved values are presented, even if the uncertainty in  $r_e$  is larger than  $2 \mu\text{m}$ .

### 2-wavelength method

The 2-wavelength method retrieves  $\tau$  and  $r_e$  using transmittance at wavelengths in the mid-visible (e.g., 515 nm) and in the near-infrared (e.g., 1630 nm) with a LUT, similarly to the current works method and the slope method. Kikuchi *et al.* [2006] employed transmittance evaluated at 1020 nm and 1600 nm. For this work, we follow the description of the standard method presented by McBride *et al.* [2011], which employs transmittance at 515 nm and 1630 nm to retrieve  $\tau$  and  $r_e$ . Although the 2-wavelength method produces large uncertainties in  $r_e$  when applied to clouds with  $\tau < 25$ , we still apply it here, and report the associated uncertainties. The uncertainties in  $\tau$  and  $r_e$  are calculated by the same method described by McBride *et al.* [2011], but applied to the measurement uncertainty of the SSFR (8%) used in this work. Similarly to the slope method, the 2-wavelength retrieval employs a liquid water cloud LUT for cases A and B and an ice cloud LUT for case C.

### Comparison of time series

Figure 3.11 shows the time series of  $\tau$ ,  $r_e$ , and  $\phi$  retrieved using the 15-parameter method (this work), the slope retrieval, and the 2-wavelength retrieval based on transmitted radiance for

the (A) liquid, (B) mixed-phase, and (C) ice cloud cases.

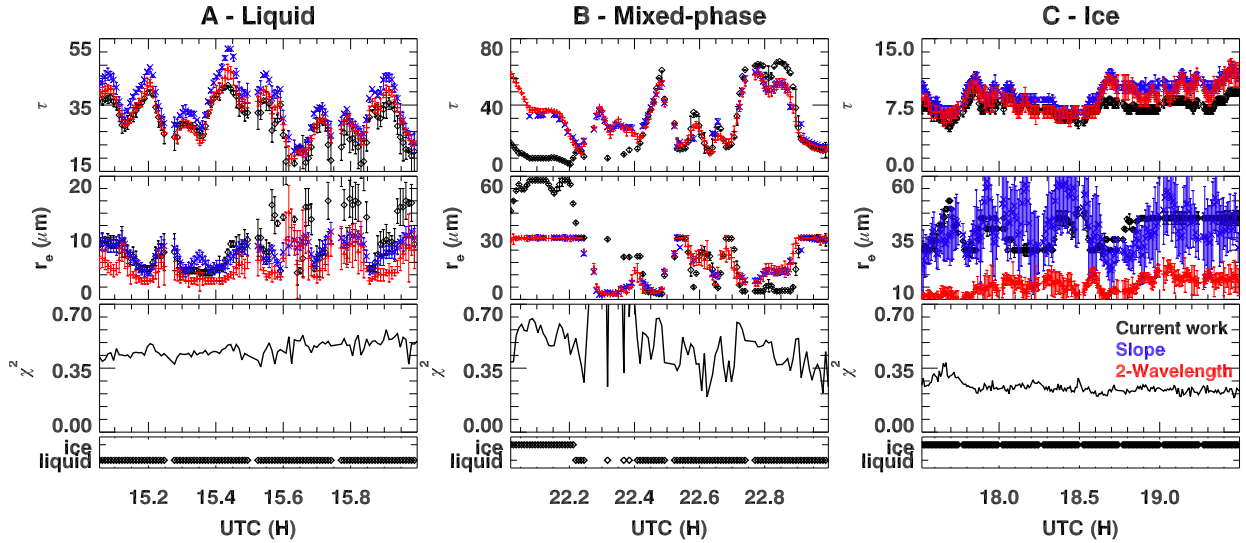


Figure 3.11: Time series of retrieved cloud properties determined by 3 different transmittance based retrieval methods; case A (left) for liquid cloud, case B (center) for mixed-phase cloud, and case C (right) for ice cloud. The mixed-phase cloud case represents a span in time where both ice and liquid water cloud particles are expected to have been present. Colors represent three different cloud retrieval methods: this work (black), the slope method (blue) and the 2-wavelength method (red). For each case study, the top-most panel presents the retrieved optical thickness,  $\tau$ , the panel directly below shows the effective radius,  $r_e$ , the panel directly below shows the minimum  $\chi^2$  determined by this work (15-parameter method), and the lowest panel shows thermodynamic phase,  $\phi$ , designated by this work. The y-axis scale in  $\tau$  and  $r_e$  differs for each case.

The ancillary data (discussed in Sect. 3.4.2) and the 15-parameter method classified each case with the same thermodynamic phase. The  $\tau$  retrieved with all 3 methods follows similar trends, albeit with different magnitudes. One exception is the start of case B, where the 15-parameter method retrieved ice clouds with much lower  $\tau$  than the other two methods. The retrieved  $r_e$  based on all 3 methods also follow the similar trends; again, the onset of case B is anomalous, as is the 2-wavelength method in case C. In addition, the uncertainty in the 15-parameter method retrievals is lower than that for the other two methods, especially for case C, with an average  $r_e$  uncertainty of  $\pm 1.2 \mu\text{m}$  smaller by a factor of at least 2.5 for the slope and 2-wavelength method respectively.

For case A, the 15-parameter method retrieved  $\tau$  matches more closely to the 2-wavelength method (mean difference of 2.5) than the slope method (mean difference of 5.6), while the retrieved

$r_e$  matches more closely the slope method (mean difference of  $2.6 \mu\text{m}$ ) than the 2-wavelength method (mean difference of  $4.4 \mu\text{m}$ ). The largest differences occur between  $\tau$  retrieved with the 15-parameter method and  $\tau$  retrieved with the slope method, whenever the 15-parameter  $\tau$  is larger than 30. The range of  $\tau$  retrieved with all three methods is never larger than 8 for the times between 15.0 - 15.4 UTC. This period coincides with times where the uncertainty in  $\tau$  for the 15-parameter method is lowest, with a mean of  $\pm 1.2$  and the average retrieved  $\tau$  is highest at 32. This mean uncertainty increases to  $\pm 2.6$  for later times, where the average  $\tau$  decreases to 28. The slope and 2-wavelength method retrieved an uncertainty of  $\tau$  consistent throughout the measurement period, with averages of  $\pm 1.3$  and  $\pm 1.5$  respectively. Additional comparisons for this case are presented below.

Similarly to the comparison of  $\tau$  for case A, the effective radii retrieved by all 3 methods matches more closely (within  $5 \mu\text{m}$ ) during the period from 15.0 - 15.4 UTC than the later period (within  $10 \mu\text{m}$ ). The uncertainty of  $r_e$  for all 3 methods is also lower in the earlier period (a mean of  $\pm 1 \mu\text{m}$  for all 3 methods) than the later period (a mean of  $\pm 1.9 \mu\text{m}$ ). Higher than average  $r_e$  uncertainty coincides with retrieved  $\tau$  lower than 20 for all 3 methods. Such behavior for low  $\tau$  has been observed previously for the slope and 2-wavelength method [Coddington *et al.*, 2013; McBride *et al.*, 2011]. The  $r_e$  retrieved with the current work is within the uncertainty range of  $r_e$  retrieved with the 2-wavelength method for 27% and the slope method for 69% of the time series.

Case B presents examples of retrieval behavior under conditions of liquid and ice cloud particle absorption. Although we have not addressed the applicability of the 15 spectral parameters to mixed phase clouds in this work, we investigate the results of the thermodynamic phase discrimination, and the residual of least squares fit of the retrieval to measured transmittance under conditions of concurrent ice and liquid absorption. The thermodynamic phase retrieval coincides with the thermodynamic phase retrieved by GOES, which was ice prior to, and liquid during the measurement period. The largest  $\chi^2$  occurs between 22.2 UTC and 22.4 UTC, when the thermodynamic phase transitions from an ice cloud to a liquid cloud, as determined by the 15-parameter method. In this transition zone, only 40% of the solutions obtained by the retrieval described herein

are valid. Large residuals indicate that more information is required to reproduce the parameters calculated from the measurements of transmittance spectra. Beyond this transition period, the match between  $\tau$  retrieved from all 3 methods is exceptional, especially since none of the retrievals explicitly takes into account mixed-phase clouds. The overall trend is reproduced with all 3 retrieval methods and they differ by an average of 5.8 in retrieved  $\tau$  and 4.7  $\mu\text{m}$  in retrieved  $r_e$ , for the period later than 22.4 UTC. At these times, uncertainties in  $r_e$  are greater than  $\pm 2 \mu\text{m}$  for 13% of the time series for the current method, 26% for the slope method and 44% for the 2-wavelength method.

For case C, the match in  $\tau$  retrieved with all 3 methods differs by less 3 throughout the entire time series even though the retrieved  $r_e$  differs by as much as 37  $\mu\text{m}$ . The re uncertainty is larger than  $\pm 2\mu\text{m}$  at all times for the slope method, 62% of the time series for the 2-wavelength method, and 29% of the time series when retrieved with the 15-parameter method. These large uncertainties obtained from the slope and 2-wavelength method are likely due to a lower signal to noise ratio of ice cloud transmittance compared to a liquid water cloud transmittance near 1600 nm. This low signal can be observed in the ice cloud transmittance spectrum for a  $\tau = 10$  with  $r_e = 20 \mu\text{m}$  (Fig. 3.5a). The smaller  $r_e$  uncertainties obtained by the 15-parameter method compared to the slope and 2-wavelength retrieval is also expected. Specific parameters were designed to take advantage of features that have high signal to noise ratio for ice and liquid clouds [e.g.,  $\boldsymbol{\eta}_1$  ( $C_{1.0}$ ),  $\boldsymbol{\eta}_2$  ( $\partial/\partial\lambda_{1.2}$ ),  $\boldsymbol{\eta}_9$  ( $\partial^2/\partial\lambda_{1.0}^2$ ),  $\boldsymbol{\eta}_{10}$  ( $\partial^2/\partial\lambda_{1.2}^2$ ), and  $\boldsymbol{\eta}_{13}$  ( $r_{1.0}$ )].

During the ice cloud case C, MODIS observed the same cloud at 18.17 UTC. Keep in mind that  $\tau$  and  $r_e$  retrieved by MODIS were from sampling volume close to cloud top, unlike the transmittance based 15-parameter method. Note also the spatial resolution of MODIS, 1  $\text{km}^2$ , versus that of the zenith-pointing SSFR, estimated to be 0.45  $\text{km}^2$  for a cloud base at 7.5 km. At 18.17 UTC, the 15-parameter method retrieved  $\tau = 8 \pm 0.5$  and  $r_e = 30 \pm 2 \mu\text{m}$ , while MODIS retrieved  $\tau = 12.7 \pm 15.3$  and  $r_e = 17.1 \pm 5.4 \mu\text{m}$  with very good confidence for both  $\tau$  and  $r_e$  retrievals [Platnick *et al.*, 2003]. The 15-parameter  $\tau$  retrieval falls within the uncertainty range of MODIS. The difference in retrieved  $r_e$  is likely due to the difference between particle sizes at cloud top and

particle sizes throughout the cloud. Both the slope and 2-wavelength methods resulted in failed retrievals at this time.

### Comparison of retrieved $\tau$ and $r_e$ for the liquid cloud case

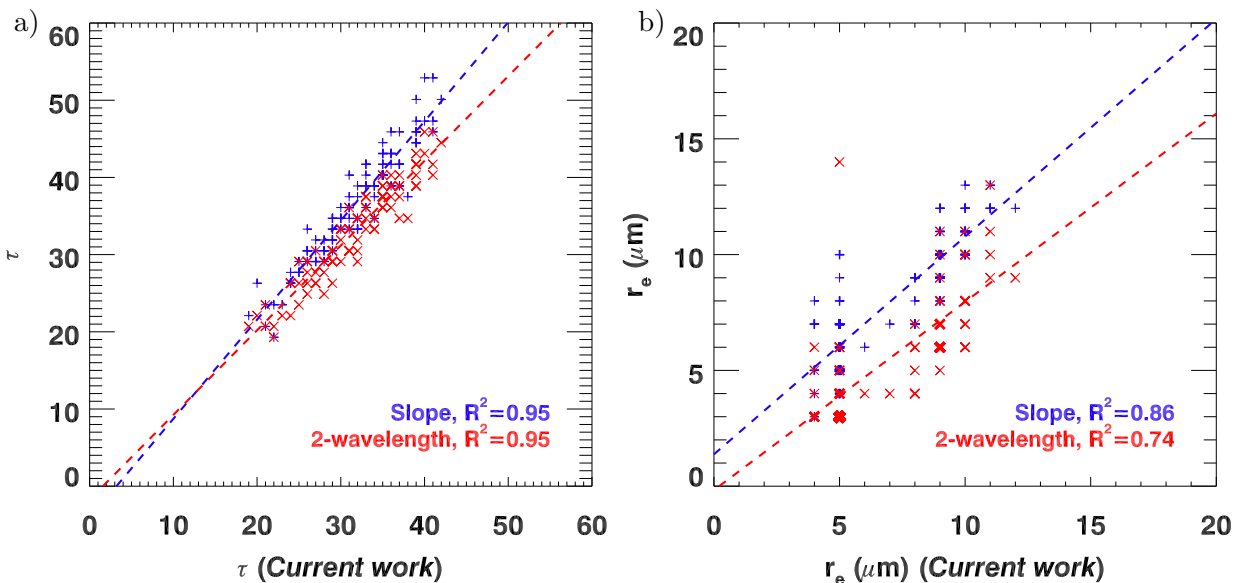


Figure 3.12: Scatter plot of (a) optical thickness and (b) effective radius for the liquid water cloud (case A) from the slope (blue) and 2-wavelength (red) methods compared to the current works retrieval. Dashed lines represent the best-fit lines. Larger thickness of the symbols indicates higher density of the points at that location.

All 3 retrievals for case A exhibit a high degree of correlation. The linear correlation coefficient ( $R^2$ ) between the 15-parameter method and the other methods is 0.95 for  $\tau$ , but lower for  $r_e$  (see Fig. 3.12). The  $\tau$  retrieved with the slope and 2-wavelength methods are consistently higher than the 15-parameter  $\tau$ . The difference between the 15-parameter method and the two other methods increases linearly with increasing  $\tau$  by a ratio of 1.28 and 1.10 for the slope and 2-wavelength methods, respectively (Fig. 3.12a). For  $r_e$  (Fig. 3.12b), the 2-wavelength method retrieves lower  $r_e$  than the 15-parameter method by a ratio of 0.81; the slope method does not have such a low bias with respect to  $r_e$  retrieved by the current method. A greater correlation between  $\tau$  than  $r_e$ , retrieved with the different methods, was also observed by *McBride et al.* [2011] for the 2-wavelength and slope retrievals.

For this liquid cloud case, factors contributing to differences in retrieved  $r_e$  values include varying effects of vertical profiles in  $r_e$  evaluated at different wavelengths [Platnick, 2000], horizontal cloud inhomogeneities [e.g., Iwabuchi and Hayasaka, 2002; Marshak et al., 2006], and undetected presence of ice crystals [Sun and Shine, 1994]. Although transmitted radiation interacts with cloud particles throughout the vertical extent of a cloud, this interaction is not the same for radiance at all wavelengths. Platnick [2000] shows that cloud particles in the lowest part of the cloud have a greater influence on transmittance for wavelength at 3700 nm than at 2200 nm, and even less influence on transmittance at 1600 nm. Those cloud particles are responsible for changes in transmitted irradiance of up to 6% at those wavelengths. This would suggest that cloud retrievals based on transmittance at shorter wavelengths would be less dependent on absorption and scattering by cloud particles in the lowest part of the cloud than transmittance at longer wavelengths. Although the influence of the cloud particles near cloud base on the different parameters has not been determined, one would expect that the parameters based on mean normalized radiance at wavelengths shorter than 1600 nm would be less influenced by particles at cloud base than the 2-wavelength method. For liquid clouds, the smallest cloud particles are often located near base [e.g., Zhang et al., 2011]; therefore, the 15-parameter method would retrieve larger  $r_e$  than the 2-wavelength method. For case A, the 15-parameter method retrieved larger  $r_e$  than the 2-wavelength method for 81% of the times, which could in part be due to the spectral dependence of vertical distribution of cloud particle size on transmitted radiance. In addition, Kikuchi et al. [2006], showed that clouds with vertically varying particle size can change the retrieved  $\tau$  by up to 2%.

Cloud inhomogeneities may also affect the 3 retrieval methods in different ways. For case A, the time period selected for analysis reduced, but did not entirely eliminate, horizontal cloud inhomogeneities. For example,  $\tau$  varied between 25 and 43 within 15 minutes around 15.4 UTC (Fig. 3.11). Cloud inhomogeneity has caused overestimations of cloud particle size for reflectance based retrieval due to shadowing [Marshak et al., 2006]. Shadowing may also cause an overestimate of cloud particle size for transmitted radiance based retrievals. Lastly, The presence of ice crystals may have been a cause of differences between the slope and 2-wavelength methods in the work

described by *McBride et al.* [2011]. However, it is unlikely the cause of differences in this case. Ice crystal spectral absorption and scattering features are quantified with  $\eta_1$ ,  $\eta_2$ ,  $\eta_9$ ,  $\eta_{10}$ , and  $\eta_{13}$ . If such features were observed, the cloud was identified as an ice cloud.

### Modeled and measured radiance spectra comparison

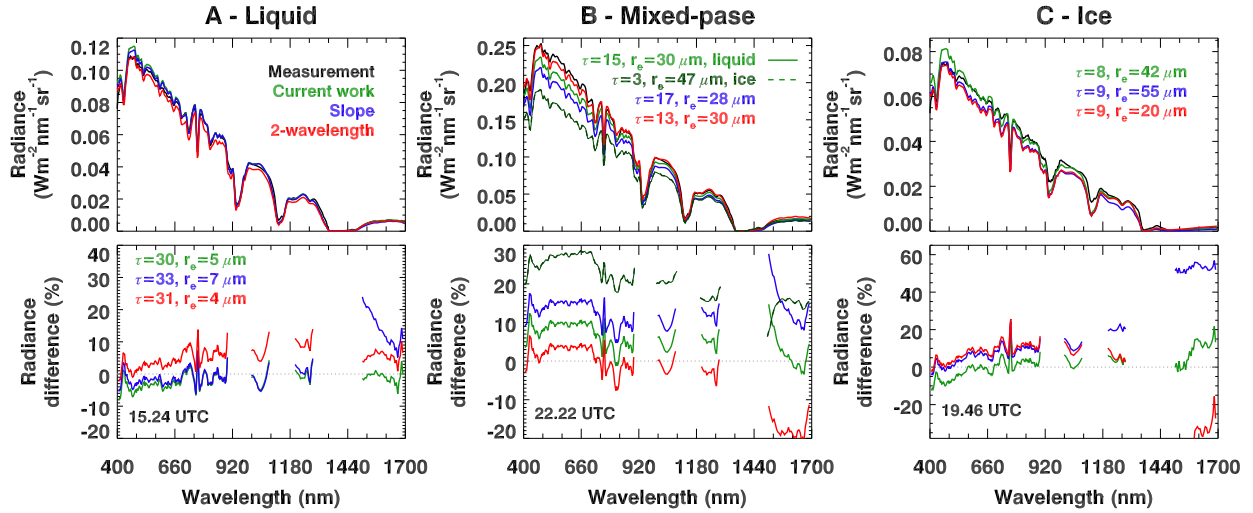


Figure 3.13: Sample measured and modeled spectra for the 3 different cloud case studies. Measured radiance spectra (black) are specific to a certain point (see legend) in the time series of Fig. 3.11. Modeled radiance spectra, are based on the retrieved cloud properties from each method (this work = green; slope = blue, and 2-wavelength = red) for the same time instance. The percentage difference in the modeled spectra with respect to the measured spectra is shown in lower panels for wavelength regions outside of water vapor absorption bands. Modeled radiance spectra based on the current works retrieval for an ice cloud (dashed line) and if it were a liquid cloud (solid line) is presented in case B. The slope and 2-wavelength modeled spectra represent a liquid cloud in case B.

More insight into the differences between the three retrievals is gained when selecting a single sample measurement for further analysis. We compare a representative measurement spectrum to modeled spectra derived from the retrieved  $\tau$  and  $r_e$  values from all three methods in Fig. 3.13. For all 3 cases, the root-mean-square (rms; see Table 3.2) difference throughout the entire wavelength range of the modeled radiance spectra based on the 15-parameter method and the measured radiance spectra are less than the other two methods by up to a factor of 3.8 smaller. However, radiances at the shortest wavelengths ( $<1000$  nm) modeled using the slope method matched the

Table 3.2: Root-mean-square (rms) of the percent difference for the entire wavelength range between modeled spectra based on the 3 different retrievals and the 3 sample measured spectra presented in Fig. 3.13.

	<b>Current Work (%)</b>	<b>Slope (%)</b>	<b>2-wavelength (%)</b>
Case A	3.1	6.4	5.9
Case B	7.2 (22.8 for ice)	13.3	7.3
Case C	5.9	22.5	20.2

measured spectra more closely than the 15-parameter method for the liquid cloud case (rms of 2.4% vs. 3.4%) but not for the ice cloud case (rms of 7.7% vs. 4.9%).

For case A (Fig. 3.13), the fit of all modeled radiance spectra to the measured spectra is better than 24%, resulting in rms values smaller than 6.4%, with the largest variation from the measured spectra occurring at the longest wavelengths ( $> 1000$  nm). At wavelengths shorter than 1000 nm, the modeled spectra based on all three retrievals matches the measured spectrum within 12%. At 1500 nm, the radiance difference for the modeled radiance spectra based on the slope retrieval diverges by 24%. By contrast, the difference between measured and modeled radiance spectrum based on  $\tau$  and  $r_e$  retrieved using the 15-parameter method is better than 7% at wavelengths longer than 1000 nm outside gas absorption bands and better than 8% at all wavelengths resulting in a rms of at least 2.8% lower than the other two methods. The better fit is expected for the 15-parameter method since the 15 parameters quantify spectral features located at wavelengths spanning the entire range.

The sample measured spectrum for case B was selected to coincide at the transition between ice and liquid cloud, where both ice and liquid cloud particles influence the transmitted radiance spectrum. The retrieval described herein classified the cloud as liquid because the normalized radiance magnitudes indicated that the cloud was composed of liquid cloud droplets, although some ice particle absorption features are still apparent in the measured spectrum at wavelengths longer than 1000 nm. One ice absorption feature is the monotonically decreasing radiance between 1000 -1100 nm, which is quantified by  $\eta_1$  and  $\eta_9$ . Conversely, liquid cloud droplets produce a local maximum in radiance at 1050 nm. We observed this maximum in the modeled radiance spectra

based on the slope, 2-wavelength, and the 15-parameter method (solid lines in Fig. 3.13). The ice absorption feature found in the measured radiance spectrum is reproduced in the dark green dashed line in Fig. 3.13, where there is no maximum at 1050 nm. Between 1500 - 1700 nm, the modeled ice cloud spectrum matches measurement more closely (within 16%) than modeled liquid cloud spectrum based on the slope and 2-wavelength method (up to 28% difference), even though the smallest rms for the entire wavelength range (7.2%) is obtained for the liquid cloud spectrum modeled from the 15-parameter method.

For case C (Fig. 3.13), the modeled radiance based on the 15-parameter method reproduced the measurement at wavelengths  $> 1000$  nm more accurately than the modeled radiance based on the other two methods, similarly to case A. The modeled radiances based on the 2-wavelength and slope method match nearly identically the measured radiance at 515 nm, but diverge by up to 55% at wavelengths  $> 1000$  nm. The poor fit of modeled radiance based on these 2 methods to measured radiance at longer wavelengths is likely due to the low signal to noise ratio of radiance at wavelengths near 1600 nm, where ice absorption is largest. The best fit to the measured spectrum throughout the entire wavelength range is obtained by the modeled radiance spectrum based on the 15-parameter described in this work, with an rms of 5.9%, which is 3.8 (3.4) times smaller than the rms from the slope (2-wavelength) method. This is expected since only 4 of the 15 spectral parameters rely on radiance with low signal to noise ratio, whereas half of the information for the slope and 2-wavelength method rely on radiances at those wavelengths.

### 3.6 Summary and Conclusions

This work introduces 15 new parameters quantifying unique absorption and scattering properties of ice and liquid water cloud particles and their first application to measured cloud radiance spectra to retrieve  $\tau$ ,  $r_e$ , and  $\phi$ . The 15 parameters generalize cloud retrieval techniques based on spectral radiance transmitted through clouds and were inspired by the spectral feature quantified by *McBride et al.* [2011]. These parameters are derived from transmitted spectral radiance measurements which have been normalized by their maximum value or by the radiance value at 1000

nm. By doing this, we no longer rely on the absolute radiometric calibration, which varies up to 8%. Rather, we rely on the much higher wavelength-to-wavelength stability of the SSFR (4.6% or 1.1%). The measurements of spectral radiance were made by the SSFR based at the Skywatch observatory in Boulder, Colorado, for 3 time periods encompassing clouds of different thermodynamic phase: liquid (case A), mixed-phase (case B), and ice (case C). We retrieve  $\tau$ ,  $r_e$ , and  $\phi$  by evaluating the weighted least-squares best fit between the parameters calculated from measured transmittance and precomputed tables of parameters derived from simulated cloud radiance. The new parameters are shown to distinguish cloud thermodynamic phase. This discrimination uses spectral absorption and scattering features unique to either ice or liquid water cloud particles. Thermodynamic phase discrimination for 3 cloud cases correctly reproduced the classification of the thermodynamic phase by ancillary data.

Five of the parameters,  $\eta_1$ ,  $\eta_2$ ,  $\eta_9$ ,  $\eta_{10}$ , and  $\eta_{13}$ , give distinct values when either ice or liquid cloud particles are present. This sensitivity to thermodynamic phase is obtained by capitalizing on spectral differences in the absorption properties of ice and liquid cloud particles. Some of these parameters,  $\eta_9$  and  $\eta_{10}$  for example, are defined over spectral ranges where the position of the local maximum and minimum of transmittance differs for ice or liquid clouds. In those wavelength ranges, the transmittance for ice or liquid water clouds exhibit either a concave or convex shape, where the spectral slope increases or decreases, respectively, as wavelength increases.

The 15 parameters quantify specific spectral features found in normalized radiance. The normalization amplifies the spectral features of interest and allows for a more direct comparison of radiance spectra transmitted through different cloud, but removes the first-order dependence on  $\tau$ . After normalization, the parameters still show dependence on  $\tau$ ,  $r_e$ , and  $\phi$ . Of these 15 parameters, we have found that  $\eta_1$ ,  $\eta_2$ ,  $\eta_3$ ,  $\eta_6$ ,  $\eta_8$ ,  $\eta_9$ ,  $\eta_{10}$ ,  $\eta_{11}$  and  $\eta_{15}$  ( $C_{1.0}$ ,  $\partial/\partial\lambda_{1.2}$ ,  $\partial/\partial\lambda_{1.5}$ ,  $\langle R \rangle_{1.6}$ ,  $C_{1.6}$ ,  $\partial^2/\partial\lambda_{1.0}^2$ ,  $\partial^2/\partial\lambda_{1.2}^2$ ,  $sl_{0.55}$ , and  $sl_{1.6}$ ) show the largest sensitivity to  $\tau$ ,  $r_e$ , and  $\phi$ .

We compare  $\tau$  and  $r_e$  from 3 different retrievals: the 15-parameter retrieval described in this work, the spectral slope method described by *McBride et al.* [2011], and the 2-wavelength method, which is typically used with reflectance [*Nakajima and King*, 1990] but applied to transmittance

[*Kikuchi et al.*, 2006]. For the liquid cloud case, the  $\tau$  retrieved with the 3 different methods correlated well ( $R^2 = 0.95$ ) and matched within 10, whereas,  $r_e$  retrieved with the 3 methods did not match as well and correlated less (as low as  $R^2 = 0.74$ ). One possible reason for the differences in retrieved  $r_e$  values can be attributed to the varying influence of cloud droplet vertical profile on radiance at different wavelength regions [*Platnick*, 2000].

We compared measured transmitted radiance spectra to modeled transmitted radiance spectra based on the retrieved  $\tau$ ,  $r_e$ , and  $\phi$ . We find root-mean-square differences between modeled and measured radiance spectra are less when using the results from the 15-parameter retrieval (3.1%) than the slope and 2-wavelength method, by up to a factor of 3.8 for the ice cloud case. By contrast, differences in radiances approach 6.4% for the liquid case and 22.5% for the ice cloud case evaluated over the same wavelength range for modeled radiances based on slope and 2-wavelength retrieval. At the shortest wavelengths (less than 1000 nm), the slope method outperform this works method for liquid clouds, but not for ice clouds in terms of match to the measured spectra.

The use of spectral information in this work showcases the advantages of using a spectrometer system for remote sensing of clouds. Increased understanding of cloud properties can be gained using photons that have interacted with cloud particles throughout the entire cloud vertical extent. The basis of this method could also be applied to spectral reflectance measurements from satellites. Some of the spectral features investigate here may translate directly to reflectance, especially those based entirely on absorption properties of liquid and ice cloud particles. In the following chapter, we will formally quantify uncertainties in the retrieved cloud properties from this new method and the information content of each parameter, by investigating the impact of varying ancillary inputs on the retrieval scheme. This will be done using a nonlinear methodology [*Vukicevic et al.*, 2010] that will investigate the changes of the retrieved properties over the full range of optical thickness and effective radius that results from uncertainties in the measurement and forward model inputs.

### 3.7 Acknowledgements

This work was partially supported from grant NNX11AK67G (remote sensing theory), entitled 'development and validation of new spectral cloud and aerosol retrievals. We thank Warren Gore from NASA Ames for the use of the SSFR instrument. The MODIS MCD43B3 surface albedo data were obtained through the online Data Pool at the NASA Land Processes Distributed Active Archive Center (LP DAAC), USGS/Earth Resources Observation and Science (EROS) Center, Sioux Falls, South Dakota ([https://lpdaac.usgs.gov/get\\_data/](https://lpdaac.usgs.gov/get_data/)).

## Chapter 4

### Statistical evaluation of parameters used to discriminate cloud thermodynamic phase and retrieve optical thickness and effective radius from transmitted shortwave radiance spectra

This work quantifies the accuracy and precision of cloud optical thickness ( $\tau$ ), effective radius ( $r_e$ ) and thermodynamic phase ( $\phi$ ) retrieved with a new method based on shortwave transmittance spectra. The technique [*LeBlanc et al.*, 2014, Chap. 3] is based on a set of 15 parameters that quantify spectral features in normalized transmitted spectral radiance through clouds. The retrieval performance is evaluated using the GEneralized Nonlinear Retrieval Analysis (GENRA) method with realistic measurement and model error characteristics. The normalized Shannon information content for liquid water clouds was greater on average (0.87) than for ice clouds (0.75); in addition, uncertainty in effective radius and optical thickness was smaller for liquid water clouds. The greatest information content occurred for the clouds with  $\tau < 20$  for both thermodynamic phases. A reduction in Shannon information content of no more than 0.02 for 3 cloud cases studied occurred when only 10 of the 15 parameters were implemented in the retrieval. By using simulated radiance spectra within GENRA, we have determined that the *LeBlanc et al.* [2014] method is unbiased for all clouds, except for ice clouds with optical thickness greater than 25 and effective radius larger than 30  $\mu\text{m}$ . We have also found that the thermodynamic phase is accurately determined for all clouds with a probability greater than 99.4%. When we assume that the cloud particle size varies proportionally to the vertical height within cloud, the mean bias in retrieved  $\tau$  is higher than truth by 3.3% for liquid water cloud and lower than truth by 3.3% for ice clouds. The retrieved  $r_e$  is

biased low for liquid water clouds by an average of -12% and biased high in ice clouds by an average of +2.3%.

## 4.1 Introduction

The shortwave radiation at Earth’s surface (between 300 nm and 4000 nm) is affected by clouds more than by any other atmospheric constituent. As such, there have been substantial efforts to define cloud optical and microphysical properties that govern the modulation of shortwave radiation by clouds [e.g., *Ehrlich et al.*, 2008; *Kikuchi et al.*, 2006; *Kindel et al.*, 2010; *LeBlanc et al.*, 2014; *McBride et al.*, 2011; *Nakajima and King*, 1990; *Platnick et al.*, 2001; *Twomey and Cocks*, 1989]. Cloud optical and microphysical properties include cloud optical thickness ( $\tau$ ), cloud particle effective radius ( $r_e$ ), and cloud thermodynamic phase ( $\phi$ ). Higher accuracy in the retrieval of these properties are necessary to reduce uncertainty in cloud radiative forcing and feedbacks.

$\tau$ ,  $r_e$ , and  $\phi$  are routinely retrieved using passive remote sensing techniques based on measuring cloud reflectance at differing wavelengths [e.g., *Baum et al.*, 2000; *Meyer and Platnick*, 2010; *Nakajima and King*, 1990; *Platnick et al.*, 2003; *Twomey and Cocks*, 1989]. However, these remote sensing techniques are inherently influenced more by the cloud particles near cloud top than cloud particles below cloud top. While they are sufficient for deriving the top-of-atmosphere radiative budget and forcing, they are less satisfactory for deriving radiative quantities at the surface since they will be influenced by the entire cloud column. To minimize this bias, the use of transmitted radiance for remote sensing of cloud properties is advantageous because transmitted radiation has interacted with cloud particles throughout the vertical extent of the cloud [*Platnick*, 2000].

Uncertainties in retrieved  $r_e$  from, for example, the reflectance based method of *Nakajima and King* [1990], are large when applied to transmittance [e.g., *Turner et al.*, 2007]. Therefore, retrieving  $\tau$  and  $r_e$  from ground based passive measurements has been difficult. Uncertainties in retrieved  $r_e$  occur in part because a single radiance measurement below cloud can be associated to more than one value of  $\tau$ . In addition, radiances evaluated at wavelengths typically used for determining  $r_e$  asymptotes to zero for large optical thickness ( $> 100$ ), which reduces the signal

to noise ratio. Recent improvements in retrieval techniques applied to ground based measurements of spectral radiance reduced uncertainties in  $r_e$  [LeBlanc *et al.*, 2014; McBride *et al.*, 2011]. The retrieval described by McBride *et al.* [2011] relied on transmitted radiance at a mid-visible wavelength and the slope of transmittance between 1565-1637 nm. LeBlanc *et al.* [2014] derived a generalized retrieval of  $\tau$ ,  $r_e$ , and  $\phi$  from cloud transmittance based on spectral features throughout the shortwave wavelength range.

The spectral features in cloud transmittance spectra exhibiting highest sensitivity to  $\tau$ ,  $r_e$ , and  $\phi$  were defined by the spectral slope, first and second derivatives, curvature, mean normalized radiance, and ratio of radiance at two wavelengths [LeBlanc *et al.*, 2014, Chap. 3] and were used to construct 15 parameters for the retrieval. The parameters take advantage of the changes in absorption and scattering properties of ice and liquid water cloud particles. These variations in absorption properties have also been used to determine cloud thermodynamic phase in reflectance [Pilewskie and Twomey, 1987]. LeBlanc *et al.* [2014] presented the dependence of each of the 15 parameters on  $\tau$ ,  $r_e$ , and  $\phi$ . The parameters serve as the basis to discriminate  $\phi$  and retrieve  $\tau$  and  $r_e$  by matching modeled parameters to the parameters calculated from a measured radiance spectrum via a weighted least squares fit. The uncertainties in retrieved  $\tau$  and  $r_e$  were linked to uncertainties in the measured radiance spectrum and were shown to be  $\pm 0.7$  and  $\pm 1.2 \mu\text{m}$  for an ice cloud.

The uncertainties of  $\tau$ ,  $r_e$ , and  $\phi$  are not only impacted by measurement uncertainties but also by uncertainty in atmospheric and surface conditions that are required in the forward radiative transfer model. To minimize the impact of these uncertainties, the modeled transmitted radiance spectra used the following observed and assumed atmospheric and surface conditions for each day of the 3 cloud cases presented by LeBlanc *et al.* [2014]: surface albedo, cloud height and extent, atmospheric profile of temperature, pressure, water vapor, number concentration of trace gases, and the vertical profile of cloud particle size. Although great care was taken to match these ancillary properties, it is highly likely that differences between the best fit modeled radiance spectra and the measured radiance spectra were, in part, due to the uncertainty in ancillary properties.

In the present work, we quantify the uncertainties in retrieved  $\tau$  and  $r_e$  as a function of cloud phase, the error of which is also quantified, when the model uncertainties are explicitly taken into account. The uncertainty of this retrieval is characterized by the use of the Generalized Nonlinear Retrieval Analysis [GENRA; *Vukicevic et al.*, 2010]. GENRA implements general inverse theory techniques [*Mosegaard and Tarantola*, 2002; *Tarantola*, 2005; *Vukicevic and Posselt*, 2008] to find the most likely combination of  $\tau$ ,  $r_e$ , and  $\phi$  that reproduces the observations. To produce realistic uncertainties of  $\tau$  and  $r_e$ , and to quantify the probability of accurate thermodynamic phase discrimination, we use realistic measurement error statistics in addition to variations of the surface albedo, cloud base height, and precipitable water typically encountered in a 12 hour period. The biases linked to differences in vertical profiles of  $r_e$  are also evaluated within the GENRA framework by applying the retrieval to modeled cloud spectral transmittance with vertically varying  $r_e$ . Moreover, the Shannon information content [SIC; *Shannon and Weaver*, 1949] is used to quantify information content. SIC is used to evaluate the information content gained with the addition of each parameter to the most likely combination of  $\tau$ ,  $r_e$ , and  $\phi$ . That is, the formal Shannon information content is used to determine which parameters are most responsible for the precision of the retrieved  $\tau$ ,  $r_e$ , and  $\phi$ . A similar analysis, which employs GENRA and SIC to obtain accuracy and precision of the method described by *McBride et al.* [2011] is described by *Coddington et al.* [2013].

This paper is organized into 6 sections. Section 4.2 introduces the radiative transfer model used in this study. Each variation in the radiative transfer model input and the resulting changes to the parameters are presented in Sect. 4.3. Section 4.4 details the retrieval methodology and the GENRA tool used for evaluating the accuracy and precision of the retrieval. Section 4.5 describes an analysis of the SIC and uncertainties of the retrieval when applied to modeled radiances. The findings are summarized in Sect. 4.6.

## 4.2 Simulation of zenith radiance spectra

A radiative transfer model is used to quantify the variability in cloud-transmitted spectral radiance for any combination of  $\tau$ ,  $r_e$ , and  $\phi$ . The same radiative transfer model presented by *LeBlanc et al.* [2014] is used here to simulate the measurements of zenith radiance spectra. These measurements were collected by the Solar Spectral Flux Radiometer [SSFR, *Pilewskie et al.*, 2003]. The SSFR typically measured upwelling and downwelling spectral irradiance onboard airborne research platforms [e.g., *LeBlanc et al.*, 2012, Chap. 2], but was modified for ground based operations to measure downwelling irradiance and zenith spectral radiance in the wavelength range between 350 nm – 1750 nm. The SSFR was located at the Skywatch observatory (<http://skywatch.colorado.edu>) in Boulder, Colorado. The SSFR slit function was used as input to the radiative transfer model to simulate the radiance measurements. The measurement accuracy and precision of the SSFR [*LeBlanc et al.*, 2014] are used to define measurement uncertainty within GENRA.

### 4.2.1 Radiative transfer model

The radiative transfer model used by *LeBlanc et al.* [2014] included the N-stream DISORT 2.0 [*Stamnes et al.*, 2000] with SBDART [*Ricchiazzi et al.*, 1998] for atmospheric molecular absorption; these are publicly available in LibRadtran [*Mayer and Kylling*, 2005]. Details of the representation of liquid water droplets and ice cloud particles in the model are presented by *LeBlanc et al.* [2014]. This model was used to simulate spectral transmittance for liquid and ice clouds with  $\tau$  varying between 1 and 100 with a resolution of 1. Liquid water clouds were modeled with  $r_e$  varying from 1  $\mu\text{m}$  to 30  $\mu\text{m}$  and ice clouds with  $r_e$  varying from 10  $\mu\text{m}$  to 60  $\mu\text{m}$ , both with a resolution of 1  $\mu\text{m}$ . This grid of solutions linking simulated measurements to a broad range in cloud properties is commonly referred to as a look-up table (LUT).

### 4.2.2 Ancillary inputs – base case

The model ancillary inputs of surface albedo, cloud height and extent, atmospheric state, and vertical profile of cloud drop sizes represent conditions encountered at Boulder, Colorado, during spring/summer 2012. A "base case" of ancillary inputs is defined as the mid-point (or baseline) in the encountered range of variability in the ancillary inputs. The variability in the ancillary inputs were measured during the period from May 2012 to September 2012, and was described by *LeBlanc et al.* [2014] as the spring/summer period, where the spectral albedo of a vegetated surface is present.

The spring/summer baseline conditions were defined for 25 May 2012 and consisted of a surface albedo scaled to match a 16-day average surface albedo observations centered on 24 May 2012. We assumed that the clouds extended from 1.5 km to 3 km above the surface (located at 1.66 km above sea level) with a constant  $r_e$  throughout the vertical extent of the cloud. The atmospheric profiles of number concentration of trace gases, pressure, temperature, and water vapor used in the baseline condition were calculated from the sounding taken at Denver airport at 12 UTC on 25 May 2012, with a precipitable water of 9.2 mm, representing the depth of the water column if all the water vapor in the atmosphere were precipitated as rain.

### 4.2.3 Modeled radiance spectra and parameters

Examples of 3 modeled cloud-transmitted radiance spectra, which will be used throughout this paper as case studies, are presented in Fig. 4.1. These 3 radiance spectra are linked to cloud properties ( $\tau$ ,  $r_e$ , and  $\phi$ ) typical of those retrieved from measurements taken during the 3 cloud cases, presented by *LeBlanc et al.* [2014]. The cases characterized: (A) liquid water cloud, (B) mixed phase cloud, and (C) ice cloud. In this study, we used  $\tau = 40$  and  $r_e = 7 \mu\text{m}$  to represent the average values retrieved for the start of cloud case A,  $\tau = 20$  and  $r_e = 50 \mu\text{m}$  for cloud case B, and  $\tau = 5$  and  $r_e = 25 \mu\text{m}$  for cloud case C. This work does not explicitly model mixed phase cloud, therefore, cloud case B is represented by a cloud containing ice particles, which was retrieved at

the start of this case [LeBlanc *et al.*, 2014].

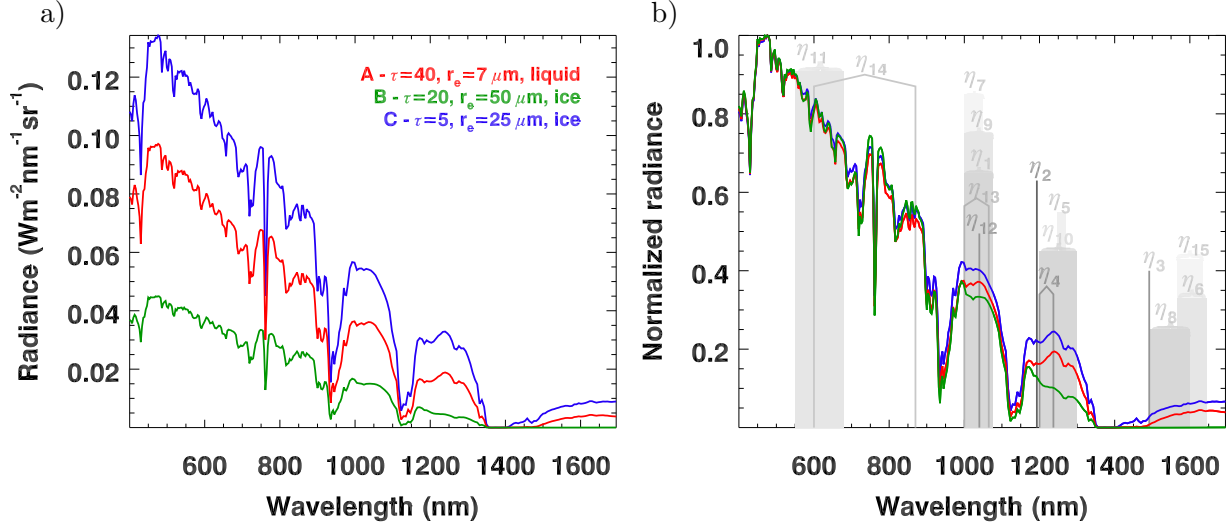


Figure 4.1: Sample modeled (a) radiance ( $Wm^{-2}nm^{-1}sr^{-1}$ ) spectra and (b) normalized radiance (unitless) transmitted through clouds with 3 combinations of  $\tau$ ,  $r_e$ , and  $\phi$  (cases A, B, and C) and a solar zenith angle of  $50^\circ$ . The grey shaded regions represent the spectral bands used in determining the different parameters, introduced by LeBlanc *et al.* [2014],  $\eta_1$ ,  $\eta_5$  to  $\eta_{11}$ , and  $\eta_{15}$ . Grey vertical lines indicate the wavelength for parameters,  $\eta_2$  to  $\eta_4$  and  $\eta_{12}$  to  $\eta_{14}$ , which are evaluated at a single wavelength.

The magnitude of spectral radiance is most sensitive to  $\tau$ , and to a lesser extent,  $r_e$ , and  $\phi$ . By normalizing a spectrum by its maximum radiance, which is found between 451 nm and 490 nm, the broad range in magnitude due to  $\tau$  is eliminated (compare Fig. 4.1a to Fig. 4.1b). Particularly in the near-infrared (NIR; wavelengths longer than 700 nm), the spectrally dependent differences, or spectral features, of normalized radiance such as curvatures, minima or maxima, and changes in slope are amplified. The wavelengths or wavelength bands with the largest variations of spectral features that depend on  $\tau$ ,  $r_e$ , and  $\phi$  are indicated by the shaded regions in Fig. 4.1b. Each shaded region also indicates the wavelengths or spectral bands that are used to derive the parameters, denoted by  $\eta_1$  through  $\eta_{15}$  [see LeBlanc *et al.*, 2014]. In addition, when using the maximum-normalized radiance, there is reduction in measurement uncertainty and in variability associated with changes of solar zenith angles as high as  $80^\circ$ . A summary of the methods used to derive the 15 parameters and shorthand symbolism is presented in Table 4.1. The wavelength

region where each parameter is defined is also included.

Table 4.1: Method, shorthand symbolism, and wavelength region for each 15 parameters introduced by *LeBlanc et al.* [2014]

	Wavelength(s) (nm)	Shorthand symbolism	Method
$\eta_1$	1000-1100	$C_{1.0}$	Curvature
$\eta_2$	1200	$\partial/\partial\lambda_{1.2}$	Derivative
$\eta_3$	1500	$\partial/\partial\lambda_{1.5}$	Derivative
$\eta_4$	1200 & 1237	$r_{1.2}$	Ratio
$\eta_5$	1245-1270	$\langle R \rangle_{1.25}$	Mean
$\eta_6$	1565-1640	$\langle R \rangle_{1.6}$	Mean
$\eta_7$	1000-1050	$\langle R \rangle_{1.0}$	Mean
$\eta_8$	1490-1600	$C_{1.6}$	Curvature
$\eta_9$	1000-1080	$\partial^2/\partial\lambda_{1.0}^2$	Slope of derivative
$\eta_{10}$	1200-1310	$\partial^2/\partial\lambda_{1.2}^2$	Slope of derivative
$\eta_{11}$	530-610	$sl_{0.55}$	Slope
$\eta_{12}$	1040	$R_{1.04}$	Normalized radiance
$\eta_{13}$	1000 & 1065	$r_{1.0}$	Ratio
$\eta_{14}$	600 & 870	$r_{0.6}$	Ratio
$\eta_{15}$	1565-1634	$sl_{1.6}$	Slope

### 4.3 Variation in modeled transmitted radiance spectra and parameters due to ancillary inputs

The accuracy of retrieved cloud properties is sensitive to the ancillary input. Measurement error along with spatial and temporal interpolation errors result in uncertainties when observing these inputs. For operational retrievals, it is impractical to have updated observation for model input; often these data must be assumed. One objective of this paper is to test the sensitivity to uncertainties in the model ancillary input. To quantify this sensitivity, we independently vary each ancillary input datum from the base case and observe the resulting change of the modeled spectra and the parameters derived from them.

### 4.3.1 Variations in cloud base height and extent, surface albedo, and precipitable water

Cloud vertical extent and base altitudes were selected to mimic single layer clouds encountered during the spring/summer measurement period. Cloud base altitudes were retrieved from the Skywatch ceilometer measurements [LeBlanc *et al.*, 2014]. Cloud top altitude was obtained from the Geostationary Operational Environmental Satellite [GOES, Minnis *et al.*, 1995] and from the Moderate Resolution Imaging Spectroradiometer [MODIS, Platnick *et al.*, 2003]. During the measurement period, observed cloud base heights ranged from near ground to higher than the measurement limit of 7.8 km above ground, with a midpoint near 1.5 km. Single layer cloud extent varied less, from a few hundred meters to 3.5 km, with an average of 1.5 km. The model input variability was set to match the observed. We varied cloud base height from 0.5 km to 9 km above ground level at 5 distinct levels above ground: 0.5 km, 1.5 km, 3 km, 5 km, 7 km, and 9 km, with a constant cloud geometrical thickness of 1.5 km. The radiance spectra resulting from changes in the cloud base height are presented in Fig. 4.2a.

The variation in surface albedo during the spring/summer measurement period was determined by the same method described by LeBlanc *et al.* [2014]. In this method, a measured spectral albedo of a vegetated surface [Michalsky *et al.*, 2003] was scaled to match the 16-day average surface albedos from MODIS [Schaaf *et al.*, 2002] centered on 24 May 2012, on 4, 12, 20 August 2012, and on 13 September 2012. The modeled radiance spectra based on the surface albedos evaluated for the different 16 day average time periods are presented in Fig. 4.2b

Atmospheric soundings measured at the Denver airport showed precipitable water ranging from 5 mm to 30 mm during the spring/summer measurement period, with the average at 11 mm. However, precipitable water did not change by more than 8 mm between soundings (representing 12 hours) for the 3 cases introduced by LeBlanc *et al.* [2014]. To vary the model input of precipitable water, we linearly extrapolated the number concentration of water vapor at each layer in the profile to represent a precipitable water of 5 mm to 30 mm in 5 mm increments, while keeping the

atmospheric profile of temperature, pressure, and number concentrations of trace gases to baseline conditions. The resulting modeled radiance spectra and their change to the radiance evaluated with baseline conditions are presented in Fig. 4.2c.

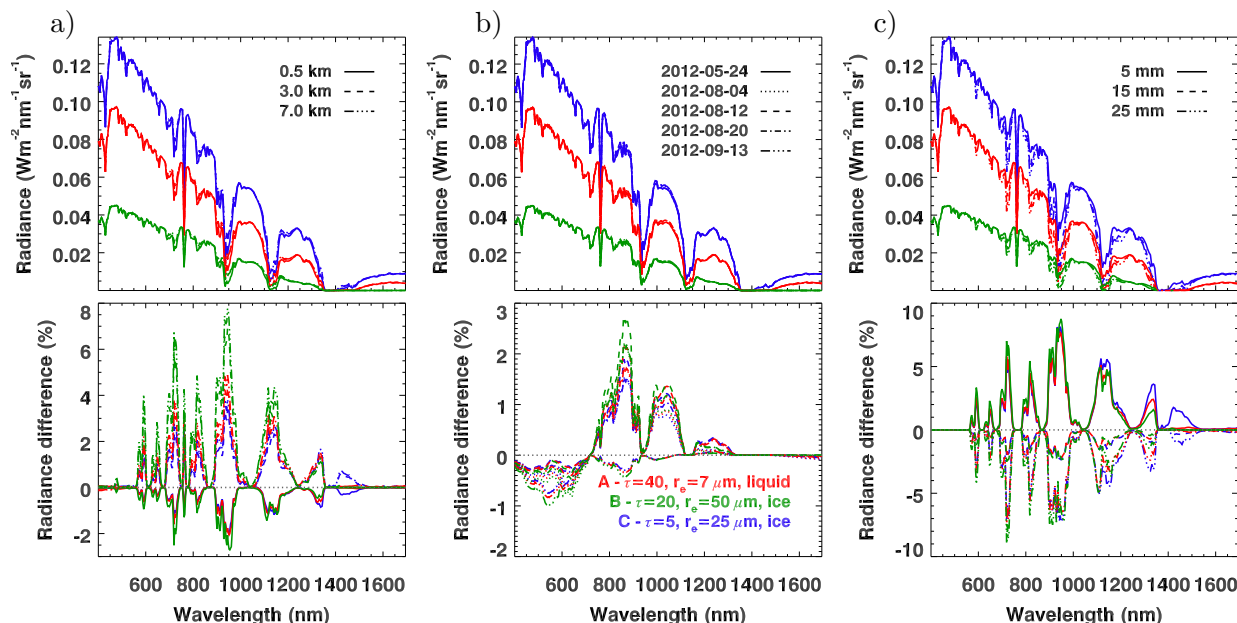


Figure 4.2: Modeled zenith spectra with variance due to (a) cloud base height above ground, (b) surface albedo evaluated for the 5 periods centered on the dates listed, and (c) precipitable water. Top panels show the radiance spectra for the 3 cloud cases (case A - red, case B - green and case C - blue) evaluated with different cloud base height above ground, surface albedo, and precipitable water identified by different line styles. The bottom panels show the difference in radiance spectra as a percentage of the maximum radiance between radiance spectra evaluated with the changing ancillary inputs presented in the top panels and the base case ancillary inputs. The dotted grey line indicates a 0% difference to the radiance evaluated with base case ancillary inputs.

Figure 4.2 shows the modeled radiance spectra for various ancillary inputs (top panels) and the difference of these spectra to the modeled radiance spectra based on the baseline ancillary inputs (bottom panels). Varying cloud base height affects radiances that are within gas absorption bands with the strongest effects within water vapor absorption bands centered at 720 nm, 810 nm, 940 nm, 1150 nm, 1400 nm (Fig. 4.2a). Only the radiance evaluated with a cloud base at 0.5 km was smaller than radiance evaluated with a cloud base at 1.5 km. This behavior is expected since a cloud at higher altitude will scatter photons in an environment that is drier than for lower clouds. Since there is more water vapor at lower altitude, absorption by water vapor is also increased.

When precipitable water is increased to as high as 25 mm, radiance within these gas absorption bands also deviates by 9% of the maximum radiance from modeled spectra with baseline conditions (bottom panel Fig. 4.2c). The changes in surface albedo affect radiances in the wavelength ranges outside gas absorption bands by 2.8% (bottom panel Fig. 4.2b). These same spectral bands are used to define the various retrieval parameters (see Table 4.1). Consequently, it is expected that the parameters are sensitive to changes in surface albedo.

### 4.3.2 Variations in vertical profile of $r_e$

Unlike the previous 3 ancillary inputs, there was no measurement of cloud particle size vertical profile during the measurement period of this study. As a result, variation of the vertical profile of  $r_e$  was not included in the uncertainty calculations of  $\tau$  and  $r_e$  or in the  $\phi$ -discrimination error. However, we simulate vertically varying  $r_e$  in order to test the retrieval accuracy. We present here vertically varying  $r_e$  to match more closely what is found in nature, versus a constant  $r_e$  [e.g., *Miles et al.*, 2000]. We used the parameterization of the vertical profile of  $r_e$  defined by *Chang and Li* [2003], where  $r_e$  is directly proportional to cloud vertical geometrical height ( $r_e \propto z$ ). To define the possible limits of the vertical profile, we set the  $r_e$  at cloud base to half its mean value. At cloud top,  $r_e$  is equivalent to 1.5 times its mean value (see Fig. 4.3a). Similar ranges of  $r_e$  are also observed in large-eddy simulations of shallow convective clouds [e.g., *Zhang et al.*, 2011]. The profile within cloud is evaluated by 10 different cloud layers of a thickness of 0.15 km each. At each layer,  $\tau$  is kept constant, but  $r_e$  varies (Fig. 4.3a). The resulting modeled radiance spectra are presented in Fig. 4.3b, with deviation from radiance spectra modeled with the base case ancillary inputs in Fig. 4.3c. A difference of 4% is found in the midvisible wavelengths for the radiance spectra of cloud case A, which is the optically thickest cloud case. Radiance spectra for the other two cases do not vary by more than 1.5% outside gas absorption bands. Variations in radiance magnitude on the order of less than 2% has also been observed for clouds with  $\tau < 40$  by *Kikuchi et al.* [2006].

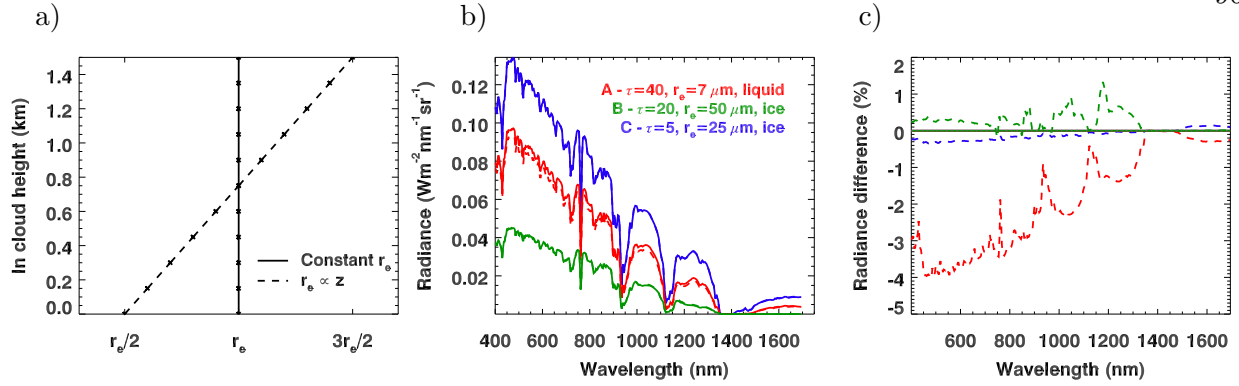


Figure 4.3: (a) Vertical profile of  $r_e$  for a cloud with constant  $r_e$  (solid line) and a cloud with  $r_e$  varying proportionally with cloud height ( $z$ , dashed line). Each 'X' symbol denotes the middle point of the cloud layer. (b) The two profiles of  $r_e$  as model input for the radiance spectra calculated with 3 cloud cases. The spectra modeled from vertically varying  $r_e$  are presented as dashed lines. (c) The differences between radiance spectra evaluated with the two  $r_e$  profiles.

### 4.3.3 Variations in retrieval parameters

To retrieve  $\tau$ ,  $r_e$ , and  $\phi$ , 15 parameters are calculated from the set of modeled radiance spectra. By changing the cloud base height, surface albedo, and precipitable water, changes of as much as 9% are observed in the modeled spectra. The differences in radiance spectra are translated to variability in the 15 retrieval parameters. The variability in each parameter (Fig. 4.4) represents the expected change in parameters during the measurement period due to changes of cloud base height, surface albedo, and precipitable water. The parameters  $\eta_5$ ,  $\eta_6$ ,  $\eta_{13}$ , and  $\eta_{15}$ , did not vary by more than 2% of the base case for all changes presented above and will not be discussed further.

The largest change in parameters is caused by variations in precipitable water. The same parameters that are sensitive to precipitable water are also sensitive to cloud base height, while changes in surface albedo affects other parameters. Cloud base height modified the radiance spectra mostly in the gas absorption bands. This translates to variations of more than 2% of the total range of the parameter for  $\eta_1$ ,  $\eta_2$ ,  $\eta_9$ , and  $\eta_{10}$ . The parameters with the largest variations are  $\eta_1$ ,  $\eta_9$ , and  $\eta_{10}$  for case B. For all cases,  $\eta_{10}$  varies much more than any other parameter because it quantifies the slope of the spectral derivative spanning a wavelength region that is bounded by either side by water vapor absorption bands. In general an increase in cloud base height decreases the value of the

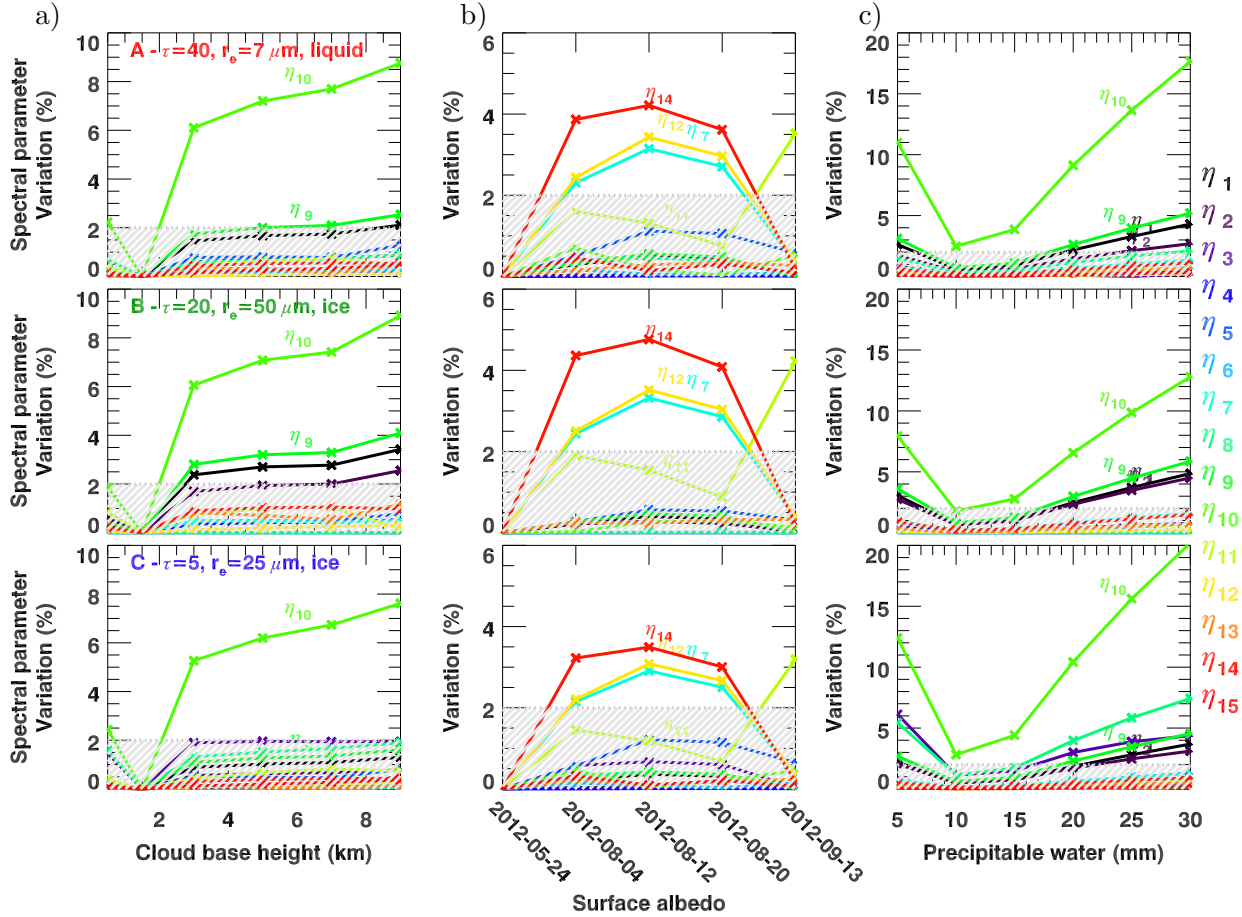


Figure 4.4: Variation in modeled parameters as a percentage of the total range of the parameter evaluated with changes due to (a) cloud base height above ground in the first column, (b) surface albedo evaluated for the 5 periods centered on the dates listed in the second column, and (c) precipitable water in the third column. Each row shows the variation of each parameters,  $\eta_{i=1..15}$ , represented by the colored lines, for the 3 cloud cases (A in the top panel, B in the middle panel, and C in the bottom panel). The shaded part represents variations of less than 2%.

parameters,  $\eta_1$ ,  $\eta_3$ ,  $\eta_8$ ,  $\eta_{11}$ , and  $\eta_{13}$  and increases the value of the other 9 parameters. The change in spectral surface albedo resulted in a change of less than 5% for all parameters.  $\eta_7$ ,  $\eta_{11}$ ,  $\eta_{12}$ , and  $\eta_{14}$  varied by more than 2% from the base case surface albedo defined on 2012-05-24. Although these parameters remained nearly constant with changes in cloud base height (variations of less than 2%), they were the most sensitive to surface albedo. Because surface albedo modifies scattered radiation incident at cloud base, parameters that rely entirely on changes of scattered radiation,  $\eta_{11}$  and  $\eta_{14}$ , were the most influenced by changes in surface albedo. Changes in precipitable water

from 5 to 30 mm result in the largest variation in the parameters, by 20% for  $\eta_{10}$ . The parameters with the variations due to precipitable water greater than 2% are  $\eta_1$ ,  $\eta_2$ ,  $\eta_3$ ,  $\eta_8$ ,  $\eta_9$ , and  $\eta_{10}$ . Of these parameters,  $\eta_1$ ,  $\eta_2$ ,  $\eta_9$ , and  $\eta_{10}$  also varied more than 2% due to changes in cloud base height.  $\eta_9$  is more sensitive to cloud base height than precipitable water, thus  $\eta_9$  is most likely associated with changes of other gas absorption.

Because the most accurate knowledge of ancillary inputs available for each day were used to model the parameters, only the ancillary inputs that varied within each day served as a basis for determining realistic uncertainty in modeled parameters. For cloud base height, only clouds with variations of less than 1 km were used in the retrieval. All parameters, except  $\eta_{10}$ , varied by less than 2% when cloud base height changes by 1 km. Surface albedo changes over each day were expected to contribute the least to the uncertainty of the modeled parameters. Precipitable water did not change by more than 8 mm in between the soundings, resulting in a change of less than 2% for all parameters, except for  $\eta_8$  and  $\eta_{10}$ . For these reasons, we remove  $\eta_8$  and  $\eta_{10}$  from all future analysis. The remaining modeled parameters for all combinations of  $\tau$ ,  $r_e$ , and  $\phi$  vary by an average of 1% due to changes in ancillary inputs expected to occur during the course of a day.

## 4.4 Retrieval evaluation methodology

### 4.4.1 Inverse problem theory

The relationship between the simulated cloud radiance observations,  $f(x; b)$ , described in Section 4.2.1, the cloud properties,  $x$ , and the parameters,  $\eta$ , derived from measured observations of radiation,  $y$ , is expressed by Eq. 4.1. The cloud properties,  $x$ , are defined in the space containing all possible cloud properties,  $\Pi$ , whereas the parameters,  $\eta$ , are defined in the measurement space,  $D$ , containing all possible values of the parameters. The ancillary, or non-retrieved, information (all denoted by  $b$ ) required by the forward model,  $f$ , includes, but is not limited to, the precipitable water, surface albedo, and cloud base height.

$$\boldsymbol{\eta}(y) = f(x; b) + \varepsilon \quad (4.1)$$

$\varepsilon$  represents the uncertainty of the measured value. For retrieving the cloud properties from the radiation measurements, it is necessary to invert this relationship.

The measurements, simulated observations, and cloud properties can be represented stochastically. Instead of single deterministic variables, they are represented by probability density functions (PDFs) and characterized by a mean value and some measure of variance. Quantitative information about the stochastic distribution in the cloud properties and measurements will then be defined by the general inverse problem as expressed in Eq. 4.2 [Mosegaard and Tarantola, 2002; Tarantola, 2005; Vukicevic and Posselt, 2008].

$$p_{\text{joint-post}}(x, \boldsymbol{\eta}(y)) = \frac{1}{\gamma} p_{\text{prior}}(x) p_{\text{meas}}(\boldsymbol{\eta}(y)) p_{\text{model}}(f(x)|x) \quad (4.2)$$

The solution distribution to the general inverse problem, known as the joint-posterior PDF,  $p_{\text{joint-post}}(x, \boldsymbol{\eta}(y))$ , represents the most complete available knowledge in the joint space,  $\Pi \times D$ , connecting cloud properties and the related measurements. This knowledge is derived from the observed parameters,  $p_{\text{meas}}(\boldsymbol{\eta}(y))$ , defined in space  $D$ , any a priori knowledge of the cloud properties,  $p_{\text{prior}}(x)$ , defined in space  $\Pi$ , and the conditional probability density function of the model PDF,  $p_{\text{model}}(f(x)|x)$ , defined in the joint space  $\Pi \times D$ . The model PDF relates simulated measurements to a broad range in cloud properties. Therefore, the uncertainty in the joint-posterior PDF explicitly incorporates model nonlinearity and knowledge of model uncertainties attributed solely to the non-retrieved information of Eq. 4.1, such as those induced by variability in ancillary inputs as discussed in Sect. 4.3. Here,  $\gamma$  represents a normalization coefficient.

#### 4.4.2 Generalized Nonlinear Retrieval Analysis (GENRA)

Vukicevic *et al.* [2010] developed a method known as the GEneralized Nonlinear Retrieval Analysis (GENRA) to characterize the cloud property retrieval solution for realistic error distribu-

tions in the forward modeling and measurements. GENRA employs the look-up tables (LUT) of simulated measurements used in operational retrievals (see Sect. 4.2.1) to build the distributions in the forward modeling. *Vukicevic and Posselt [2008]* have shown that associating a PDF to the model solution in space  $D$  for every value of cloud properties included in space  $\Pi$  forms the model PDF. In GENRA, the LUT plays the critical role of the discrete transfer function between the simulated measurements and the discrete points of the multidimensional  $(\tau, r_e, \text{ and } \phi)$  array of cloud properties [*Vukicevic et al., 2010*].

Ultimately, GENRA is used to compare the solution of the posterior PDF to the 'true' cloud properties defined at the discrete LUT grid points to evaluate the impact of both measurement and modeling errors on the retrieved distribution. Because measurement distributions can be computed using the simulated measurements contained within the LUT and realistic errors, GENRA does not need to perform the retrieval with actual measurements to characterize the retrieval results. The GENRA method has also been applied to characterize cloud properties retrieved from reflected or transmitted radiation [*Coddington et al., 2013; Vukicevic et al., 2010*] and in defining the Shannon Information Content (SIC) in shortwave spectral cloud albedo data [*Coddington et al., 2012*].

The solution distribution, or posterior PDF, in cloud property space,  $\Pi$ , is obtained by integrating the joint-posterior PDF (Eq. 4.2) over the measurement space,  $D$ . The posterior PDF,  $p_{post}$ , returns the solution probability for combinations of cloud properties,  $\tau$ ,  $r_e$ , and  $\phi$ , which represent the generic variable for cloud property,  $x$ . The expanded relationship is presented in Eq. 4.3, with  $\boldsymbol{\eta}$  implicitly including the dependence of the parameter on the measured scattered radiation,  $y$ .

$$p_{post}(\tau, r_e, \phi) = \int_D \frac{1}{\gamma} p_{prior}(\tau, r_e, \phi) p_{meas}(\boldsymbol{\eta}) p_{model}(f(\tau, r_e, \phi)|(\tau, r_e, \phi)) d\boldsymbol{\eta} \quad (4.3)$$

The PDF that describes the uncertainties of  $\boldsymbol{\eta}$  based on the accuracy and precision of the measurement of zenith radiance is denoted by  $p_{meas}(\boldsymbol{\eta})$ . The measurement PDF is interpreted as probability of measurement values over a discrete interval  $(\boldsymbol{\eta}, \boldsymbol{\eta} + \Delta\boldsymbol{\eta})$ , spanning  $D$ . Each parameter,  $\boldsymbol{\eta}_i$

( $i = 1, 2, \dots, 15$ ), is represented by a unique measurement PDF and a unique measurement space  $D_i$ . The model PDFs,  $p_{model}(f(\tau, r_e, \phi)|(\tau, r_e, \phi))$ , represents the probability distribution computed for the  $i$ th-parameter for each combination of cloud properties contained in the LUT. Variations in the simulated zenith radiance due to uncertainty or variability in the ancillary model inputs (Sect. 4.3) are used in defining the error statistics of the model PDF. Similarly, for each cloud property combination, the prior PDF,  $p_{prior}(\tau, r_e, \phi)$ , explains probabilities of the cloud properties over discrete intervals ( $x, x + \Delta x$ ). The discretization of the intervals,  $\Delta\boldsymbol{\eta}$  and  $\Delta x$ , defines the maximum precision in  $D$  and  $\Pi$ .  $\gamma$  is defined such that the integral of the posterior PDF over cloud property space,  $\Pi$  is equal unity. We outline the derivation of these PDFs and the computation of the posterior PDF in Sect. 4.4.3; detailed descriptions can be found in the methodology paper by *Vukicevic et al. [2010]*.

#### 4.4.3 Building the probability density functions

*Defining the measurement space, the cloud property space, and the probability density functions:*

The measurement space,  $D$ , is a 1-D discretized set of all possible values attained by the parameter,  $\boldsymbol{\eta}$ , regularly gridded with constant intervals of  $\Delta\boldsymbol{\eta}$ . The measurement PDF, the joint-posterior PDF, and the model PDF use the same gridding.

The cloud property space,  $\Pi$ , contains evenly-spaced discretized values of  $\tau$ ,  $r_e$ , and  $\phi$  in the same range of values computed for the LUT (see Sect. 4.2.1). To describe the  $\tau$  and  $r_e$  precision for liquid water clouds, for ice clouds, and the  $\phi$ -discrimination accuracy, we define 3 distinct cloud property spaces;  $\Pi_{liq}$  is the set of  $\tau$  and  $r_e$  combinations also defined for the LUT of liquid water clouds,  $\Pi_{ice}$  is the set of  $\tau$  and  $r_e$  combinations also defined for the LUT of ice water clouds, and  $\Pi_{com}$  is the combined set of  $\tau$  and  $r_e$  values for the LUT of both liquid and ice clouds, where  $\Pi_{com} = \Pi_{liq} \cup \Pi_{ice}$ . The total number of points within the 2-D space of  $\Pi_{liq}$  or  $\Pi_{ice}$  is  $N = N_\tau \times N_r$ , where  $N_\tau$  and  $N_r$  are the number of discrete values of  $\tau$  and  $r_e$  included in the respective LUT. The combined space,  $\Pi_{com}$ , is a 3-D space with the number of discrete points  $N = N_\tau \times N_r \times N_\phi$ , with  $N_\phi = 2$  representing the two realizations of cloud thermodynamic phase (ice and liquid).

All 3 cloud property space contain the same  $\tau$ -range, with  $N_\tau = 100$ , but not the same range in  $r_e$ , mimicking naturally occurring values for ice and liquid clouds [e.g., *Baum et al.*, 2011; *Han et al.*, 1994]. The  $\Pi_{com}$  space is defined for  $r_e$  ranging from 1  $\mu\text{m}$  to 60  $\mu\text{m}$  with  $N_r = 60$ , which incorporates the  $\Pi_{liq}$  space containing  $N_r = 30$  liquid water cloud particles with  $r_e$  ranging from 1  $\mu\text{m}$  to 30  $\mu\text{m}$ , and the  $\Pi_{ice}$  space containing  $N_r = 51$  ice cloud particles with  $r_e$  ranging from 10  $\mu\text{m}$  to 60  $\mu\text{m}$ . The total number of discrete points for  $\Pi_{liq}$  is  $N = 3000$ , for  $\Pi_{ice}$  is  $N = 5100$ , and for  $\Pi_{com}$  is  $N = 12000$ . The posterior PDF, model PDF, and prior PDF evaluated in the spaces  $\Pi_{liq}$  and  $\Pi_{ice}$  describe similar information than when evaluated in space  $\Pi_{com}$ , but in space  $\Pi_{com}$ ,  $\phi$  is considered a retrieved property, whereas in space  $\Pi_{liq}$  and  $\Pi_{ice}$  it is a non-retrieved property. Consequently, these PDFs must be evaluated separately for the 3 realizations of the space  $\Pi$  resulting in 3 posterior PDFs used to characterize the retrieval solution. In general terms, the location index within any cloud property space is represented by  $n$ , or by the superscript  $n$ , and represents the doublet ( $\tau$  and  $r_e$ ) in the LUT used to define  $\Pi_{liq}$  and  $\Pi_{ice}$  or the triplet ( $\tau$ ,  $r_e$ , and  $\phi$ ) in the combined space  $\Pi_{com}$  spanning the ice and liquid water cloud LUT.

The probability density functions (PDF) are defined such that the integral of the distribution is equal to unity. In a discretized space, it is the sum of the probability distribution multiplied by the discrete space interval ( $\Delta\boldsymbol{\eta}$  or  $\Delta x$ ) that equals unity, for sufficiently small  $\Delta\boldsymbol{\eta}$  or  $\Delta x$ . Therefore, the PDF can be represented by any positive value starting from 0. When combining PDFs, the PDFs must be defined with the same gridding than for the spaces  $\Pi$  and/or  $D$ .

### 1. Computing the measurement PDF:

The measurement PDF is determined from the errors derived from a set of spectra measured by the SSFR and the spectrum of simulated radiance at index  $n$  of the LUT. To represent realistic error sources of the simulated spectrum the following steps are used:

- a) The set of spectra used to evaluate the spectrum-to-spectrum variation of the SSFR [defined by *LeBlanc et al.*, 2014] has their mean shifted to the value of the simulated spectrum at each wavelength, effectively building a set of simulated spectra with random noise.

- b) The new set of spectra is then evaluated with the variability of 8% of the 3 radiometric calibrations describe by *LeBlanc et al.* [2014], by multiplying the spectra by the ratio of each of the radiometric calibrations to the first. Resulting is a set of radiance spectra 3 times larger than in a), representing non-random error statistics, which are dependent on signal strength (i.e., produce different width of PDFs for each spectrum contained in the LUT)
- c) Each value of  $\eta_i$  is derived per Table 4.1 for all spectra contained in the set described in b). Since all  $\eta_i$  are derived from normalized radiance, the spectrally independent change of the 3 radiometric calibrations is eliminated.
- d) Build a histogram of  $\eta_i$  in the measurement space  $D_i$  and then normalize it such that the integral over  $D_i$  is equal to unity, estimating the measurement PDF.

While measurement error is often assumed to be Gaussian distributed, the propagation of radiometric error into the parameters often resulted in a non-Gaussian, skewed, measurement distribution. This is the result of error statistics that are non-random. The GENRA analysis tool does not require assumptions of normally distributed behavior in the statistics. Figure 5 shows the measurement distributions for  $\eta_2$  for the 3 different cloud cases. The distributions are presented as probability densities, where the PDF least impacted by propagation of errors due to radiometric calibration uncertainty (case A, red line, Fig. 4.5) has a greater value of maximum probably density than the PDF with the largest width, or greatest measurement uncertainty (case B, green line, Fig. 4.5).

## 2. Computing the model PDFs:

The model PDFs, one for each of the 3 cloud property spaces, ( $\Pi_{liq}$ ,  $\Pi_{ice}$ , and  $\Pi_{com}$ ), describe the variance in the  $i^{th}$  parameter values for each  $n^{th}$  element. A total of  $N$  (varies by space), 1-dimensional PDFs describe the model variance through computing the variability in simulated transmittance of the  $n^{th}$  element for uncertainties in the forward model ancillary inputs. For the combined ice and liquid water cloud property space,  $\Pi_{com}$ , where the cloud properties combinations are not expected in nature, which represent ice clouds with  $r_e < 10 \mu\text{m}$  and liquid water clouds

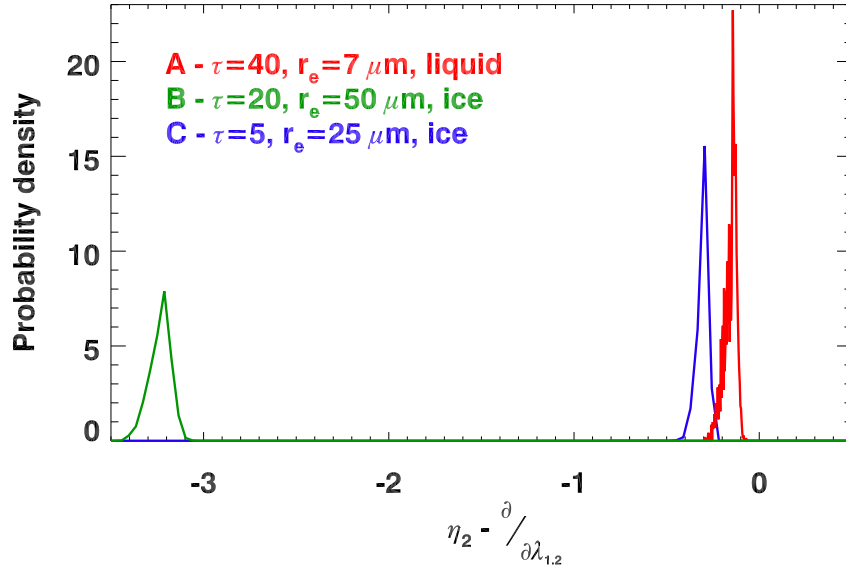


Figure 4.5: Measurement PDF of  $\eta_2$  for the 3 cloud cases.

with  $r_e > 30 \mu\text{m}$ , the 1-D PDFs are set to 0. Although the 1-D model PDF could be calculated at these points, it is unnecessary as the prior PDF for these points will be set to 0. The uncertainties considered arise from the variability in spectral surface albedo, cloud base height, and precipitable water from defined, baseline ancillary model inputs (Sect. 4.3.1).

To build the model PDFs, we first derive PDFs of transmittance at each wavelength with the spectrally-dependent variance described above and using a Monte Carlo sampling procedure (with 20000 points) of an assumed Gaussian distribution. Corresponding samples of the  $i^{\text{th}}$  parameters were computed using the relationships described in Table 4.1. Second, we compute normalized histograms from these samples in the space  $D$ . The resulting PDF in measurement space of  $\eta_i$  is nearly Gaussian (not shown).

### 3. Computing the likelihood function:

For each of the  $N$  discrete grid points in the space  $\Pi_{liq}$ ,  $\Pi_{ice}$ , or  $\Pi_{com}$ , the  $n^{\text{th}}$  model PDF is convolved with the measurement PDF. The likelihood function,  $p_{likelihood}^n$ , of Eq. 4.4 is computed by integrating the convolution of the measurement and model PDFs over the physically possible values of the measurement space that represent the range in parameter values that are

calculated from the radiance spectra contained within the LUT of either ice or liquid water clouds; for example, only positive values of transmittance are physically possible. The integration removes the dependence on the measurement space,  $D$ . Therefore, the likelihood function, consisting of  $N$  solutions, is a function of the cloud property space alone. We created 3 likelihood functions, each defined in a different cloud property space,  $\Pi_{liq}$ ,  $\Pi_{ice}$ , or  $\Pi_{com}$ , for the respective model PDF.

$$P_{likelihood}^n = \int_D p_{meas} p_{model}^n d\boldsymbol{\eta} \quad (4.4)$$

#### 4. Computing the retrieval posterior PDF:

In a final step, the prior PDF containing a priori information of the cloud property space is multiplied with the likelihood function of step 3 for every  $n^{th}$  location index. The resulting posterior PDF is a 2-D or 3-D map of the probabilities for the doublet ( $\tau$  and  $r_e$ ) values of the  $\phi$ -segregated cloud (liquid/ice) property space,  $\Pi_{liq}$  or  $\Pi_{ice}$ , or the triplet ( $\tau$ ,  $r_e$ , and  $\phi$ ) values of the combined property space,  $\Pi_{com}$ .

$$P_{post}^n = \frac{1}{\gamma} p_{prior}^n P_{likelihood}^n \quad (4.5)$$

##### 4a. The treatment of the prior PDF:

The GENRA algorithm introduces each  $\boldsymbol{\eta}_i$  parameter sequentially by calculating measurement and model PDF for the  $i^{th}$  parameter and combining them into the posterior PDF with the prior PDF. In this study, we use two considerations of a priori information in the cloud properties. The first prior PDF evaluated in space  $\Pi_{liq}$  or  $\Pi_{ice}$  to be introduced into the GENRA algorithm is non-informative and is equivalent to unity for every cloud property doublet (i.e. all combinations of  $\tau$  and  $r_e$  are equally likely). In space  $\Pi_{com}$ , the first prior PDF is partially-informed and is equivalent to unity wherever the cloud property triplet is expected to naturally occur (for all  $\tau < 100$ , liquid water clouds with  $r_e$  as large as  $30 \mu\text{m}$  and ice clouds with  $r_e$  ranging between  $10 \mu\text{m}$  and  $60 \mu\text{m}$ ), at any other triplet the prior PDF is set to 0. Therefore, there are more possible  $\tau$  and  $r_e$  combinations when  $\phi = ice$  than  $\phi = liquid$  in space  $\Pi_{com}$ . For each subsequent  $i^{th}$  parameter

introduced iteratively into the algorithm, we can choose how to apply, or update, the prior knowledge dependent upon what information content is desired about the retrieval. For example, using a partially- or non-informative prior PDF for every parameter introduced results in a posterior PDF that is specific to each parameter (i.e. retrieval information is characterized separately for each individual parameter). If, however, we update the prior PDF at each step using the posterior PDF from the previous step in the iterative process, what results is the final cumulative retrieval information based on all parameters introduced into the algorithm, known as the final posterior PDF. The order in which the prior is updated does not influence the total SIC of the final solution, but would impact relative increments in SIC.

**4b.** *The normalization coefficient,  $\gamma$ :*

$\gamma$  is required to force the integral of the posterior PDF to equal unity and is calculated from the convolution of the prior, the model, and the measurement PDF. The normalization coefficient [adapted from *Vukicevic and Posselt, 2008*] can be evaluated for each parameter by

$$\gamma = \int_D \int_{\Pi} p_{\text{prior}}^n p_{\text{meas}} p_{\text{model}}^n d\mathbf{n} d\boldsymbol{\eta} \quad (4.6)$$

This equation only holds if the measurement space,  $D$ , varies with equal separations. For separations that are unequal, the normalization coefficient must be evaluated with the use of homogeneous probability density [see Eq. (2.2) of *Vukicevic and Posselt, 2008*]. Note that applying this coefficient to ensure the area of the posterior PDF is equal to 1 for each parameter changes the magnitude, but not the shape, of the posterior PDF. It is the shape of the likelihood function convolved with a priori information in the cloud properties, which determines the posterior PDF, and subsequent retrieval diagnostics derived from it such as the maximum likelihood solution and the SIC. Assuring that the normalization coefficient is properly evaluated is essential for the valid comparison of retrievals from the same or different platforms where a) different physical measurements are used in the retrieval, similar to the parameters, or b) different grid spacing is used in the respective LUT.

Special considerations in calculating  $\gamma$  are required when applied to clouds spanning 2 ther-

modynamic phases. For all applications of the GENRA algorithm to date [Coddington *et al.*, 2012, 2013; Vukicevic *et al.*, 2010], the precision of  $\tau$  and  $r_e$  were evaluated for clouds of a single (liquid) thermodynamic phase. This previous application is repeated in a similar manner in this study when evaluating the PDFs based on the spaces  $\Pi_{liq}$  or  $\Pi_{ice}$ . If the precision of  $\tau$  and  $r_e$  is evaluated with a second phase, where two likelihood functions are combined ad-hoc, it would be necessary to include an extra homogenization factor to ensure that the measurement space and cloud property space for the likelihood functions from both thermodynamic phases represent the same area. By directly addressing the thermodynamic phase as a retrieved property, and including it as one of the dimension in the cloud property space, such as done for  $\Pi_{com}$ , the homogenization factor is not required and only the normalization coefficient, defined in Eq. 4.6, is required.

#### 4.4.4 Retrieval Diagnostics

One retrieval diagnostic derived from the posterior PDF is the maximum likelihood solution. This is defined as the combination of  $\tau$  and  $r_e$  in spaces  $\Pi_{liq}$  or  $\Pi_{ice}$ , or  $\tau$ ,  $r_e$ , and  $\phi$  in the space  $\Pi_{com}$  where the posterior PDF returns its maximum value.

A second diagnostic is the marginal PDF, the unconditional probability of the cloud properties, obtained by integrating the posterior PDF over a subset of the cloud property space (Eq. 4.7-4.9). The  $\phi$ -marginal PDF, Eq. 4.9, can only be evaluated with the posterior PDF defined in the space  $\Pi_{com}$ , whereas the  $\tau$ - and  $r_e$ -marginal PDF are evaluated with the posterior PDF defined in the space  $\Pi_{liq}$  or  $\Pi_{ice}$ .

$$p_{marg}(\tau) = \int p_{post}(\tau, r_e) dr_e \quad ; \text{ where } p_{post}(\tau, r_e) \in \Pi_{liq} \text{ or } \Pi_{ice} \quad (4.7)$$

$$p_{marg}(r_e) = \int p_{post}(\tau, r_e) d\tau \quad ; \text{ where } p_{post}(\tau, r_e) \in \Pi_{liq} \text{ or } \Pi_{ice} \quad (4.8)$$

$$p_{marg}(\phi) = \int \int p_{post}(\tau, r_e, \phi) dr_e d\tau \quad ; \text{ where } p_{post}(\tau, r_e, \phi) \in \Pi_{com} \quad (4.9)$$

Each marginal PDF will have an associated mean and error variance. If the posterior PDF is Gaussian distributed, the statistical mean of the marginal PDFs will coincide with the maximum likelihood solution of the posterior PDF [Vukicevic *et al.*, 2010]. For a non-Gaussian posterior PDF, this relationship is not upheld and the degree of discrepancy would depend on the shape of the posterior PDF [Coddington *et al.*, 2013]. In this work, most posterior PDF are non-Gaussian, similar to the shape of the measurement PDFs presented in Fig. 4.5. The uncertainty range for  $\tau$  and  $r_e$  is the error variance (i.e. precision) of the marginal PDFs but the retrieved solution is calculated from the maximum likelihood value of the posterior PDF.

Since the retrieved  $\phi$  is a binary value (either liquid or ice), we report the probability of retrieving one particular cloud thermodynamic phase rather than an uncertainty. This probability is represented by the marginal PDF for ice ( $p_{marg}(\phi)|_{\phi=ice}$ ) or liquid ( $p_{marg}(\phi)|_{\phi=liquid}$ ). These marginal PDFs are related to each other by  $p_{marg}(\phi)|_{\phi=ice} = 1 - p_{marg}(\phi)|_{\phi=liquid}$ , since they are derived from the posterior PDF which is normalized to 1. Probability values between 0 and 1 do not imply a mixed phase cloud.

A third retrieval diagnostic is the SIC [Shannon and Weaver, 1949] which uses the thermodynamic entropy,  $S$ , to quantify the information of any one PDF,  $p(x)$ . The SIC values are used to compare the information in cloud properties gained from the different parameters. Through varying treatment of the prior PDF (i.e. non-informative prior, updated prior) one can determine the individual information each parameter holds on the nature of the cloud properties, and which set of parameters holds the greatest cumulative retrieval information. The entropy is defined as

$$S(x) = - \sum_{N^*} p(x) \log_2 p(x) \quad (4.10)$$

When evaluating the combined precision of  $\tau$  and  $r_e$  in the space  $\Pi_{liq}$  or  $\Pi_{ice}$ ,  $p(x)$  is the posterior PDF and  $N^*$  is its number of points, equivalent to  $N$ . When evaluating the precision of either  $\tau$  or  $r_e$  independently,  $p(x)$  is the  $\tau$ - or  $r_e$ -marginal PDF described with  $N^*$  points of  $\tau$  or  $r_e$ . The maximum entropy occurs when every possibility is equally probable, while zero entropy occurs

when there is a sole  $\tau$  and  $r_e$  combination with a probability density of unity (i.e. uniquely defined solution). Conversely, the SIC,  $H^*$ , (Eq. 4.11) is a difference between the entropy of the posterior state,  $S_{post}$ , and the entropy of the prior state,  $S_{prior}$ .  $H^*$  is a relative measure of the information gained (increasing in magnitude) or lost (reducing in magnitude) from the prior state. The SIC is inversely related to error variance [Coddington *et al.*, 2013], thereby providing a measure of retrieval precision, but not retrieval accuracy.

$$H^* = S_{prior} - S_{post} \quad (4.11)$$

In the GENRA approach, a theoretical maximum SIC,  $H_{max}$ , is defined as the logarithm of  $N^*$ . By normalizing the SIC by the theoretical maximum, the normalized SIC values range between zero and unity, with unity representing the maximum SIC.  $H$  represents the normalized SIC calculated from the posterior PDF, while  $H_\tau$  and  $H_{r_e}$  represent the normalized SIC calculated from the  $\tau$ - and  $r_e$ -marginal PDF, respectively.

A final retrieval diagnostic is the evaluation/characterization of retrieval bias or accuracy. The retrieval bias is the difference between the maximum likelihood solution of the posterior PDF and the true  $\tau$ ,  $r_e$ , and  $\phi$  value defined by the grid of input values used to model the spectral zenith radiance. The retrieval bias is independent of the retrieval precision, and can only be defined with additional information such as measurement by independent instrument, or modeling study as shown here.

## 4.5 Results: Simulated Spectral Transmittance

Insight in the accuracy and precision of the retrieval method can be gained by applying the GENRA methodology to a set of modeled transmittance spectra. The retrieval diagnostics are applied to the posterior PDF, which was calculated by combining the measurement PDF, model PDFs, and prior PDF.

### 4.5.1 Sample case studies modeled spectra

For each of the 3 cloud cases, the posterior PDFs are evaluated by following Eq. 4.3 with the prior PDF iteratively updated for each of the 15 parameters, except  $\eta_8$  and  $\eta_{10}$  since they showed large variance with changes in precipitable water. The final posterior PDFs for case A are defined in the space  $\Pi_{liq}$  and the final posterior PDFs for case B and C are defined in the space  $\Pi_{ice}$ . The measurement PDFs, described by their mean and the standard deviation presented in Table 4.2, are combined with model PDFs, described by a variability of less than 2% of the total range in values of parameters. The first prior PDF is non-informative, or uniform, over the entire range of  $\tau$  and  $r_e$ . Figure 4.6 shows the final posterior PDFs, where contours of probability indicate how well each combination of  $\tau$  and  $r_e$  represent the input measurement PDFs.

Table 4.2: Parameters with measurement uncertainties for the 3 cloud cases

	<b>Case A - Liquid</b> $\tau=40, r_e=7 \mu\text{m}$	<b>Case B - Ice</b> $\tau=20, r_e=50 \mu\text{m}$	<b>Case C - Ice</b> $\tau=5, r_e=25 \mu\text{m}$
$\eta_1$	$0.577 \pm 0.010$	$0.103 \pm 0.019$	$0.3627 \pm 0.0073$
$\eta_2$	$-0.148 \pm 0.038 \mu\text{m}^{-1}$	$-3.230 \pm 0.049 \mu\text{m}^{-1}$	$-0.2943 \pm 0.041 \mu\text{m}^{-1}$
$\eta_3$	$1.282 \pm 0.019 \mu\text{m}^{-1}$	$0.0011 \pm 0.031 \mu\text{m}^{-1}$	$2.203 \pm 0.026 \mu\text{m}^{-1}$
$\eta_4$	$0.8458 \pm 0.0009$	$1.1982 \pm 0.0047$	$0.8957 \pm 0.0006$
$\eta_5$	$0.173 \pm 0.016$	$0.0843 \pm 0.0076$	$0.2190 \pm 0.020$
$\eta_6$	$0.0394 \pm 0.0034$	$0.00019 \pm 0.00022$	$0.0615 \pm 0.0054$
$\eta_7$	$0.367 \pm 0.034$	$0.337 \pm 0.031$	$0.404 \pm 0.038$
$\eta_8$	$0.193 \pm 0.004$	$-0.0015 \pm 0.0079$	$0.2066 \pm 0.0035$
$\eta_9$	$-0.0970 \pm 0.0008 \mu\text{m}^{-1}\text{nm}^{-1}$	$-0.0394 \pm 0.0015 \mu\text{m}^{-1}\text{nm}^{-1}$	$-0.06777 \pm 0.00059 \mu\text{m}^{-1}\text{nm}^{-1}$
$\eta_{10}$	$-0.0739 \pm 0.0004 \mu\text{m}^{-1}\text{nm}^{-1}$	$-0.0031 \pm 0.0003 \mu\text{m}^{-1}\text{nm}^{-1}$	$-0.06124 \pm 0.00039 \mu\text{m}^{-1}\text{nm}^{-1}$
$\eta_{11}$	$-1.549 \pm 0.043 \mu\text{m}^{-1}$	$-1.625 \pm 0.042 \mu\text{m}^{-1}$	$-1.378 \pm 0.048 \mu\text{m}^{-1}$
$\eta_{12}$	$0.371 \pm 0.035$	$0.333 \pm 0.031$	$0.401 \pm 0.038$
$\eta_{13}$	$1.124 \pm 0.005$	$1.1667 \pm 0.0064$	$1.1584 \pm 0.0050$
$\eta_{14}$	$1.519 \pm 0.022$	$1.444 \pm 0.026$	$1.480 \pm 0.021$
$\eta_{15}$	$0.00471 \pm 0.00005 \text{nm}^{-1}$	$0.0300 \pm 0.00003 \text{nm}^{-1}$	$0.00322 \pm 0.00003 \text{nm}^{-1}$

For all 3 cases, the maximum likelihood solution falls directly on top of the truth. The contours of probability are nearly symmetrically centered on the maximum likelihood solutions (Fig. 4.6). Both case A and C have high information content, with SIC of 0.95 and 0.94 respectively. Thus, the posterior PDFs are almost unity at one combination of  $\tau$  and  $r_e$  resulting in a near perfect diamond shaped contours. Case B has a SIC of 0.74, smaller than case A and C. Non-zero

probabilities, in case B, extend from the maximum likelihood solution at  $\tau=20$  and  $r_e=50 \mu\text{m}$ , denoted by the X, to a second maxima at  $\tau=21$  and  $r_e=47 \mu\text{m}$  with a probability of less than half the maximum likelihood. Case A, a modeled liquid water cloud of  $\tau=40$  and  $r_e=7 \mu\text{m}$ , has the most certain maximum likelihood solution of all 3 cases, giving  $\tau = 40 \pm 0.4$  and  $r_e = 7 \pm 0.1 \mu\text{m}$ . Case B has a broader uncertainty range with  $\tau = 20 \pm 1.7$  and  $r_e = 50 \pm 5.2 \mu\text{m}$ . Case C has a maximum likelihood solution of  $\tau = 5 \pm 0.1$  and  $r_e = 25 \pm 1.1 \mu\text{m}$ .

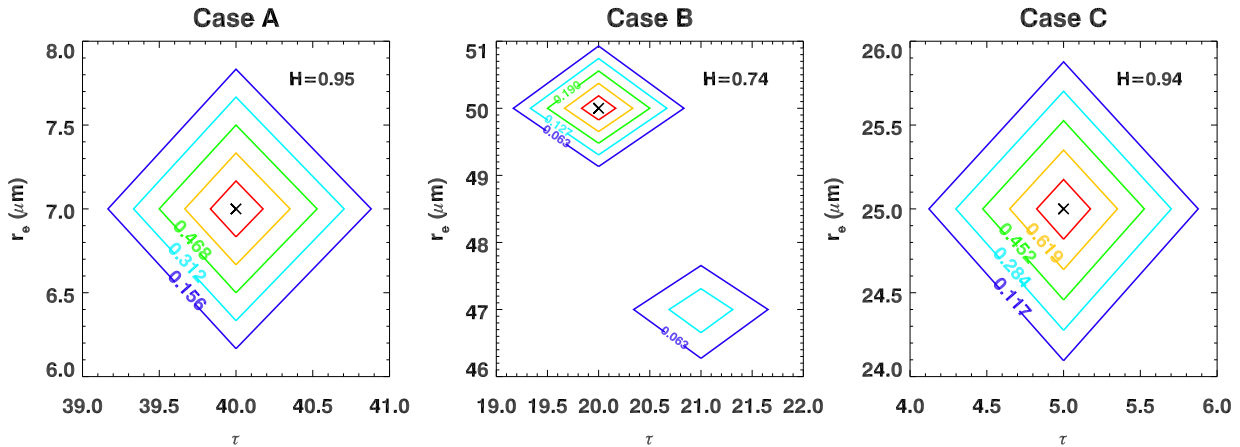


Figure 4.6: Posterior PDF for cloud cases A, B, and C. The colors denote the probability of the selected pair of  $\tau$  and  $r_e$  to describe the measured spectrum. The colors for each case denote different probabilities, indicated directly on the contour. The highest probability is denoted by the red contour, while the smallest non-zero probability is indicated by the blue contour. The black X denotes the maximum likelihood solution. The x- and y-axes are magnified to center on the optical thickness and effective radius regions where the posterior PDF has a non-zero probability.

The uncertainties of the retrieved  $\tau$  and  $r_e$  are determined by the variance of their marginal PDFs. Figure 4.7 shows the  $r_e$ - and  $\tau$ -marginal PDFs for all 3 cloud cases. Cases A and C have information content near unity in the  $\tau$ -marginal PDFs, with  $H_\tau = 0.82$  and  $H_\tau = 0.97$  respectively. The re-marginal PDFs for case A and C have an information content of  $H_{r_e} = 0.99$  and  $H_{r_e} = 0.71$ , respectively. Case B has lower information content than the other 2 cases and therefore has a larger uncertainty range for both  $\tau$  and  $r_e$ . The  $r_e$  uncertainty range for case C represents 11.6% of the maximum likelihood solution.

Figure 4.8 shows the contribution of normalized SIC from each parameter for the 3 cloud

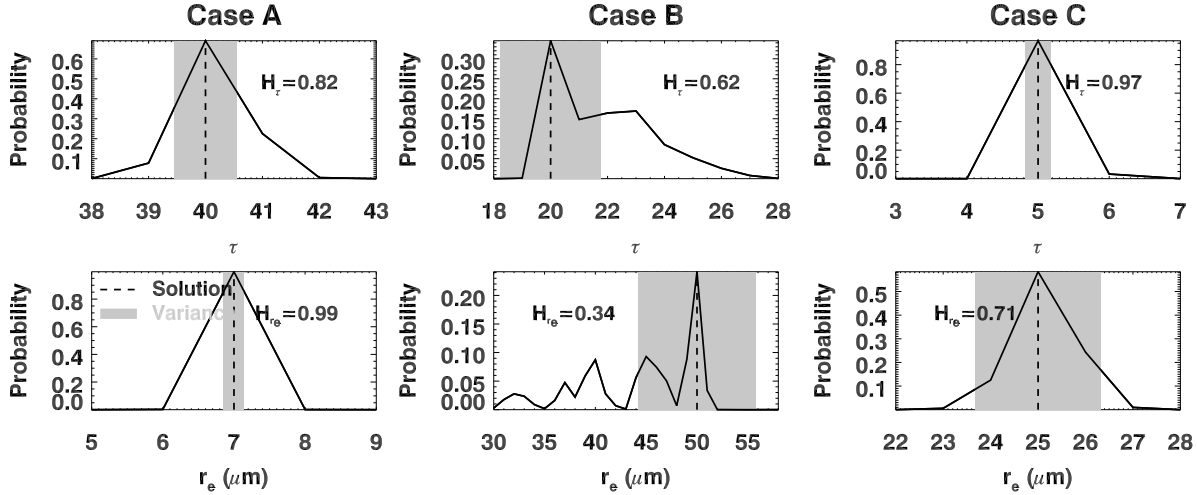


Figure 4.7: Marginal PDFs in optical thickness (top panels) and effective radius (bottom panels) for the 3 cloud cases. For each marginal PDF, the shaded region denotes its variance, while the dashed line denotes the maximum likelihood solution in either optical thickness or effective radius. The SIC calculated from the marginal PDF (either  $H_\tau$  or  $H_{re}$ ) is reported on each panel.

cases. The independent SIC of each parameter is calculated from the posterior PDF without updating the prior PDF (Fig. 4.8a). The contribution to the final SIC by each parameter (Fig. 4.8b) is calculated from the posterior PDF when the prior PDF is updated and represents the parameter-dependent cumulative SIC.

The parameter containing the highest independent SIC is different for each of the 3 cases. For at least one of the three cases, the parameters  $\eta_3$ ,  $\eta_5$ ,  $\eta_6$ , and  $\eta_{15}$  have an independent SIC greater than 0.4.  $\eta_3$ ,  $\eta_6$ , and  $\eta_{15}$  ( $\partial/\partial\lambda_{1.5}$ ,  $\langle R \rangle_{1.6}$ , and  $sl_{1.6}$ , respectively) have the highest independently calculated SIC for case A (Fig. 4.8a). These parameters are defined at wavelengths ranging between 1500 nm–1640 nm. In this wavelength range, bulk absorption by ice and liquid cloud particles is greater than absorption at all shorter wavelengths. Therefore, the absorption in that wavelength band is more sensitive to effective radius than all shorter wavelength bands. For case B,  $\eta_3$ ,  $\eta_6$ , and  $\eta_{15}$  have an independent SIC of less than 0.06 since radiance over that wavelength range is nearly entirely attenuated, unlike radiance in the same wavelength range for case A and C. To gain more information on  $\tau$  and  $r_e$ , a parameter defined at wavelengths where radiance is not entirely attenuated is required. The single parameter that gives the most information content for case B is

$\eta_5$  ( $\langle R \rangle_{1.25}$ ), defined at a wavelength where absorption by either ice or liquid water is less than at longer wavelengths, from 1500 nm to 1640 nm. Both  $\eta_5$  and  $\eta_6$  result in a SIC of greater than 0.4 for case C.

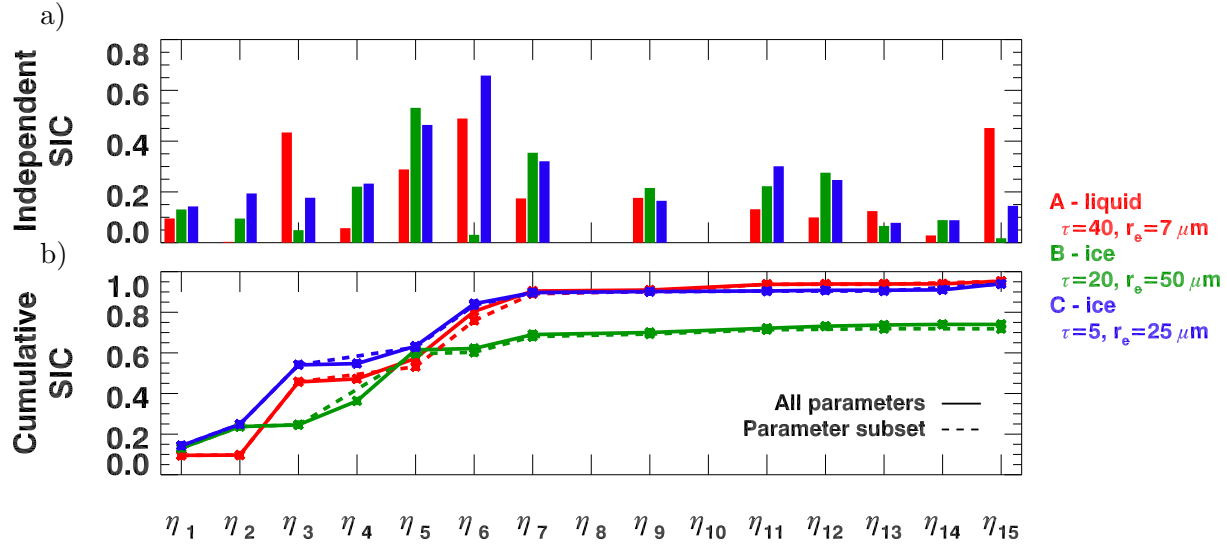


Figure 4.8: The Shannon information content (SIC) for each parameter for the 3 cloud cases. SIC for each parameter can be calculated (a) independently or (b) cumulatively (see text). The dashed lines represent the cumulative SIC where only a subset of parameters are used ( $\eta_1, \eta_2, \eta_3, \eta_5, \eta_6, \eta_7, \eta_9, \eta_{11}, \eta_{13},$  and  $\eta_{15}$ ) and describes similar cumulative SIC obtained by combining all parameter (solid lines).

Although all parameters result in non-zero independent SIC, their contributions to the cumulative SIC are typically much less than their independently-calculated value. This means that much of the information for  $\tau$  and  $r_e$  contained within different parameters is repeated. The most information not found in the previous parameters resides in  $\eta_3$  ( $\partial/\partial\lambda_{1.5}$ ) for cloud case A and C, and  $\eta_5$  ( $\langle R \rangle_{1.25}$ ) for cloud case B. This is determined by the biggest jump in SIC after ingesting those parameters into GENRA. For the liquid water cloud case (A), the SIC is 0.90 after  $\eta_7$  ( $\langle R \rangle_{1.0}$ ) is ingested, which represents 95% of the SIC after ingesting all parameters (0.95 for case A). Similarly for the cloud cases B and C, the first 7 parameters represent 93% and 95% of the SIC with all parameters, respectively. By omitting  $\eta_4, \eta_{12}$ , and  $\eta_{14}$ , the SIC calculated from the final posterior PDF is reduced by only 0.0006, 0.02, and 0.001 for cloud cases A, B, and C respectively. Therefore,

the parameters  $\boldsymbol{\eta}_1, \boldsymbol{\eta}_2, \boldsymbol{\eta}_3, \boldsymbol{\eta}_5, \boldsymbol{\eta}_6, \boldsymbol{\eta}_7, \boldsymbol{\eta}_9, \boldsymbol{\eta}_{11}, \boldsymbol{\eta}_{13}$ , and  $\boldsymbol{\eta}_{15}$  ( $C_{1.0}, \partial/\partial\lambda_{1.2}, \partial/\partial\lambda_{1.5}, \langle R \rangle_{1.25}, \langle R \rangle_{1.6}, \langle R \rangle_{1.0}, \partial^2/\partial\lambda_{1.0}^2, sl_{0.55}, r_{1.0}$ , and  $sl_{1.6}$ ) are sufficient to define the solution of  $\tau$  and  $r_e$ , and are now referred to as the subset of the parameters. Although not all of the parameters in the subset contribute to the cumulative SIC for the 3 cloud case, each parameter does contribute by more than 0.01 to the cumulative SIC of the solution of at least one cloud case (Fig. 4.8b). 7 of the parameters ( $\boldsymbol{\eta}_1, \boldsymbol{\eta}_2, \boldsymbol{\eta}_3, \boldsymbol{\eta}_5, \boldsymbol{\eta}_6, \boldsymbol{\eta}_9, \boldsymbol{\eta}_{11}$ , and  $\boldsymbol{\eta}_{15}$ ) were identified to have the largest sensitivity to  $\tau, r_e$ , and  $\phi$  [LeBlanc et al., 2014] and are also contained in the subset of the parameters. The two other parameters identified to have large sensitivities ( $\boldsymbol{\eta}_8$  and  $\boldsymbol{\eta}_{10}$ ) were omitted in this analysis since they showed large variance with changes in precipitable water.

Another measure of the retrievals precision is the variance in marginal PDF, which defines the uncertainty in  $\tau$  and  $r_e$ . By ingesting new information into GENRA, this uncertainty is typically reduced. The uncertainty in  $\tau$  and  $r_e$  is dependent on each parameter (Fig. 4.9), where ingestion of a small number of parameters produces a greater reduction of the uncertainty in  $\tau$  than in  $r_e$ . For example, the uncertainty in  $\tau$  decreases below 5 after only 2 parameters have been ingested for case C, while the uncertainty in  $r_e$  requires 6 parameters to reach an uncertainty of  $5 \mu\text{m}$ . All 3 cloud cases return uncertainties in  $\tau$  less than 1.7 after ingesting all or only the subset of the parameters (Fig. 4.9a). The uncertainties in  $r_e$  for cases A, B, and C are reduced to  $0.1 \mu\text{m}$ ,  $5.2 \mu\text{m}$ , and  $1.1 \mu\text{m}$  after ingesting the subset of the parameters (Fig. 4.9b). The order by which the parameters are ingested does not change the final outcome of their uncertainty. As expected, the SIC varies inversely with the uncertainty; Case A has the smallest uncertainty in  $r_e$  and the largest SIC, while case B has the largest  $r_e$  uncertainty and the smallest SIC.

#### 4.5.2 Information content, uncertainty, and biases for ice and liquid water clouds of varying $\tau$ and $r_e$

SIC calculated from the posterior PDF, defined in space  $\Pi_{liq}$  and  $\Pi_{ice}$ , for liquid and ice clouds, respectively are presented in Fig. 4.10. The average SIC for ice clouds (0.75) is smaller than the average SIC for liquid water clouds (0.87), due to the low SIC for ice clouds with  $\tau > 60$

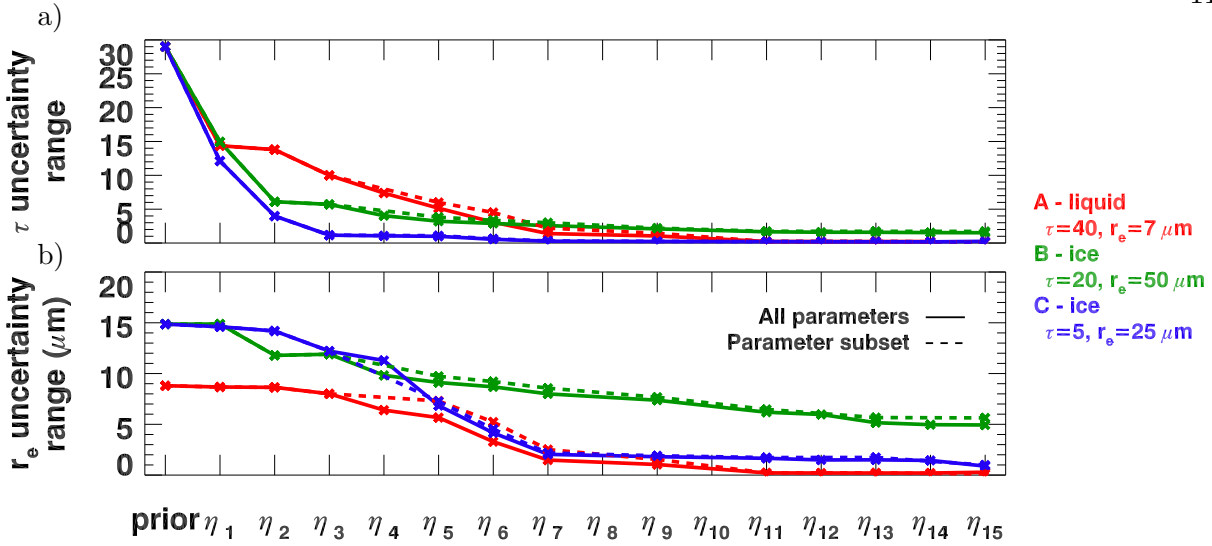


Figure 4.9: The uncertainty of optical thickness (a) and effective radius (b) as a function of ingested parameters for the 3 cloud cases. The uncertainties after ingesting a subset of the parameters are indicated by the dashed line. The prior uncertainty in  $\tau$  and  $r_e$  is described as the standard deviation of the marginal PDF of a non-informative prior PDF defined in cloud property space  $\Pi_{liq}$  for case A, and  $\Pi_{ice}$  for case B and C.

and  $r_e > 25 \mu\text{m}$ . The most certain solutions, with highest SIC, occur for both ice and liquid water clouds at  $\tau < 20$  and  $r_e < 15 \mu\text{m}$  for liquid droplets and  $r_e < 25 \mu\text{m}$  for ice particles. The SIC is reduced by up to 0.3 for liquid water clouds and up to 0.55 for ice clouds with increasing  $r_e$  and increasing  $\tau$  (past 40). This behavior is expected as clouds with  $\tau > 20$  result in smaller transmitted radiance, and therefore lower signal-to-noise ratio than clouds with  $\tau < 20$ . In particular, between 1500 - 1640 nm ice cloud transmittance with  $\tau > 40$  is completely attenuated. This reduces the signal-to-noise ratio of the parameters that typically give the most information on  $r_e$  ( $\eta_3$ ,  $\eta_6$ , and  $\eta_{15}$ ).

The parameters that contribute the most to the solution differ for clouds with varying  $\tau$ ,  $r_e$ , and  $\phi$ , as seen in Fig. 4.8 for the 3 cloud cases. To better understand the influence of each parameter on the SIC calculated from the final posterior PDFs, we divided the cloud property space,  $\Pi_{liq}$  and  $\Pi_{ice}$ , into three regions: 1 - optically thin clouds ( $\tau < 20$ ), 2 - optically thick clouds ( $\tau > 20$ ) with large particles ( $r_e > 15 \mu\text{m}$  for liquid cloud droplets and  $r_e > 25 \mu\text{m}$  for ice particles),

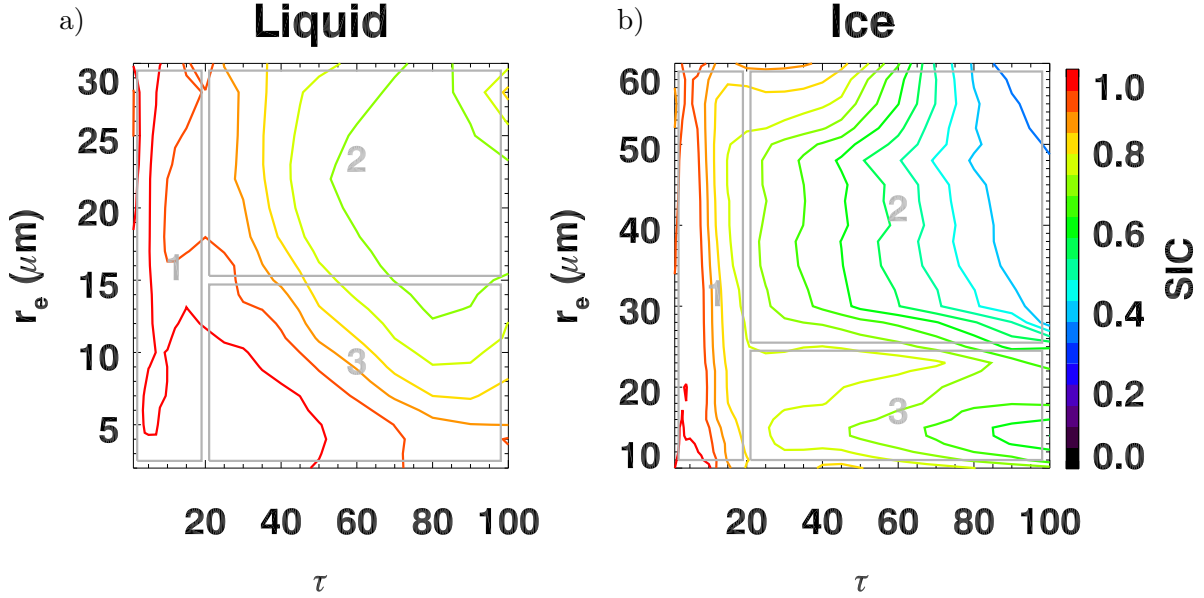


Figure 4.10: Shannon information content (distinguished by colored-contour lines) calculated from each final posterior PDF with a subset of parameters determined from simulated measurement with varying optical thickness and effective radius presented for (a) liquid and (b) ice clouds. The grey boxed regions related to 1 – thin clouds, 2 – thick clouds with large particles, and 3 – thick clouds with small particles.

and 3 - optically thick clouds ( $\tau > 20$ ) with small particles ( $r_e < 15 \mu\text{m}$  for liquid cloud droplets and  $r_e < 25 \mu\text{m}$  for ice particles), identified by the grey regions in Fig. 4.10. The cumulative SIC as a function of ingested parameter for each region are presented in Fig. 4.11. A small set of parameters cause the largest increase in SIC for clouds in region 1, whereas increases in SIC for clouds in region 2 and 3 are spread out over a greater number of parameters. Also, the average SIC for clouds in region 1 (liquid 0.94, ice 0.85) is greater than clouds in region 3 (liquid 0.86, ice 0.68), which is in turn greater than clouds in region 2 (liquid 0.74, ice 0.60).

The set of parameters that contributes the most to the cumulative SIC for clouds in region 1 is composed of  $\boldsymbol{\eta}_1$ ,  $\boldsymbol{\eta}_3$ ,  $\boldsymbol{\eta}_5$ ,  $\boldsymbol{\eta}_6$ , and  $\boldsymbol{\eta}_7$  ( $C_{1.0}$ ,  $\partial/\partial\lambda_{1.5}$ ,  $\langle R \rangle_{1.25}$ ,  $\langle R \rangle_{1.6}$ , and  $\langle R \rangle_{1.0}$ ) and includes  $\boldsymbol{\eta}_2$  ( $\partial/\partial\lambda_{1.2}$ ) for ice clouds.  $\boldsymbol{\eta}_3$  and  $\boldsymbol{\eta}_6$  stand out as the parameters that contribute the most to the cumulative SIC of clouds in region 1. This is not surprising since the spectral derivative of normalized radiance at 1500 nm and the mean normalized radiance near 1600 nm, parameterized

by  $\eta_3$  and  $\eta_6$ , respectively, are very sensitive to changes in  $\tau$  for  $\tau < 20$ , while always being directly proportional to  $r_e$  (see Fig. 3.10).

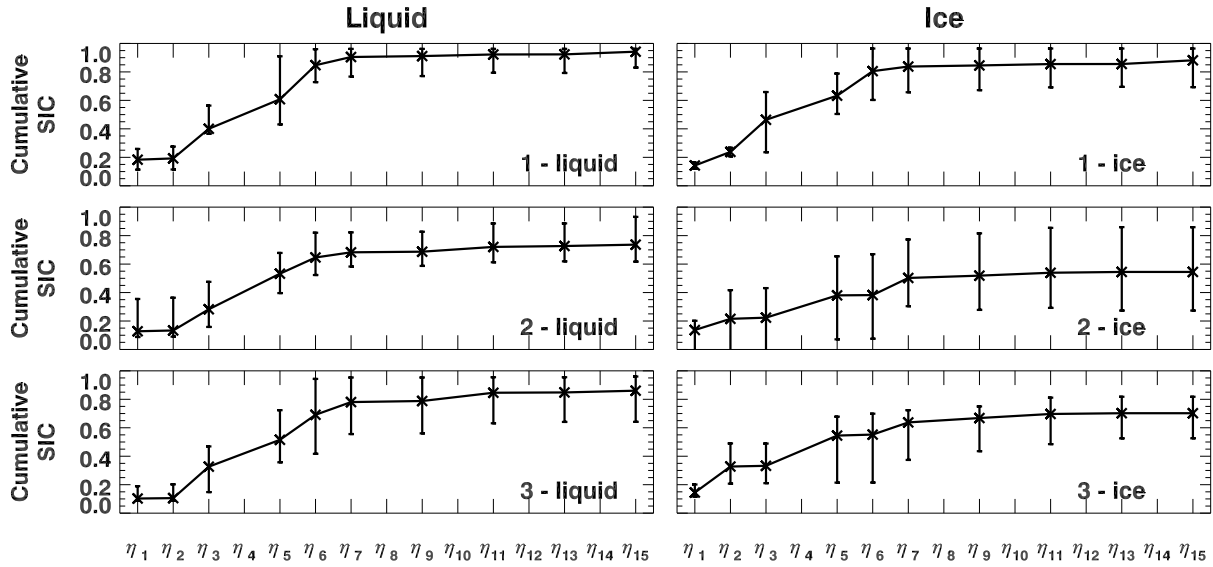


Figure 4.11: Cumulative SIC after sequential ingestion of each parameter into GENRA for the 3 regions of optical thickness, effective radius, and thermodynamic phase determined in Fig. 4.10. The regions are denoted by the legend in the bottom right side of each panel. The error bars at each parameter show the maximum and minimum value of SIC for that parameter in the specified region. The X denotes the mean cumulative SIC due to the particular parameter for that region.

The cumulative SIC for clouds in regions 2 and 3 increase in smaller increment after ingesting each parameter than for clouds in region 1. The increments in SIC are spread out over a larger set of parameters that include the same set identified for region 1 with the addition of  $\eta_{11}$  and  $\eta_{15}$  ( $sl_{0.55}$  and  $sl_{1.6}$ ) for liquid water clouds. For ice clouds, the set of parameters that contribute the most to the cumulative SIC is composed of  $\eta_1$ ,  $\eta_2$ ,  $\eta_5$ ,  $\eta_7$ ,  $\eta_9$ ,  $\eta_{11}$ , and  $\eta_{13}$  ( $C_{1.0}$ ,  $\partial/\partial\lambda_{1.2}$ ,  $\langle R \rangle_{1.25}$ ,  $\langle R \rangle_{1.0}$ ,  $\partial^2/\partial\lambda_{1.0}^2$ ,  $sl_{0.55}$ , and  $r_{1.0}$ ), which differs from the set for the liquid water cloud by the addition of  $\eta_2$ ,  $\eta_9$ , and  $\eta_{13}$  and the subtraction of  $\eta_3$ ,  $\eta_6$  and  $\eta_{15}$ . The parameters ( $\eta_3$ ,  $\eta_6$  and  $\eta_{15}$ ), defined at the wavelengths ranging between 1500–1640 nm have little influence on the cumulative SIC for ice clouds with  $\tau > 20$  (region 2 and 3), since radiance over that wavelength range is nearly entirely attenuated. The difference in SIC between ice clouds in region 2 and 3 is

largely due to the influence of  $\eta_2$ , which increases the SIC by 0.1 more in region 3 than region 2. This parameter quantifies the spectral derivative of normalized radiance at 1200 nm, which is more sensitive to ice clouds with  $r_e < 25 \mu\text{m}$  than with  $r_e > 25 \mu\text{m}$ . Radiance at 1200 nm is more attenuated for  $r_e > 25 \mu\text{m}$  because absorption increases with particle size, thus  $\eta_2$  returns a smaller signal than for  $r_e < 25 \mu\text{m}$ .

The uncertainties in retrieved  $\tau$  and  $r_e$  also vary depending on the region of the cloud property space (Fig. 4.12). The regions of smallest SIC coincide with the regions of highest uncertainty in  $\tau$  and  $r_e$ , with the most uncertain  $\tau$  and  $r_e$  combinations in region 2. Conversely, clouds in region 1, which have the highest SIC, represent the most certain  $\tau$  and  $r_e$ , with average uncertainties of  $\tau$  equal to  $\pm 0.2$  and  $r_e$  equal to  $\pm 0.6 \mu\text{m}$ . In addition, the average uncertainty in  $\tau$  is greater for ice clouds ( $\pm 1.3$ ) than for liquid water clouds ( $\pm 0.8$ ), whereas, the average uncertainty in  $r_e$  represents a similar percentage of  $r_e$  for both ice and liquid water clouds (4.8%). The overall distribution of  $\tau$  uncertainties is similar to the distribution of  $r_e$  uncertainties for liquid water clouds, but not for ice clouds. Ice clouds in region 3 have uncertainties in  $\tau$  similar to those in region 2 ( $\pm 2.2$ ), but uncertainties in  $r_e$  are smaller in region 3 ( $\pm 1.5 \mu\text{m}$ ) than region 2 ( $\pm 3.3 \mu\text{m}$ ). The mean relative uncertainty in  $\tau$  is less than the magnitude of the mean relative uncertainty in  $r_e$  for both ice and liquid clouds, in agreement with other methods based on transmitted radiance [McBride *et al.*, 2011].

The differences between the retrieved values and truth for all possible combinations of  $\tau$  and  $r_e$  for ice and liquid clouds represent the biases in the retrieval. For ice clouds in region 1 and 3 and all liquid water clouds, neither  $\tau$  nor  $r_e$  are biased. There is a negative bias in  $\tau$  for ice clouds in part of region 2 ( $\tau > 25$  and  $r_e > 30 \mu\text{m}$ ), where the true  $\tau$  exceeds the retrieval by as much as 8, and is accompanied by a positive bias in  $r_e$  as much as  $12 \mu\text{m}$ . Such large biases mean that the retrieval is not accurate for ice clouds with  $\tau > 25$  and  $r_e > 30 \mu\text{m}$ . These points coincide with SIC values of less than 0.5 and uncertainties in  $r_e$  greater than  $\pm 3.3 \mu\text{m}$ .

When applying the GENRA algorithm to the combined cloud property space  $\Pi_{com}$ , the probability of  $\phi$ -discrimination can be determined by calculating the marginal PDF for thermodynamic

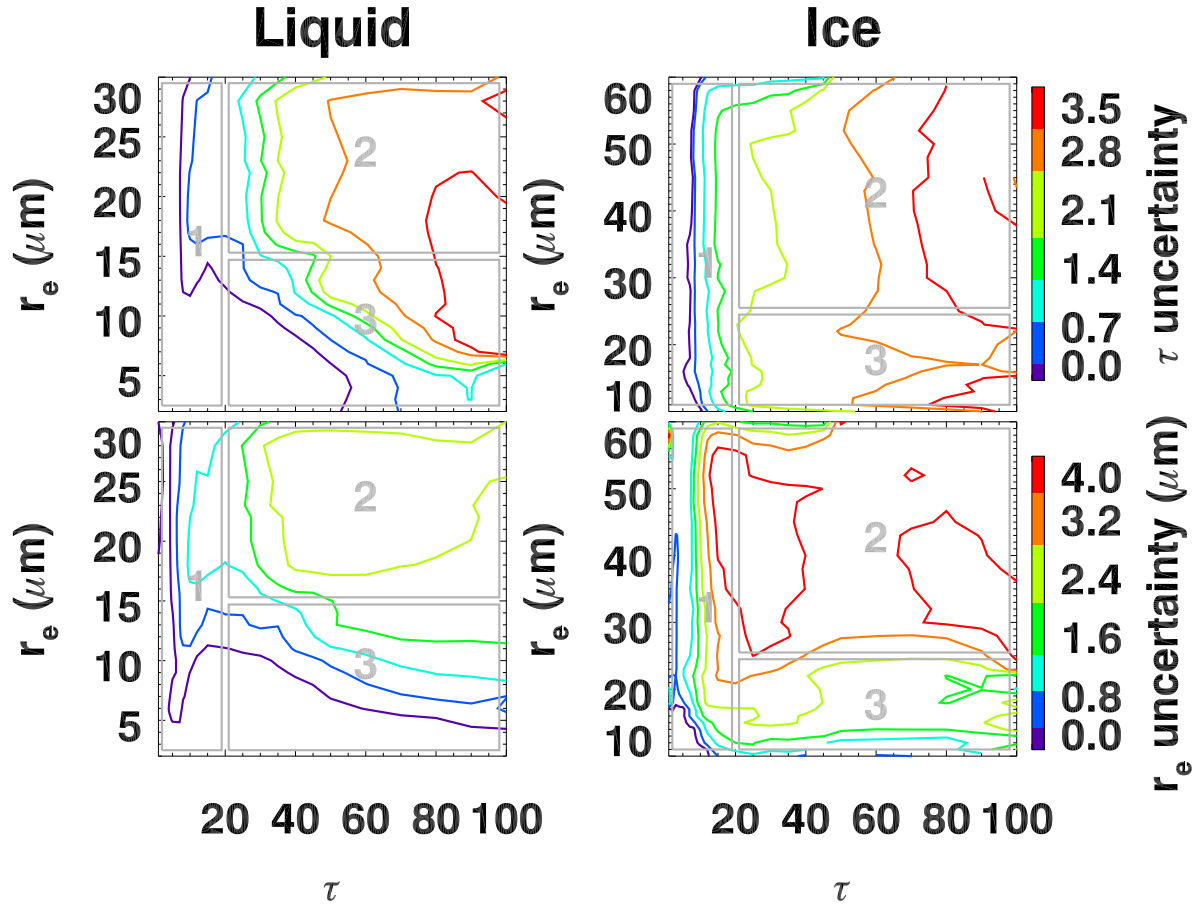


Figure 4.12: Uncertainties of  $\tau$  (upper panel) and  $r_e$  (bottom panel) for liquid (left column) and ice (right column) clouds are presented as a function of  $\tau$  and  $r_e$ . The values of each contour lines (denoted by different colors) refer to uncertainties in  $\tau$  or  $r_e$ . The grey boxes denote the same regions of the  $\tau$  and  $r_e$  introduced in Fig. 4.10

phase. The probability of obtaining either thermodynamic phase can be evaluated with the addition of every single parameter (Fig. 4.13). For the 3 cloud cases, a probability of greater than 98% of retrieving the correct thermodynamic phase was obtained after ingesting six parameters, even though these parameters are not ordered by information content of thermodynamic phase. The probability increases to 100% after all the parameters in the subset are ingested. Throughout the entire cloud property space,  $\phi$  is accurately determined with a probability that is never lower than 99.4% after ingesting all parameters in the subset.

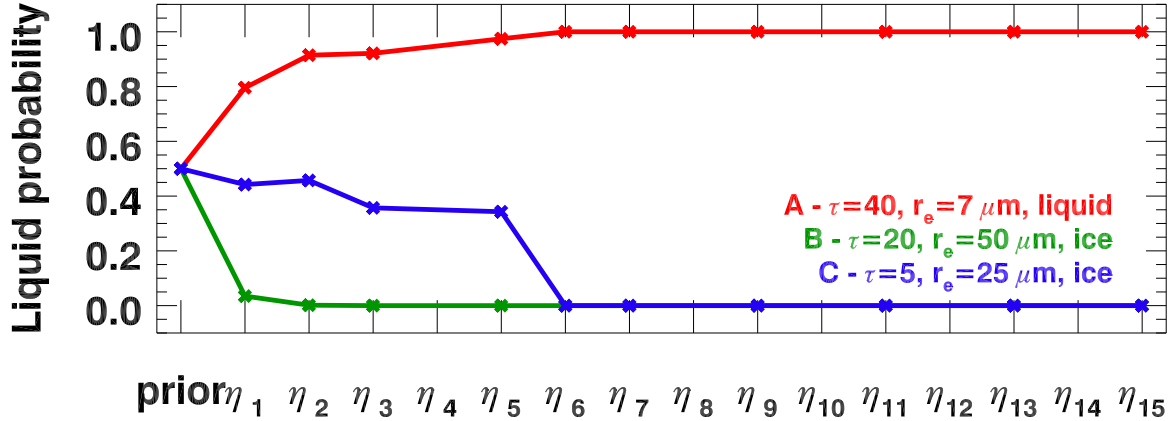


Figure 4.13: Probability of retrieving a liquid water cloud after ingesting the parameters sequentially within the GENRA algorithm for the 3 cloud cases. A liquid water cloud probability of 0 also means an ice cloud probability of 1.

#### 4.5.3 Effect of vertically varying effective radius on retrieval

To understand the effect of modifying the vertical profile of cloud particle size on the retrieval accuracy and precision, we used simulated radiance spectra based on clouds with  $r_e$  directly proportional to cloud geometrical height to define the measurement PDF. Although, not all clouds can be approximated with this vertical profile, we used this profile to uncover retrieval sensitivity to a vertically changing  $r_e$ . These measurement PDFs are used to calculate the maximum likelihood solutions, which are biased compared to the truth and less certain than equivalent solutions for clouds with vertically constant  $r_e$ . The average uncertainty in  $\tau$  increases from  $\pm 1.1$  for clouds with vertically constant particle sizes to  $\pm 2.1$  when  $r_e$  varies with cloud height. The uncertainties in  $r_e$  are also nearly doubled, as much as an average of  $\pm 2.6 \mu\text{m}$ , for clouds with vertically varying  $r_e$ .

The biases in  $\tau$  are smaller than the biases in  $r_e$  for both liquid and ice clouds, but for the combinations of  $\tau$  and  $r_e$  where there are positive  $\tau$  biases, the retrieved  $r_e$  will be negatively biased (Fig. 4.14). For liquid water clouds with a mean  $r_e > 5 \mu\text{m}$ , retrieved  $\tau$  are biased high by an average of +3.3%, whereas retrieved  $r_e$  are biased low by an average of -12%. The liquid water

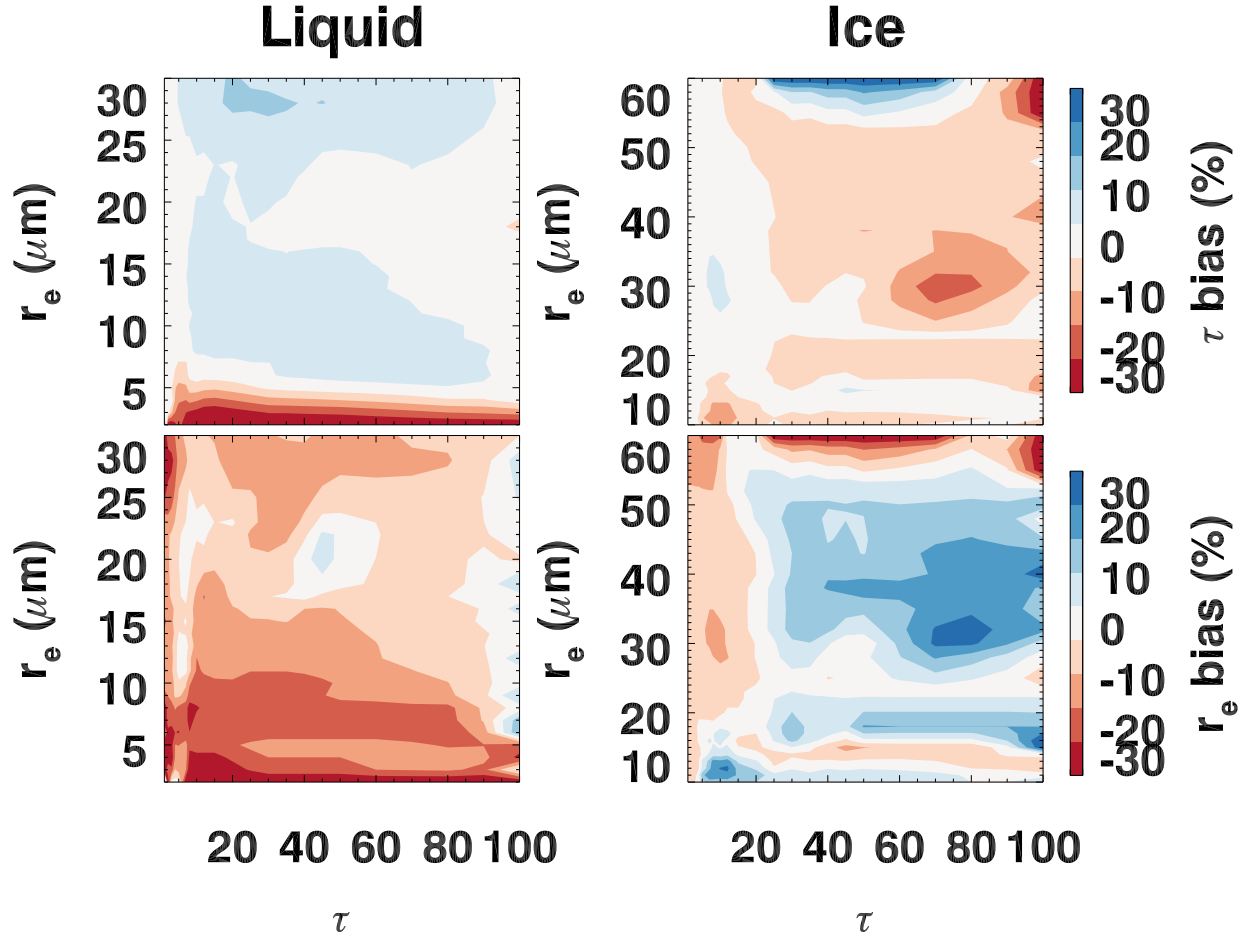


Figure 4.14: Bias in retrieved optical thickness (top panels) and effective radius (bottom panels) of liquid water clouds (left panels) spanning space  $\Pi_{liq}$  and ice clouds (right panel) spanning space  $\Pi_{ice}$  when the input simulated measurements include clouds with vertically varying effective radius. Negative biases (red) represent retrieved values less than the truth and positive biases (blue) represent retrieved values greater than the truth, with the white regions indicating no bias. The true values of  $r_e$  are the mean  $r_e$  of the vertical profiles of cloud particle sizes.

cloud droplets with a mean  $r_e < 5 \mu\text{m}$  result in a negative bias for both  $\tau$  and  $r_e$  of -28%. For ice clouds, retrieved  $\tau$  are on average smaller than the truth by -3.3% and retrieved  $r_e$  are on average larger than the truth by +2.3%. These biases are inverted for  $\tau < 20$  and  $r_e > 55 \mu\text{m}$ .

## 4.6 Summary and conclusions

We have characterized a retrieval [*LeBlanc et al.*, 2014] of cloud optical thickness, cloud particle effective radius, and cloud thermodynamic phase from a series of parameters derived from spectral features in transmittance. Previously, *LeBlanc et al.* [2014] determined uncertainties of  $\tau$  and  $r_e$  for ice and liquid water clouds using only measurement uncertainty, independent of variability in the atmospheric and surface conditions. Realistic model uncertainties were quantified by analyzing the impact of varying atmospheric and surface conditions on the 15 parameters derived from transmittance. It was found that all parameters, except for  $\eta_8$  and  $\eta_{10}$ , vary by less than 2% for changes in surface albedo, cloud base height, and precipitable water that occur during a day. Variations in cloud base height affect the parameters in a similar manner to the variations in precipitable water.  $\eta_7$ ,  $\eta_{11}$ ,  $\eta_{12}$ , and  $\eta_{14}$  are the most sensitive to surface albedo.

To quantify realistically the accuracy and precision of the new retrieval related to changes in ancillary inputs, we employed the GENRA methodology, which describes the retrieval process in terms of stochastic variables with PDFs. We calculated the SIC of the solution PDFs to quantify its information content. From the original 15 parameters, defined by *LeBlanc et al.* [2014], a minimum of 93% of the SIC is contained within the first 7 parameters for the 3 cloud cases presented. Furthermore,  $\eta_1$ ,  $\eta_2$ ,  $\eta_3$ ,  $\eta_5$ ,  $\eta_6$ ,  $\eta_7$ ,  $\eta_9$ ,  $\eta_{11}$ ,  $\eta_{13}$ , and  $\eta_{15}$  can be used to achieve a similar SIC (within 0.02) than the SIC obtained when all 15 parameters are ingested for any combinations of  $\tau$ ,  $r_e$ , and  $\phi$ . For different regions of the cloud property space, different parameters contribute the most to defining the retrieval solution. For example,  $\eta_2$  contributes no new information for liquid water clouds, but adds to the cumulative SIC by as much as 0.2 for ice clouds. The most information content is contained in solutions with  $\tau < 20$ , while ice clouds with  $r_e > 25 \mu\text{m}$  and  $\tau > 20$  have much less information content. In addition,  $\tau$  and  $r_e$  for ice clouds are less constrained than  $\tau$  and  $r_e$  for liquid water clouds. The retrieval for ice clouds with  $\tau > 25$  and  $r_e > 30 \mu\text{m}$  is biased low for  $\tau$  and biased high for  $r_e$ , and therefore should not be applied to clouds with these properties. The probability of identifying the correct thermodynamic phase is never smaller than 99.4% after

ingesting the subset of the parameters. When applying GENRA to simulated transmittance spectra of clouds with vertically varying  $r_e$ , the retrieval results became less certain than vertically constant  $r_e$  clouds and biased from truth. The maximum likelihood solution of  $\tau$  for liquid water clouds is on average 3.3% greater than truth whereas  $r_e$  is biased on average by 12% lower than truth. This behavior is inverted for ice clouds, where the maximum likelihood solutions of  $\tau$  are smaller than truth and  $r_e$  are larger than truth.

This work shows that  $\tau$  and  $r_e$  are accurately retrieved, and  $\phi$  is accurately determined, when using spectrally resolved shortwave zenith radiance measurements with realistic error characteristics. The use of a subset of the 15 parameters is sufficient to retrieve  $\tau$  and  $r_e$  for any liquid water cloud and any ice cloud of  $\tau < 25$  and  $r_e < 30 \mu\text{m}$ . We have also observed that the 15 parameters are sensitive to vertical variations in  $r_e$ , meaning that more information may be retrieved by using these parameters. Such information could be linked to mixed phase clouds, or vertical profiles of  $r_e$ . This will be the subject of future research.

#### 4.7 Acknowledgements

This work was partially supported from grant NNX11AK67G (remote sensing theory), entitled 'development and validation of new spectral cloud and aerosol retrievals'. We thank Warren Gore from NASA Ames for the use of the SSFR instrument. The MODIS MCD43B3 surface albedo data were obtained through the online Data Pool at the NASA Land Processes Distributed Active Archive Center (LP DAAC), USGS/Earth Resources Observation and Science (EROS) Center, Sioux Falls, South Dakota ([https://lpdaac.usgs.gov/get\\_data/](https://lpdaac.usgs.gov/get_data/)).

## Chapter 5

### Summary and Outlook

In this thesis, retrievals that use spectral measurements of shortwave radiation to quantify aerosol and cloud microphysical and optical properties were presented. The spectral radiation measurements were collected by the Solar Spectral Flux Radiometer (SSFR) from airborne and ground-based platforms. These measurements uncovered spectral signatures for either aerosols or clouds. This thesis focused on answering 3 main questions:

- (1) What are the impacts of aerosol on the spectrally-resolved net radiative effects? Is there a recurrent pattern in the radiative effects of aerosol observed in different locations?
- (2) What do spectral features in ground-based zenith radiance measurements reveal about cloud optical and microphysical properties?
- (3) How do naturally occurring variations in environmental conditions affect the accuracy and precision of the retrieval of cloud optical and microphysical properties from transmitted radiance?

To answer the first question, focus sampling of spectral irradiance above and below an aerosol layer was used to derive the change in net irradiance due to the presence of the aerosol. The aerosols were found to reduce the net irradiance below the layer, with the largest impact occurring at the shortest wavelengths sampled. This change is quantified with the spectral relative forcing efficiency, which was used to compare the impact of aerosols from locations such as the Los Angeles basin and northern Alberta, Canada, sampled during CalNex and ARCTAS respectively. The relative

forcing efficiency at any wavelength is within 20% for aerosol measured during the field missions CalNex, ARCTAS, MILAGRO, and INTEX-NA. Its spectral shape is consistent for all aerosols sampled. The average relative forcing efficiency below aerosol at 400 nm is -30% and increases with wavelength to near -5% per unit of midvisible optical thickness. These similarities, not expected a priori, may suggest that this quantity is constrained for various types of absorbing aerosols sampled during these experiments. In parameterized form, the spectra of relative forcing efficiency could be used for global estimates of the aerosol direct forcing, although more airborne irradiance measurements are required to quantify the variability of relative forcing efficiency for aerosols types not studied here.

Measurements of spectral irradiance and optical thickness are typically required to calculate relative forcing efficiency. However, no concurrent observations of optical thickness and spectral irradiance were available on the same airborne platform during CalNex. There was a separate airborne platform sampling profiles of aerosol extinction coefficient, which was used in lieu of aerosol optical thickness. To compensate for the time and space difference between the measurement of aerosol extinction coefficient and spectral irradiance, an existing technique of retrieving aerosol radiative forcing and aerosol properties was modified. In addition to the relative forcing efficiency, this iterative technique retrieved aerosol single scattering albedo, asymmetry parameter, surface albedo, and a modification factor to the aerosol optical thickness. The modification factor is used to adjust an initial estimate of aerosol optical thickness obtained from the vertical integration of the aerosol extinction coefficient. This method was validated with data taken during ARCTAS, where aerosol optical thickness was sampled on the same platform as spectral irradiance in addition in having a separate platform profiling the aerosol extinction coefficient.

To answer the second question, the sensitivity of cloud-transmitted radiance spectra to  $\tau$ ,  $r_e$ , and  $\phi$  was explored. The absorption and scattering properties of liquid and ice cloud particles modulate the spectral transmittance. When radiation is scattered by ice crystals, the cloud-transmitted radiance is consistently lower than radiance transmitted through a liquid water cloud with the same optical thickness. The absorption of radiation is, in part, governed by the bulk absorption coeffi-

cient and the cloud particle size. The ice absorption spectrum has local maxima that are shifted to longer wavelengths than in liquid water absorption, themselves shifted to longer wavelengths than the absorption maxima in water vapor. Since the scattering and absorption processes are wavelength dependent, the transmittance is either preferentially absorbed or scattered in varying wavelength regions, which results in spectral slopes, curvatures, maxima, and minima. These spectral shapes are sensitive to cloud optical and microphysical properties. When the radiance spectra are normalized by their maximum or by their value at 1000 nm, the spectral features and shapes are amplified, while the large scale variations in magnitude of the radiance spectra are eliminated. Furthermore, the sensitivity to spectrally independent changes in calibration is reduced by using normalized radiance.

Even though the large scale magnitude variation in radiances is removed, the spectral features are still dependent on  $\tau$  and can be used to uniquely derive  $\tau$ ,  $r_e$ , and  $\phi$ . 15 parameters quantify these shapes and features. By matching the 15 parameters derived from measurements to those derived from modeled transmittance spectra with a least squares fit, the retrieval obtained  $\phi$  first then  $\tau$  and  $r_e$ . Not all parameters are sensitive to  $\tau$ ,  $r_e$ , and  $\phi$  for all combinations of cloud properties. For example, the parameter,  $\eta_2$ , is sensitive to  $\tau$  and  $r_e$  variations in ice clouds but not in liquid water clouds. The sensitivity to  $\phi$  is due to the spectral differences between the absorption properties of ice and liquid water cloud particles.

A ground-based SSFR in Boulder, Colorado, collected radiance spectra during the time range between May 2012 and January 2013. We selected 3 cloud cases during this measurement period to represent a liquid water, a mixed-phase, and an ice cloud. The new retrieval and two other retrievals were used to extract  $\tau$ ,  $r_e$ , and  $\phi$  from transmittance measurements taken during the 3 cloud cases. Of the three retrievals, the best fit between measured and modeled radiance spectra is found when using the new retrieval based on multiple spectral features. In addition, the new retrieval yielded an ice cloud average  $r_e$ -uncertainty ( $\pm 1.2 \mu\text{m}$ ) smaller than the two other retrievals by at least 2.5 times.

To answer the third question, the retrieval accuracy and precision was evaluated with the GENRA method. GENRA built solution probability distributions that span every possible combination of  $\tau$ ,  $r_e$ , and  $\phi$  with natural variations in ancillary inputs and realistic measurement uncertainties. The solution probability distributions vary as each of the 15 parameters is ingested. The Shannon information content (SIC) evaluates the contributions from each parameter to the retrieval solution distribution. The parameters with the greatest contribution to SIC vary for different regions of the cloud property space.

The greatest SIC is found in clouds with  $\tau < 20$ , where large changes in SIC are due to only few parameters, meaning that these parameters are most sensitive to changes in cloud properties for optically thin clouds. In contrast to the optically thin clouds, clouds with  $\tau > 20$  have smaller SIC contributions spread over more parameters. The parameters that contribute the most the SIC for the optically thin clouds are defined at the wavelengths ranging between 1500 nm – 1640 nm and have little influence on the cumulative SIC for optically thicker clouds, since radiance over that wavelength range is nearly entirely attenuated. Solutions of ice clouds with  $r_e > 25 \mu\text{m}$  and  $\tau > 20$  contain the least information. By only using 10 parameters, an accurate solution of  $\tau$  and  $r_e$  for any liquid water cloud and for any ice cloud of  $\tau < 25$  and  $r_e < 30 \mu\text{m}$  is obtained with the same SIC than when using all 15 parameters (within 0.02). Of these parameters,  $\eta_3$  and  $\eta_6$  contribute the most to define the retrieval solution for clouds with  $\tau < 20$ . This high sensitivity is expected because both parameters are defined in a wavelength band where the bulk liquid and ice absorption coefficients peak (1500 nm – 1640 nm). In addition, the  $\tau$ - and  $r_e$ -uncertainties are evaluated by calculating the variance in the probability distribution that is only dependent on either  $\tau$  or  $r_e$ , respectively. The retrieved  $\tau$  and  $r_e$  for ice clouds have more variance than for liquid water clouds with a greater average  $\tau$ -uncertainty for ice clouds ( $\pm 1.3$ ) than for liquid water clouds ( $\pm 0.8$ ). The average  $r_e$ -uncertainty percentage is similar for ice and liquid water clouds (4.8%). The retrieval obtained the correct thermodynamic phase with a probability that is never lower than 99.4% for horizontally homogeneous clouds of unique thermodynamic phase. To further test the retrieval, we simulated clouds with vertically varying  $r_e$ . When using radiance transmitted through these clouds,

the retrieved  $\tau$  and  $r_e$  are biased from truth and their uncertainties are larger than for vertically constant  $r_e$  clouds.

## 5.1 Outlook

Even though the general effect of clouds and aerosols is to reduce the shortwave radiation at the surface, satellite based measurements are used to generate climate models of cloud and aerosol properties. With continued observations of clouds from below and direct measurements of aerosols, these climate models can be more constrained. Using the retrieval based on multiple spectral features in transmittance, cloud thermodynamic phase can be determined. In addition,  $\tau$  and  $r_e$  can be retrieved with smaller uncertainty than it would have been possible with traditional methods. Now ground-based observations of clouds are no longer limited by large uncertainties in  $r_e$ , and therefore can be used to further study cloud processes, such as aerosol-cloud interactions, although assumptions in modeling the scattering by cloud particles must still be made.

In future work, the retrieval based on multiple spectral features in cloud-transmitted radiance presented in this thesis will be used to quantify clouds sampled during two other field missions.  $\tau$ ,  $r_e$ , and  $\phi$  will be extracted from measurements of zenith cloud-transmitted radiance spectra taken by the Spectrometer for Sky-Scanning, Sun-Tracking Atmospheric Research [4STAR, *Dunagan et al.*, 2013]. More than 13 hours over nine days of these 4STAR measurements were taken during the recent Two-Column Aerosol Project (TCAP) held in February 2013. 4STAR also measured cloud-transmittance during the recent Studies of Emissions and Atmospheric Composition, Clouds and Climate Coupling by Regional Surveys (SEAC<sup>4</sup>RS) field mission, which took place during August-September 2013.

During these field missions, retrievals from transmittance are likely to extract different cloud properties than those from reflectance. Such differences in cloud properties retrieved from reflected and transmitted radiance could have important implications in determining biases in climate modeling due to only using cloud properties derived from reflected light. As such, cloud properties retrieved from transmittance will also be compared with coincident cloud properties extracted

from satellite based measurements and from in situ measurements. To reconcile the differences in sampling volumes, an optimal estimation method similarly to the technique described by *Feingold et al.* [2006] will be used.

Clouds, such as those encountered during these field missions, are likely influenced by aerosol. As well as quantifying the cloud properties from TCAP and SEAC<sup>4</sup>RS, the microphysical aerosol-cloud interactions will be investigated. Cloud properties together with in situ measurements of aerosol particle concentration, absorption, and scattering near cloud base will be used to evaluate aerosol-cloud interactions. Aerosol-cloud interactions can be calculated following the technique described by *McComiskey et al.* [2009] but applied to airborne measurements at cloud base.

Since 10 of the 15 parameters contributed to the information content by more than 0.02, the omitted parameters may be useful in extracting additional cloud optical and microphysical properties. Therefore, other future work includes using all 15 parameters to retrieve not only  $\tau$ ,  $r_e$ , and  $\phi$ , but also the proportion of ice cloud particles to liquid cloud particles in mixed-phase clouds.

## Bibliography

- Allan, R. P., Combining satellite data and models to estimate cloud radiative effect at the surface and in the atmosphere, *Meteorological applications*, 18, 324–333, doi:10.1002/met.285, 2011.
- Baum, B. a., P. F. Soulen, K. I. Strabala, M. D. King, S. a. Ackerman, W. P. Menzel, and P. Yang, Remote sensing of cloud properties using MODIS airborne simulator imagery during SUCCESS 2. Cloud thermodynamic phase, *Journal of Geophysical Research*, 105(D9), 11,781–11,792, 2000.
- Baum, B. a., P. Yang, and A. J. Heymsfield, The Next Generation of Ice Cloud Bulk Scattering/Absorption Models at Visible through Infrared Wavelengths, *Imaging and Applied Optics*, p. HTuB2, doi:10.1364/HISE.2011.HTuB2, 2011.
- Bellouin, N., O. Boucher, J. Haywood, and M. S. Reddy, Global estimate of aerosol direct radiative forcing from satellite measurements., *Nature*, 438(7071), 1138–1141, doi:10.1038/nature04348, 2005.
- Bergstrom, R., P. Pilewskie, B. Schmid, and P. B. Russell, Estimates of the spectral aerosol single scattering albedo and aerosol radiative effects during SAFARI 2000, *Journal of Geophysical Research*, 108(D13), 1–11, doi:10.1029/2002JD002435, 2003.
- Bergstrom, R. W., P. Pilewskie, P. B. Russell, J. Redemann, T. C. Bond, P. K. Quinn, and B. Sierau, Spectral absorption properties of atmospheric aerosols, *Atmospheric Chemistry and Physics*, 7(4), 10,669–10,686, 2007.
- Bevington, P. R., and D. K. Robinson, *Data reduction and error analysis for the physical sciences*, McGraw-Hill Higher Education, 2003.
- Bohren, C. F., and E. Clothiaux, *Fundamentals of atmospheric radiation*, Wiley. com, 2006.
- Bond, T. C., and H. Sun, Can reducing black carbon emissions counteract global warming?, *Environmental science & technology*, 39(16), 5921–6, 2005.
- Brock, C. a., Particle growth in urban and industrial plumes in Texas, *Journal of Geophysical Research*, 108(D3), 4111, doi:10.1029/2002JD002746, 2003.
- Brock, C. a., Particle characteristics following cloud-modified transport from Asia to North America, *Journal of Geophysical Research*, 109(D23), D23S26, doi:10.1029/2003JD004198, 2004.
- Bush, B. C., Surface aerosol radiative forcing at Gosan during the ACE-Asia campaign, *Journal of Geophysical Research*, 108(D23), 8660, doi:10.1029/2002JD003233, 2003.

- Bush, B. C., and F. P. J. Valero, Spectral aerosol radiative forcing at the surface during the Indian Ocean Experiment ( INDOEX ), *Journal of Geophysical Research*, *107*, 2002.
- Chang, F.-L., and Z. Li, Retrieving vertical profiles of water-cloud droplet effective radius: Algorithm modification and preliminary application, *Journal of Geophysical Research: Atmospheres*, *108*(D24), n/a–n/a, doi:10.1029/2003JD003906, 2003.
- Chiu, C., A. Marshak, Y. Knyazikhin, W. J. Wiscombe, H. W. Barker, J. C. Barnard, Y. Luo, and J. C. Chiu, Remote sensing of cloud properties using ground-based measurements of zenith radiance, *Journal of Geophysical Research*, *111*(D16), D16,201, doi:10.1029/2005JD006843, 2006.
- Chiu, C., A. Marshak, Y. Knyazikhin, P. Pilewskie, and W. J. Wiscombe, Physical interpretation of the spectral radiative signature in the transition zone between cloud-free and cloudy regions, *Atmospheric Chemistry and Physics*, *9*(2008), 1419–1430, 2009.
- Chiu, J. C., C.-H. Huang, A. Marshak, I. Slutsker, D. M. Giles, B. N. Holben, Y. Knyazikhin, and W. J. Wiscombe, Cloud optical depth retrievals from the Aerosol Robotic Network (AERONET) cloud mode observations, *Journal of Geophysical Research*, *115*(D14), 1–12, doi:10.1029/2009JD013121, 2010.
- Chung, C. E., V. Ramanathan, D. Kim, and I. a. Podgorny, Global anthropogenic aerosol direct forcing derived from satellite and ground-based observations, *Journal of Geophysical Research*, *110*(D24), 1–17, doi:10.1029/2005JD006356, 2005.
- Coddington, O., P. Pilewskie, and T. Vukicevic, The Shannon information content of hyperspectral shortwave cloud albedo measurements: Quantification and practical applications, *Journal of Geophysical Research*, *117*(D4), 1–12, doi:10.1029/2011JD016771, 2012.
- Coddington, O. M., P. Pilewskie, K. Schmidt, P. McBride, and T. Vukicevic, Characterizing a New Surface-Based Shortwave Cloud Retrieval Technique, Based on Transmitted Radiance for Soil and Vegetated Surface Types, *Atmosphere*, *4*(1), 48–71, doi:10.3390/atmos4010048, 2013.
- Cooper, S., T. L'Ecuyer, P. Gabriel, A. J. Baran, and G. L. Stephens, Objective assessment of the information content of visible and infrared radiance measurements for cloud microphysical property retrievals over the global oceans. Part, *Journal of Applied Meteorology and Climatology*, *45*, 42–62, 2006.
- Cumming, J. B., Temperature dependence of light absorption by water, *Nuclear Instruments and Methods in Physics Research Section A: Accelerators, Spectrometers, Detectors and Associated Equipment*, *713*, 1–4, doi:http://dx.doi.org/10.1016/j.nima.2013.02.024, 2013.
- Daniel, J. S., Cloud liquid water and ice measurements from spectrally resolved near-infrared observations: A new technique, *Journal of Geophysical Research*, *107*(D21), 4599, doi:10.1029/2001JD000688, 2002.
- Daniel, J. S., S. Solomon, H. L. Miller, a. O. Langford, R. W. Portmann, and C. S. Eubank, Retrieving cloud information from passive measurements of solar radiation absorbed by molecular oxygen and O<sub>2</sub>-O<sub>2</sub>, *Journal of Geophysical Research*, *108*(D16), 1–12, doi:10.1029/2002JD002994, 2003.

- Daniel, J. S., R. W. Portmann, H. L. Miller, S. Solomon, a. O. Langford, C. S. Eubank, R. Schofield, D. D. Turner, and M. D. Shupe, Cloud property estimates from zenith spectral measurements of scattered sunlight between 0.9 and 1.7  $\mu$  m, *Journal of Geophysical Research*, 111(D16), D16,208, doi:10.1029/2005JD006641, 2006.
- Dubovik, O., B. Holben, T. F. Eck, A. Smirnov, Y. J. Kaufman, M. D. King, D. Tanré, and I. Slutsker, Variability of Absorption and Optical Properties of Key Aerosol Types Observed in Worldwide Locations, *Journal of the Atmospheric Sciences*, 59(3), 590–608, 2002.
- Dunagan, S. E., et al., Spectrometer for Sky-Scanning Sun-Tracking Atmospheric Research (4STAR): Instrument Technology Development, *Remote Sensing*, 5, 3872–3895, 2013.
- Eck, T., B. Holben, and J. Reid, Wavelength dependence of the optical depth of biomass burning, urban, and desert dust aerosols, *Journal of Geophysical Research*, 104(1), 31,333–31,349, 1999.
- Ehrlich, A., E. Bierwirth, M. Wendisch, J.-f. Gayet, G. Mioche, A. Lampert, and J. Heintzenberg, Cloud phase identification of Arctic boundary-layer clouds from airborne spectral reflection measurements: test of three approaches, *Atmospheric Chemistry and Physics*, 8, 7493–7505, 2008.
- Esteve, a. R., J. a. Ogren, P. J. Sheridan, E. Andrews, B. N. Holben, and M. P. Utrillas, Sources of discrepancy between aerosol optical depth obtained from AERONET and in-situ aircraft profiles, *Atmospheric Chemistry and Physics*, 12(6), 2987–3003, doi:10.5194/acp-12-2987-2012, 2012.
- Evans, K. F., The Spherical Harmonics Discrete Ordinate Method for Three-Dimensional Atmospheric Radiative Transfer, *Journal of the Atmospheric Sciences*, 55(3), 429–446, doi: 10.1175/1520-0469(1998)055<0429:TSHDOM>2.0.CO;2, 1998.
- Feingold, G., R. Furrer, P. Pilewskie, L. a. Remer, Q. Min, and H. Jonsson, Aerosol indirect effect studies at Southern Great Plains during the May 2003 Intensive Operations Period, *Journal of Geophysical Research*, 111(D5), D05S14, doi:10.1029/2004JD005648, 2006.
- Forster, P., et al., Changes in atmospheric constituents and in radiative forcing, in *Climate Change 2007: The Physical Science Basis. Contribution of Working Group I to the Fourth Assessment Report of the Intergovernmental Panel on Climate Change [Solomon, S., D. Qin, M. Manning, Z. Chen, M. Marquis, K.B. Averyt, M. Tignor and H.L. Miller*, Cambridge University Press, Cambridge, United Kingdom and New York, NY, USA, 2007.
- Hair, J. W., C. a. Hostetler, A. L. Cook, D. B. Harper, R. a. Ferrare, T. L. Mack, W. Welch, L. R. Isquierdo, and F. E. Hovis, Airborne high spectral resolution lidar for profiling aerosol optical properties., *Applied Optics*, 47(36), 6734–6752, 2008.
- Han, Q., W. Rossow, and A. Lacis, Near-global survey of effective droplet radii in liquid water clouds using ISCCP data, *Journal of Climate*, 7, 1994.
- Hansen, J., and J. Hovenier, Interpretation of the polarization of Venus, *J. Atmos. Sci.*, 31, 1137–1160, 1974.
- Holben, B. N., et al., AERONET A Federated Instrument Network and Data Archive for Aerosol Characterization, *Remote Sensing of Environment*, 4257(98), 1998.
- Horler, D. N. H., M. DOCKRAY, and J. Barber, The red edge of plant leaf reflectance, *International Journal of Remote Sensing*, 4(2), 273–288, 1983.

- Hu, Y., B. Wielicki, B. Lin, G. Gibson, S.-C. Tsay, K. Stamnes, and T. Wong,  $\delta$ -Fit: A fast and accurate treatment of particle scattering phase functions with weighted singular-value decomposition least-squares fitting, *Journal of Quantitative Spectroscopy and Radiative Transfer*, *65*, 681–690, 2000.
- Iwabuchi, H., and T. Hayasaka, Effects of Cloud Horizontal Inhomogeneity on the Optical Thickness Retrieved from Moderate-Resolution Satellite Data, *Journal of Atmospheric Sciences*, *59*(2000), 2227–2242, 2002.
- Jacob, D. J., J. H. Crawford, H. Maring, A. D. Clarke, and J. E. Dibb, The ARCTAS aircraft mission : design and execution, *Atmospheric Chemistry and Physics*, *9*(July 2008), 17,073–17,123, 2009.
- Kaufman, Y. J., D. Tanré, and O. Boucher, A satellite view of aerosols in the climate system, *Nature*, *419*(September), 215–223, 2002.
- Key, J. R., and J. M. Intrieri, Cloud Particle Phase Determination with the AVHRR, *Journal of Applied Meteorology*, *39*(10), 1797–1804, doi:10.1175/1520-0450-39.10.1797, 2000.
- Kikuchi, N., T. Nakajima, H. Kumagai, H. Kuroiwa, A. Kamei, R. Nakamura, and T. Y. Nakajima, Cloud optical thickness and effective particle radius derived from transmitted solar radiation measurements: Comparison with cloud radar observations, *Journal of Geophysical Research*, *111*(D7), D07,205, doi:10.1029/2005JD006363, 2006.
- Kim, D., and V. Ramanathan, Solar radiation budget and radiative forcing due to aerosols and clouds, *Journal of Geophysical Research*, *113*(D2), D02,203, doi:10.1029/2007JD008434, 2008.
- Kindel, B. C., K. S. Schmidt, P. Pilewskie, B. a. Baum, P. Yang, and S. Platnick, Observations and modeling of ice cloud shortwave spectral albedo during the Tropical Composition, Cloud and Climate Coupling Experiment (TC 4 ), *Journal of Geophysical Research*, *115*, D00J18, doi:10.1029/2009JD013127, 2010.
- Kurucz, R. L., Synthetic Infrared-spectra, in *INFRARED SOLAR PHYSICS*, edited by C. Rabin, DM and Jefferies, JT and Lindsey, no. 154 in IAU SYMPOSIA, pp. 523–531, INT ASTRON UNION, KLUWER ACADEMIC PUBL, PO BOX 17, 3300 AA DORDRECHT, NETHERLANDS, 1994.
- Lack, D. a., M. S. Richardson, D. Law, J. M. Langridge, C. D. Cappa, R. J. McLaughlin, and D. M. Murphy, Aircraft Instrument for Comprehensive Characterization of Aerosol Optical Properties, Part 2: Black and Brown Carbon Absorption and Absorption Enhancement Measured with Photo Acoustic Spectroscopy, *Aerosol Science and Technology*, *46*(5), 555–568, doi:10.1080/02786826.2011.645955, 2012.
- Langridge, J. M., M. S. Richardson, D. Lack, D. Law, and D. M. Murphy, Aircraft Instrument for Comprehensive Characterization of Aerosol Optical Properties, Part I: Wavelength-Dependent Optical Extinction and Its Relative Humidity Dependence Measured Using Cavity Ringdown Spectroscopy, *Aerosol Science and Technology*, *45*(11), 1305–1318, doi:10.1080/02786826.2011.592745, 2011.
- LeBlanc, S. E., K. S. Schmidt, P. Pilewskie, J. Redemann, C. Hostetler, R. Ferrare, J. Hair, J. M. Langridge, and D. a. Lack, Spectral aerosol direct radiative forcing from airborne radiative measurements during CalNex and ARCTAS, *Journal of Geophysical Research*, *117*, D00V20, doi:10.1029/2012JD018106, 2012.

- LeBlanc, S. E., P. Pilewskie, K. S. Schmidt, and O. Coddington, A generalized method for discriminating thermodynamic phase and retrieving cloud optical thickness and effective radius using transmitted shortwave radiance spectra, *Atmospheric Measurement Techniques Discussions*, (In Preperation), 2014.
- L'Ecuyer, T., P. Gabriel, K. Leesman, S. Cooper, and G. L. Stephens, Objective assessment of the information content of visible and infrared radiance measurements for cloud microphysical property retrievals over the global oceans. Part, *Journal of Applied Meteorology and Climatology*, *45*, 20–41, 2006.
- Magi, B. I., Q. Fu, J. Redemann, and B. Schmid, Using aircraft measurements to estimate the magnitude and uncertainty of the shortwave direct radiative forcing of southern African biomass burning aerosol, *Journal of Geophysical Research*, *113*(D5), D05,213, doi:10.1029/2007JD009258, 2008.
- Marshak, A., Y. Knyazikhin, K. D. Evans, and W. J. Wiscombe, The RED versus NIR plane to retrieve broken-cloud optical depth from ground-based measurements, *Journal of the Atmospheric Sciences*, *61*, 1911–1925, 2004.
- Marshak, A., S. Platnick, T. Várnai, G. Wen, and R. F. Cahalan, Impact of three-dimensional radiative effects on satellite retrievals of cloud droplet sizes, *Journal of Geophysical Research*, *111*(D9), D09,207, doi:10.1029/2005JD006686, 2006.
- Marshak, a., Y. Knyazikhin, J. C. Chiu, and W. J. Wiscombe, Spectral invariant behavior of zenith radiance around cloud edges observed by ARM SWS, *Geophysical Research Letters*, *36*(16), 5 PP., doi:10.1029/2009GL039366, 2009.
- Massoli, P., et al., Aerosol optical and hygroscopic properties during TexAQSGoMACCS 2006 and their impact on aerosol direct radiative forcing, *Journal of Geophysical Research*, *114*(null), D00f07, doi:10.1029/2008JD011604, 2009.
- Mayer, B., and a. Kylling, Technical note: The libRadtran software package for radiative transfer calculations description and examples of use, *Atmospheric Chemistry and Physics Discussions*, *5*(2), 1855–1877, 2005.
- McBride, P. J., K. S. Schmidt, P. Pilewskie, a. S. Kittelman, and D. E. Wolfe, A spectral method for retrieving cloud optical thickness and effective radius from surface-based transmittance measurements, *Atmospheric Chemistry and Physics*, *11*(14), 7235–7252, doi:10.5194/acp-11-7235-2011, 2011.
- McBride, P. J., K. S. Schmidt, P. Pilewskie, A. Walther, a. K. Heidinger, D. E. Wolfe, C. W. Fairall, and S. Lance, CalNex cloud properties retrieved from a ship-based spectrometer and comparisons with satellite and aircraft retrieved cloud properties, *Journal of Geophysical Research: Atmospheres*, *117*(D21), 1–10, doi:10.1029/2012JD017624, 2012.
- McComiskey, A., G. Feingold, a. S. Frisch, D. D. Turner, M. a. Miller, C. Chiu, Q. Min, J. a. Ogren, and J. C. Chiu, An assessment of aerosolcloud interactions in marine stratus clouds based on surface remote sensing, *Journal of Geophysical Research*, *114*(D9), D09,203, doi:10.1029/2008JD011006, 2009.

- Meyer, K., and S. Platnick, Utilizing the MODIS 1.38  $\mu$  m channel for cirrus cloud optical thickness retrievals: Algorithm and retrieval uncertainties, *Journal of Geophysical Research*, 115(D24), D24,209, doi:10.1029/2010JD014872, 2010.
- Meywerk, J., and V. Ramanathan, Observations of the spectral clear-sky aerosol forcing over the tropical Indian Ocean, *Journal of Geophysical Research*, 104(D20), 24,359–24,370, 1999.
- Michalsky, J., Q. Min, J. Barnard, R. Marchand, and P. Pilewskie, Simultaneous spectral albedo measurements near the Atmospheric Radiation Measurement Southern Great Plains (ARM SGP) central facility, *Journal of Geophysical Research*, 108(D8), 4254, doi:10.1029/2002JD002906, 2003.
- Miles, N. L., J. Verlinde, and E. E. Clothiaux, Cloud Droplet Size Distributions in Low-Level Stratiform Clouds, *Journal of Atmospheric Sciences*, 57, 295–311, 2000.
- Minnis, P., D. P. Kratz, J. A. Coakley Jr, M. D. King, D. Garber, P. Heck, S. Mayor, D. F. Young, and R. Arduini, Cloud optical property retrieval (subsystem 4.3), *Clouds and the Earth's Radiant Energy System (CERES) Algorithm Theoretical Basis Document*, 3, 135–176, 1995.
- Mosegaard, K., and A. Tarantola, 16 Probabilistic approach to inverse problems, *International Geophysics*, pp. 237–265, 2002.
- Nakajima, T., and M. D. King, Determination of the Optical Thickness and Effective Particle radius of clouds from reflected solar radiation measurements. Part I: Theory, *Journal of the Atmospheric Sciences*, 47(15), 1878–1893, 1990.
- Nakajima, T., and M. Tanaka, Algorithms for radiative intensity calculations in moderately thick atmospheres using a truncation approximation, *Journal of Quantitative Spectroscopy and Radiative Transfer*, 40(1), 51–69, 1988.
- Penner, J., et al., Quantifying and minimizing uncertainty of climate forcing by anthropogenic aerosols, *Bulletin of the American Meteorological Society*, 75, 375–400, 1994.
- Petters, M. D., and S. M. Kreidenweis, A single parameter representation of hygroscopic growth and cloud condensation nucleus activity, *Atmospheric Chemistry and Physics*, 7(8), 1961–1971, 2007.
- Pilewskie, P., and S. Twomey, Discrimination of Ice from Water in Clouds by Optical Remote Sensing, *Atmospheric Research*, 21, 113–122, 1987.
- Pilewskie, P., J. Pommier, R. Bergstrom, W. Gore, S. Howard, M. Rabbette, B. Schmid, P. V. Hobbs, and S. C. Tsay, Solar Spectral Radiative Forcing During the Southern African Regional Science Initiative, *Journal of Geophysical Research*, 108(D13), 1–7, doi:10.1029/2002JD002411, 2003.
- Platnick, S., Vertical photon transport in cloud remote sensing problems, *Journal of Geophysical Research*, 105(D18), 22,919–22,935, 2000.
- Platnick, S., J. Y. Li, M. D. King, H. Gerber, and P. V. Hobbs, A solar reflectance method for retrieving the optical thickness and droplet size of liquid water clouds over snow and ice surfaces, *Journal of Geophysical Research*, 106(D14), 15,185–15,199, 2001.

- Platnick, S., M. D. King, S. a. Ackerman, W. P. Menzel, B. a. Baum, J. C. Riedi, and R. a. Frey, The MODIS cloud products: algorithms and examples from Terra, *IEEE Transactions on Geoscience and Remote Sensing*, *41*(2), 459–473, 2003.
- Ptashnik, I. V., K. M. Smith, K. P. Shine, and D. a. Newnham, Laboratory measurements of water vapour continuum absorption in spectral region 5000-5600 cm(-1): Evidence for water dimers, *Quarterly Journal of the Royal Meteorological Society*, *130*(602), 2391–2408, doi:10.1256/qj.03.178, 2004.
- Rawlins, F., and J. Foot, Remotely sensed measurements of stratocumulus properties during FIRE using the C130 aircraft multi-channel radiometer., *Journal of Atmospheric Sciences*, 1990.
- Redemann, J., et al., Suborbital Measurements of Spectral Aerosol Optical Depth and Its Variability at Subsatellite Grid Scales in Support of CLAMS 2001, *Journal of the Atmospheric Sciences*, *62*(4), 993–1007, 2005.
- Redemann, J., et al., Airborne measurements of spectral direct aerosol radiative forcing in the Intercontinental chemical Transport Experiment/Intercontinental Transport and Chemical Transformation of anthropogenic pollution, 2004, *Journal of Geophysical Research*, *111*(D14), D14,210, doi:10.1029/2005JD006812, 2006.
- Remer, L., and Y. Kaufman, Aerosol direct radiative effect at the top of the atmosphere over cloud free ocean derived from four years of MODIS data, *Atmospheric Chemistry and Physics*, pp. 237–253, 2006.
- Ricchiazzi, P., S. Yang, C. Gautier, and D. Sowle, SBDART: A Research and Teaching Software Tool for Plane-Parallel Radiative Transfer in the Earth's Atmosphere, *Bulletin of the American Meteorological Society*, *79*(10), 2101–2114, 1998.
- Rothman, L. S., et al., The HITRAN 2008 molecular spectroscopic database, *Journal of Quantitative Spectroscopy and Radiative Transfer*, *110*(9-10), 533–572, doi:10.1016/j.jqsrt.2009.02.013, 2009.
- Russell, P. B., S. A. Kinne, and R. W. Bergstrom, Aerosol climate effects: Local radiative forcing and column closure experiments, *Journal of Geophysical Research*, *102*, 9397–9407, 1997.
- Russell, P. B., et al., Absorption Angstrom Exponent in AERONET and related data as an indicator of aerosol composition, *Atmospheric Chemistry and Physics*, *10*(3), 1155–1169, 2010.
- Schaaf, C. B., et al., First operational BRDF, albedo nadir reflectance products from MODIS, *Remote Sensing of Environment*, *83*(1-2), 135–148, doi:10.1016/S0034-4257(02)00091-3, 2002.
- Schmidt, K. S., et al., A new method for deriving aerosol solar radiative forcing and its first application within MILAGRO/INTEX-B, *Atmospheric Chemistry and Physics*, *10*(16), 7829–7843, doi:10.5194/acp-10-7829-2010, 2010.
- Schofield, R., et al., Retrieval of effective radius and liquid water path from ground-based instruments: A case study at Barrow, Alaska, *Journal of Geophysical Research*, *112*(D21), D21,203, doi:10.1029/2007JD008737, 2007.
- Shannon, C. E., and W. Weaver, The mathematical theory of commcopernicus.bstunication, *University of Illinois Press*, *19*(7), 1, 1949.

- Shinozuka, Y., et al., Airborne observation of aerosol optical depth during ARCTAS: vertical profiles, inter-comparison and fine-mode fraction, *Atmospheric Chemistry and Physics*, 11(8), 3673–3688, doi:10.5194/acp-11-3673-2011, 2011.
- Slingo, A., Sensitivity of the Earth’s radiation budget to changes in low clouds, *Nature*, 1990.
- Stamnes, K., S. Tsay, W. J. Wiscombe, and I. Laszlo, DISORT, a general-purpose Fortran program for discrete-ordinate-method radiative transfer in scattering and emitting layered media: documentation of methodology, *Tech. rep.*, Dept. of Physics and Engineering Physics, Stevens Institute of Technology, Hoboken, NJ 07030, 2000.
- Sun, Z., and K. P. Shine, Studies of the radiative properties of ice and mixed-phase clouds, *Quarterly Journal of the Royal Meteorological Society*, 120(515), 111–137, 1994.
- Sun, Z., and K. P. Shine, Parameterization of ice cloud radiative properties and its application to the potential climatic importance of mixed-phase clouds, *Journal of climate*, 8(7), 1874–1888, 1995.
- Tarantola, A., *Inverse Problem Theory and Methods for Model Parameter Estimation*, 342 pp., Society for Industrial and Applied Mathematics, 2005.
- Taylor, J. R., *An introduction to error analysis: the study of uncertainties in physical measurements*, University science books, 1997.
- Turner, D. D., et al., Thin Liquid Water Clouds: Their Importance and Our Challenge, *Bulletin of the American Meteorological Society*, 88(2), 177–190, doi:10.1175/BAMS-88-2-177, 2007.
- Twomey, S., and C. F. Bohren, Simple Approximations for Calculations of Absorption in Clouds, *Journal of the Atmospheric Sciences*, 37(9), 2086–2095, doi:10.1175/1520-0469(1980)037<2086:SAFCOA>2.0.CO;2, 1980.
- Twomey, S., and T. Cocks, Remote sensing of cloud parameters from spectral reflectance in the near-infrared, *Beiträge zur Physik der Atmosphäre*, 62(3), 172–179, 1989.
- Vukicevic, T., and D. Posselt, Analysis of the Impact of Model Nonlinearities in Inverse Problem Solving, *Journal of the Atmospheric Sciences*, 65(9), 2803–2823, doi:10.1175/2008JAS2534.1, 2008.
- Vukicevic, T., O. Coddington, and P. Pilewskie, Characterizing the retrieval of cloud properties from optical remote sensing, *Journal of Geophysical Research*, 115(D20), 1–14, doi:10.1029/2009JD012830, 2010.
- Wan, Z., and Z.-l. Li, A Physics-Based Algorithm for Retrieving Land-Surface Emissivity and Temperature from EOS / MODIS Data, *IEEE Transactions on Geoscience and Remote Sensing*, 35(4), 980–996, 1997.
- Warren, S. G., and R. E. Brandt, Optical constants of ice from the ultraviolet to the microwave: A revised compilation, *Journal of Geophysical Research*, 113(D14), 1–10, doi:10.1029/2007JD009744, 2008.
- Westphal, D. L., and O. B. Toon, Simulations of microphysical, radiative, and dynamical processes in a continental-scale forest fire smoke plume, *Journal of Geophysical Research*, 96(D12), 22,379–22,400, 1991.

- Wiscombe, W., *Mie scattering calculations: advances in technique and fast, vector-speed computer codes*, June, Atmospheric Analysis and Prediction Division, National Center for Atmospheric Research, 1979.
- Wiscombe, W., Improved Mie scattering algorithms, *Applied optics*, 1980.
- Wiscombe, W., and G. Grams, The backscattered fraction in two-stream approximations, *genesis*, *33*, 2440–2451, 1976.
- Wiscombe, W., and S. Warren, A model for the spectral albedo of snow. I: Pure snow, *Journal of the Atmospheric Sciences*, *37*, 2712–2733, 1980.
- Wiscombe, W. J., R. M. Welch, and W. D. Hall, The Effects of Very Large Drops on Cloud Absorption. Part I: Parcel Models, *Journal of the Atmospheric Sciences*, *41*(8), 1336–1355, doi:10.1175/1520-0469(1984)041<1336:TEOVLD>2.0.CO;2, 1984.
- Yu, H., M. Chin, L. a. Remer, R. G. Kleidman, N. Bellouin, H. Bian, and T. Diehl, Variability of marine aerosol fine-mode fraction and estimates of anthropogenic aerosol component over cloud-free oceans from the Moderate Resolution Imaging Spectroradiometer (MODIS), *Journal of Geophysical Research*, *114*(D10), D10,206, doi:10.1029/2008JD010648, 2009.
- Yu, H., et al., A review of measurement-based assessments of the aerosol direct radiative effect and forcing, *Atmospheric Chemistry and Physics*, *6*(3), 613–666, 2006.
- Zhang, S., H. Xue, and G. Feingold, Vertical profiles of droplet effective radius in shallow convective clouds, *Atmospheric Chemistry and Physics*, *11*(10), 4633–4644, doi:10.5194/acp-11-4633-2011, 2011.